Master thesis : Rotation Curve of the Spiral Galaxy NGC 7331 from the Luminosity and Mass Profiles

Auteur : Lopez Lopez, Andrea
Promoteur(s) : Magain, Pierre
Faculté : Faculté des Sciences appliquées
Diplôme : Master en ingénieur civil en aérospatiale, à finalité spécialisée en "aerospace engineering"
Année académique : 2018-2019
URI/URL : http://hdl.handle.net/2268.2/6292

Université de Liège

Faculty of Applied Sciences

Rotation Curve of the Spiral Galaxy NGC 7331 from the Luminosity and Mass Profiles

Author:
Andrea López

Supervisor:
Prof. Pierre Magain

Graduation Studies conducted for obtaining the Master's degree in Aerospace Engineering by Andrea López

Academic year 2018-2019

Abstract

The present work consists in the obtention of the rotation curve of the spiral galaxy NGC 7331 from its luminosity profile. In order to do that, 14 images of different spectral bands (from the far ultraviolet to the far infrared) were used, dividing the galaxy in concentric elliptical annuli to obtain the flux for the different distances to the galactic center, and for each spectral band. The luminosity profiles were then corrected for dust absorption. These spectra were then adjusted to stellar population models, using a two-burst function to represent the stellar formation events. With these stellar populations, the stellar mass profile is calculated. The mass profile for the gas in the galaxy is calculated as well, and added to the stellar mass to obtain the total mass profile. This result is used to calculate the rotation curve, with the hypothesis of spherical mass distribution for the bulge and circular planar mass distribution for the galactic disk. This curve was then compared with the rotation curve obtained from spectroscopy, and some theories (i.e. underestimation of the distance, dark matter halo) were formulated in order to explain the differences between the two curves. Some other hypothesis, like the MOND theory, strong magnetic fields in the outer disk or undetected mass clouds, were also introduced, although not developed.

Acknowledgements

I would like to express the deepest appreciation to my advisor Professor Pierre Magain, who introduced me to Astrophysics, and whose passion for the topic had lasting effect. Without his supervision and constant help this dissertation would not have been possible. I would also like to thank Lyne Van de Vyvere, whose office door was always open whenever I ran into a trouble spot or had a question about my research. I would not forget to remember Judith Biernaux, Clémentine Hauret, Sandrine Sohy, Martin Farnir and Marin Ferrais for their constant encouragement, support and guidance till the completion of this dissertation.

This research has made use of the NASA/IPAC Extragalactic Database (NED), which is operated by the Jet Propulsion Laboratory, California Institute of Technology, under contract with the National Aeronautics and Space Administration.

This research has made use of the NASA/ IPAC Infrared Science Archive, which is operated by the Jet Propulsion Laboratory, California Institute of Technology, under contract with the National Aeronautics and Space Administration.

This research has made use of the SVO Filter Profile Service (http://svo2.cab.inta-csic.es/theory/fps/) supported from the Spanish MINECO through grant AyA2014-55216

Contents

List of Tables

List of Figures

Chapter 1

Introduction

1.1 Motivation and Objectives

Galaxies are the largest assemblages of stars in the universe. Although many observations have been made, and a great deal of information is known about them, galactic formation, evolution and structure is not as well known as, for example, those of the stars. Furthermore, galaxies are not longer seen as isolated and unchanging objects: they evolve, interact, merge and collide, modifying their initial characteristics. Galaxies are classified depending on their morphology: elliptic, lenticular, spiral or irregular [1]. An example of these different types can be found in Figure 1.1.

It is particularly interesting to study the structure of spiral galaxies, which is usually well differentiated in a central bulge, with a high concentration of stars, and a flat disk made up with younger stars, dust and gas [1]. In the disk there are structures of stars that extend from the center to the outer part, also called arms, wrapping the galaxy with a spiral-shape structure. These spiral arms suggest a rotation of the galactic disk, which can be observed with spectroscopy. Nowadays, the rotation

(a) M 49. *Credit:* NASA, ESA, STScI, J. Blakeslee

(b) NGC 2787. *Credit:* Hubble Heritage, NASA, M. Carollo

(c) M 63. *Credit:* ESA/Hubble, NASA

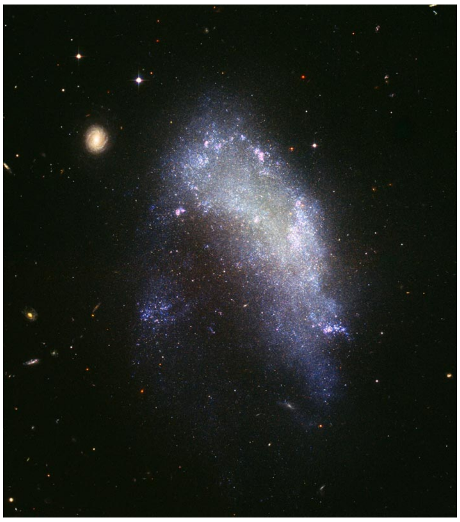

(d) NGC 1427A. *Credit:* Hubble Heritage, ESA, NASA

Figure 1.1: Examples of elliptic, lenticular, spiral and irregular galaxies, respectively.

curves of spiral galaxies are obtained thanks to the 21-cm line of atomic hydrogen [2]. When looking at a spiral galaxy with a certain inclination (with the galactic plane not perpendicular to the line-of-sight), there is a shift in the wavelengths of the observed line between one side of the galaxy, where the gas clouds move away from the Earth in their circular motion, and the other side of the galaxy, where the opposite effect takes place. This shift due to Doppler effect allows to calculate the velocity of rotation of the galaxy, once the inclination is known and assuming axisymmetry at all distances from the galactic center.

There is another method for obtaining the rotation curves of a spiral galaxy: using Newtonian physics to estimate the velocities in the orbits around the center of the galaxy, employing a mass profile of the galaxy, calculated from the luminosity of the galaxy in different wavelengths. When comparing the rotation curves obtained with both methods, there is a systematic difference between the two of them. The velocities obtained with spectroscopy are higher, and do not decrease in the outer regions of the galaxy (see Figure 1.2). There have been many attempts to explain this disagreement. Currently, the most widely accepted explanation is the presence of matter that does not interact with electromagnetic radiation, but that plays a role in the gravitational interactions, adding the remaining mass in the Newtonian model to increase the velocities obtained with this method [3, 4]. This theory of non-observable matter halos in the galaxies, called *dark matter* halos, was proposed by Pointcaré [5] and Zwicky [6], and developed by Jan Oort in the 1930's [4]. In the same line of thought, Jeremiah Ostriker and James Pleebles defended in 1973 that rotation disks are subject to an instability, unless a stabilizing dark matter halo is present in the spiral galaxy [4] (however, Kalnajs (1983) and Sellwood (1985) argued that a central bulge would be equally efficient to stabilize the arms [7]). Although the dark matter halos are a generally accepted explanation for the difference between the rotation curves obtained with the two methods, other explications are also contemplated, like the MOND (*MOdified Newtonian Dynamics*) theory [8, 9], a strong magnetic field in the outer disk [10] or the presence of undetected molecular clouds [11].

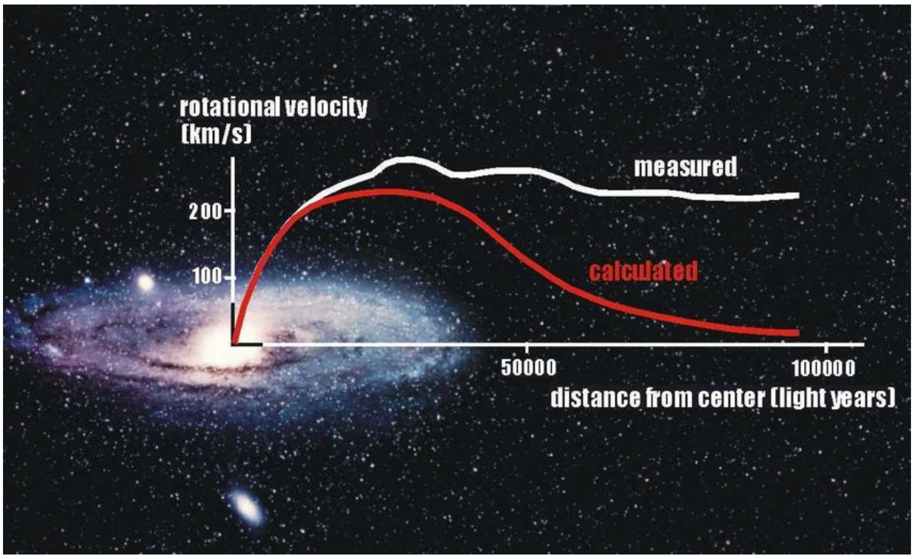

Figure 1.2: Rotation curves of galaxy M31 (Andromeda), both observed and calculated from the luminous disk. *Credit:* Queens University

Usually, the estimations of the rotation curve from the luminosity are carried out under the hypothesis of a *constant mass-luminosity ratio*. But this hypothesis is not evident, since it is possible that different types of stars (age, mass, metallicity) are found at different locations in the galaxy, which implies a variable mass-luminosity relation for the different distances to the galactic center. In addition to this, the observed luminosity in some wavelengths [2] is diminished due to the effect of the dust absorption (*reddening*), distorting the mass estimation. Another usual assumption for the calculation of the mass profile is the hypothesis of spherical symmetry, which is a very convenient assumption for the calculation of the velocity of rotation, because only the mass inside the sphere of radius r influences the speed in the orbit of the same radius [12, 4]. However, this is not a realistic assumption for the distances outside the galactic bulge, where the mass is rather distributed along a plane. Additionally to these assumptions, generally the mass of gas is either neglected or considered as a constant fraction of the stellar mass, which is in clear contradiction with the observations of galactic gas beyond the luminous disk.

The objective of this master thesis is, therefore, to provide a more realistic estimation of the mass profile of a spiral galaxy (specifically, of NGC 7331), which will allow to calculate a rotation curve with more accuracy, in order to compare it with the rotation curve obtained from spectroscopy.

1.2 The galaxy NGC 7331

NGC 7331 (also known as UGC 12113, PGC 69327 or Caldwell 30) is an unbarred spiral galaxy (type SA(s)b) [13] situated in the constellation Pegasus. This galaxy was first spotted by William Herschel in 1784 [14]. It is the brightest member of the NGC 7331 Group. In visible and infrared images, the core of the galaxy seems to be slightly off-centered, so one side of the disk appears to extend further away from the core than the opposite side [15]. It is located at a distance of 14.7 Mpc [16], at $RA = 339.26672000\,\text{deg}$ and $DEC = 34.41552000\,\text{deg}$ [13].

NGC 7331 is often referred to as "the Milky Way's twin", since its similar in size, shape and mass to our galaxy. The star formation rate, the number of stars and the spiral arms are also comparable to the ones in the Milky Way, and there is a black hole in its center as well. The main difference with our galaxy is that NGC 7331 is an unbarred spiral galaxy, unlike the Milky Way [17].

The central bulges in spiral galaxies normally rotate in the same direction as the disk. The case of the galaxy NGC 7331 is different: it was found that it has a counter-rotating bulge [18].

Figure 1.3: Color image of NGC 7331. *Credit:* D. Hager, T. Grossmann

1.3 Structure of the work

This dissertation is organized following the next scheme: first, the luminosity profile is obtained from a set of images in different wavelengths; then, the mass profile of the galaxy is estimated making use of theoretical stellar population models; finally, the rotation curve is deduced from this mass profile, and compared with the rotation curve obtained from the observations.

The galaxy NGC 7331 has been chosen for several reasons. The distance to the galaxy has been measured with the method of cepheids, which is the most accurate method in the present [16] for measuring astronomical distances. Furthermore, the distance to NGC 7331 is $14.70 \pm 1.50\, Mpc$ [16], which allows for a good resolution of the images while still fitting in one image of the telescope. The galactic plane is inclined with respect to the plane of the sky, which allows to measure the rotation curve with the Doppler effect. In addition, NGC 7331 is a spiral galaxy that has been widely observed and studied, having a large amount of data available (i.e. the distribution of neutral atomic hydrogen, or the rotation curve).

For the development of this dissertation, 14 spectral bands have been selected, from the far ultraviolet to the far infrared. The objective of using this wide range of spectral bands is to cover in great measure the spectrum of stars and dust present in the galaxy.

In order to obtain the luminosity profile, the coordinates of the center of the galaxy in the different images, the orientation of the galaxy and its apparent ellipticity were calculated. Once this information is known, a set of masks with the shape of concentric elliptical rings is applied to NGC 7331, allowing the obtention of the luminosity of the galaxy in each ring, and thus, at different distances from the galactic center.

Then, the emission in the far infrared is used to estimate the absorption of light in the ultraviolet, visible, and near infrared by the dust in the galaxy and correct these fluxes. Next, the absorption by the dust in the Milky Way in the line-of-sight is also taken into account.

For the obtention of the mass profile, the derived spectra were adjusted to the spectra for stellar population models. The star formation rate was modeled with burst functions. The mass of neutral atomic hydrogen and molecular hydrogen were obtained from the profiles of surface density, which are available in the literature. The mass of helium is also accounted for, assuming cosmological abundances.

The expected rotation curve from the luminous matter is obtained using the calculated mass profile, separating the bulge contribution, with a spherical mass distribution, from the contribution of the galactic disk, with a mass distribution contained in a plane. This results are then compared with the rotation curve obtained from the observations of the 21-cm line of hydrogen. Various causes are then discussed to explain the difference between the two curves.

Figure 1.4: Color image of NGC 7331: close-up. *Credit:* ESA Hubble, NASA, D. Milisavljevic

Chapter 2

Luminosity profile

In this chapter, the luminosity profile of the galaxy is calculated. First, the flux is obtained for the different radial distances to the center of the galaxy, in 14 wavelengths from the far ultraviolet to the far infrared. Then, these luminosity profiles are corrected for the absorption of light by the dust in the galaxy NGC 7331, and by the dust in the Milky Way in the line of observations. Finally, the luminosity profiles are presented for these 14 wavelengths. Unless stated otherwise, the same methodology as Van de Vyvere [19] is followed in this Chapter.

2.1 Images

The images used in this master thesis have been selected from the NED (NASA/IPAC Extragalactic Database[1])[13]. This database contains multiwavelength data and images for extragalactic objects, from gamma rays through radio frequencies. For the galaxy NGC 7331, the following bands have been selected: FUV and NUV (from the GALEX -Galaxy Evolution Explorer- telescope); u, g, r, i and z (from the

[1]The NASA/IPAC Extragalactic Database (NED) is operated by the Jet Propulsion Laboratory, California Institute of Technology, under contract with the National Aeronautics and Space Administration.

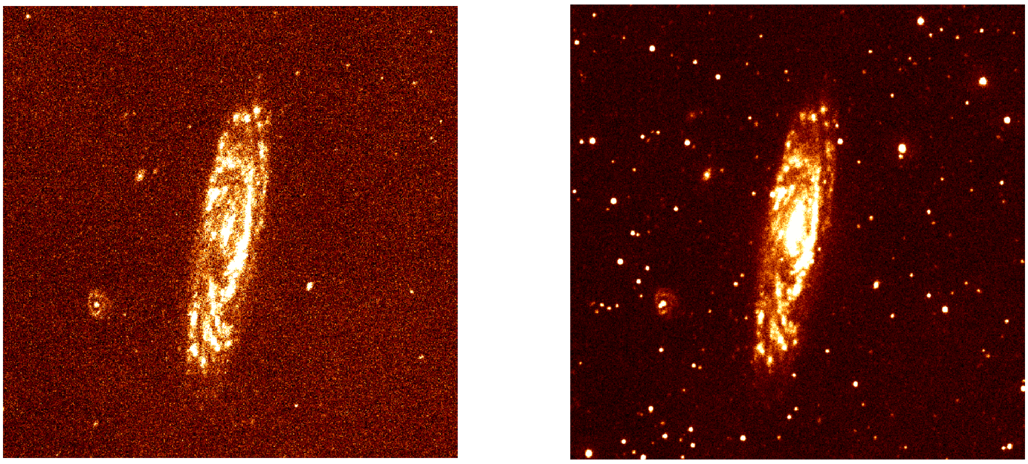

(a) GALEX FUV (b) GALEX NUV

Figure 2.1: Images from the GALEX telescope

telescopes of the project SDSS -Sloan Digital Sky Survey), four NIR and MIR wavelengths (from the Spitzer telescope) and three FIR wavelengths (from the Herschel telescope). The images are shown in Figures 2.1, 2.2, 2.3 and 2.4, and the corresponding spectral bands and effective wavelengths are listed in Table 2.1 [13].

Telescope	Spectral band	Effective wavelength
GALEX	FUV	$152.8nm$
GALEX	NUV	$227.1nm$
SDSS	u	$354.3nm$
SDSS	g	$477.0nm$
SDSS	r	$623.1nm$
SDSS	i	$762.5nm$
SDSS	z	$913.4nm$
Spitzer	IRAC3.6	$3.550\mu m$
Spitzer	IRAC4.5	$4.493\mu m$
Spitzer	IRAC8.0	$7.872\mu m$
Spitzer	MIPS24	$24\mu m$
Herschel	PACS70	$70\mu m$
Herschel	PACS100	$100\mu m$
Herschel	PACS160	$160\mu m$

Table 2.1: Spectral bands and effective wavelengths for the different images

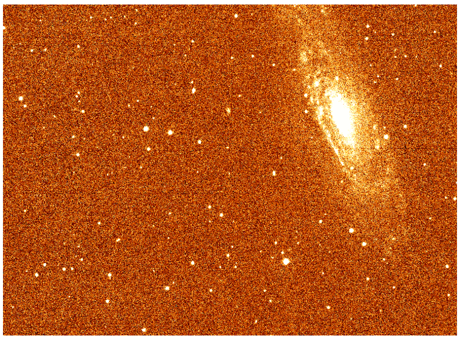

(a) SDSS u

(b) SDSS g

(c) SDSS r

(d) SDSS i

(e) SDSS z

Figure 2.2: Images from the SDSS telescope

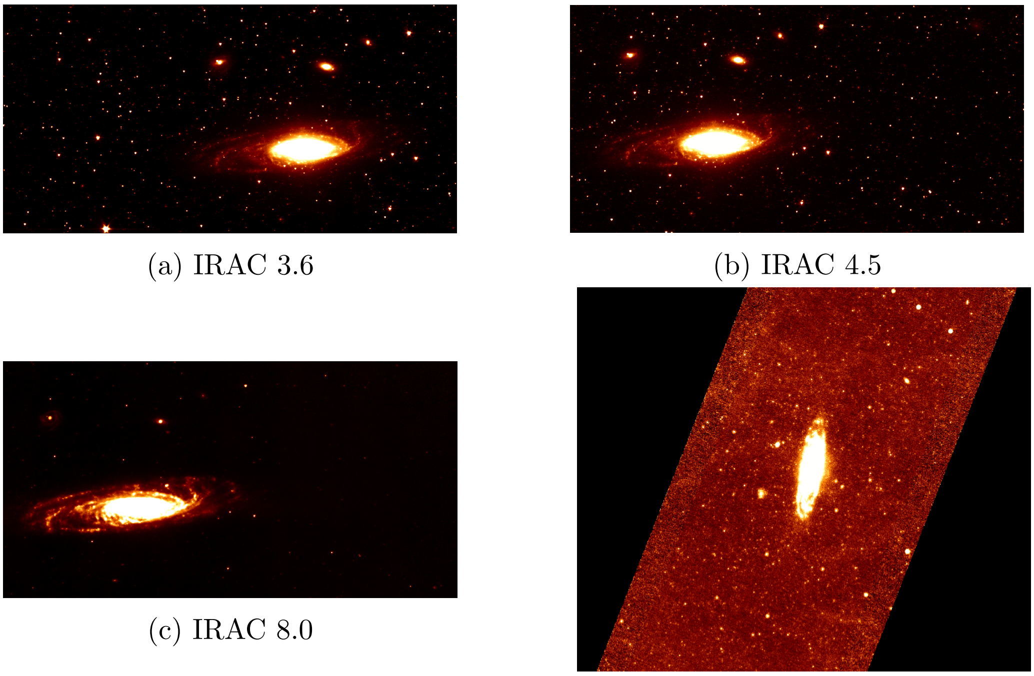

(a) IRAC 3.6

(b) IRAC 4.5

(c) IRAC 8.0

(d) MIPS 24

Figure 2.3: Images from the Spitzer telescope

2.2 Image processing

The images used have already been post-treated. However, before been able to calculate the luminosity profile, some operations have to be performed in the different images in order to extract the luminosity information effectively. For this purpose, the image processing software *MIDAS*, developed by the European Southern Observatory (ESO) [20], is used in this section.

2.2.1 Sizing and orientation of image

Since the images used in the development of this project come from different instruments, the pixel size is not uniform. Therefore, all the images have been through a linear rebinning process, in order to impose the smallest pixel size to all images, linearly interpolating the intensities for each pixel. The initial and final pixel sizes can be found in Table 2.2.

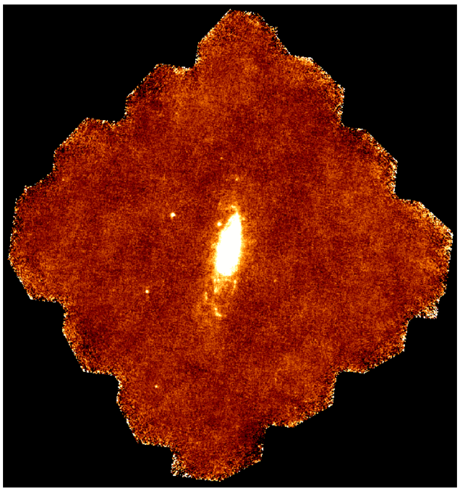

(a) PACS 70

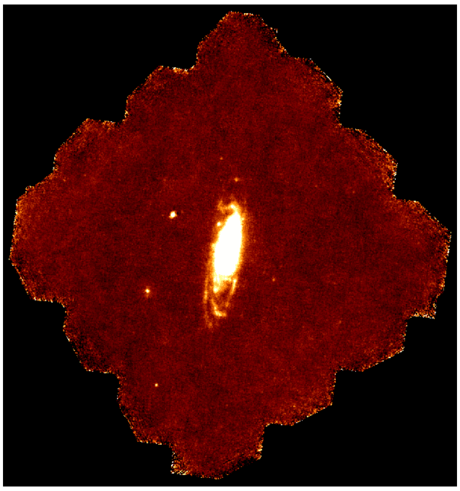

(b) PACS 100

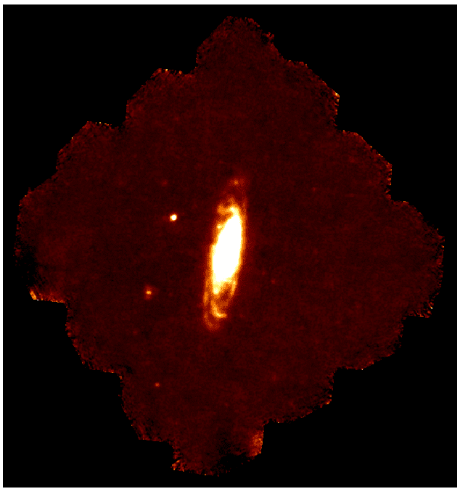

(c) PACS 160

Figure 2.4: Images from the Herschel telescope

Additionally, some of the images have a position angle (angle of the rows of pixels with respect to the North) different than 0. If this is the case, the position angle is specified in the FITS header. A rotation must be performed in order to align the upper part of the image with the North. The position angles of the different images can also be found in Table 2.2.

Spectral band	Initial pixel size (arcsec/pixel)	Final pixel size (arcsec/pixel)	Position angle (degrees)
FUV	1.5000	0.3960	0
NUV	1.5000	0.3960	0
u	0.3960	0.3960	148.484
g	0.3960	0.3960	148.696
r	0.3960	0.3960	148.265
i	0.3960	0.3960	148.375
z	0.3960	0.3960	148.591
IRAC3.6	0.7637	0.3960	73.6892
IRAC4.5	0.7576	0.3960	73.8076
IRAC8.0	0.7500	0.3960	73.5315
MIPS24	1.5000	0.3960	0
PACS70	1.4000	0.3960	0
PACS100	1.7000	0.3960	0
PACS160	2.8500	0.3960	0

Table 2.2: Pixel sizes and position angles of the different images

2.2.2 Coordinates of the center of the galaxy

The coordinates of the center of the galaxy in the different images are an essential piece of information in order to find the orientation and ellipticity of the galaxy, as well as to determine the luminosity as a function of the distance to the galactic center. For this purpose, a 2D-Gaussian was adjusted over the central bulge of the galaxy. The coordinates of the center of the Gaussian will be the ones of the center of the galaxy. This process can only be followed for those images where the bulge is distinguishable (visible, NIR and MIR). For the remaining images (UV and FIR), the coordinates of the center of the galaxy are obtained by matching several stars from the images where the coordinates of the center are known with the same stars of the image where these coordinates are still to be found. The coordinates of the center for the different images can be found in Table 2.3.

Filter	Center of the galaxy	
	x	y
FUV	1192.51	1198.09
NUV	1192.51	1198.09
u	1508.20	983.85
g	1509.42	989.10
r	1509.22	979.58
i	1508.30	982.65
z	1508.87	987.07
IRAC3.6	2025.78	561.19
IRAC4.5	985.61	599.61
IRAC8.0	996.09	586.13
MIPS24	3243.35	4672.54
PACS70	1972.30	2094.66
PACS100	1985.30	2106.32
PACS160	2026.18	2150.83

Table 2.3: Coordinates (in pixels) of the center of the galaxy in the different images

2.2.3 Extraction of the relevant image

For the purpose of this master thesis, the relevant area of the image to be analyzed is the one containing the galaxy. In order to achieve uniformity in the sizes of the images and in the relative position of the galaxy in them, a rectangular image centered in the center of the galaxy and with a size of 1200x2000 pixels has been extracted from each image. These resulting rectangular images are the ones to be used from now on.

2.2.4 Sky subtraction and star removal

Even though the images used in this master thesis have already been post-treated, a subtraction of the sky background is performed, avoiding any possible irregularities in the sky background and providing a more uniform starting point. After this, the resulting sky background has a mean value of zero for all images. The background to be subtracted is calculated with the help of the MIDAS software, by sampling the areas with no stars of the images and adjusting polynomials of degree 0, 1, 2 or 3 depending on the case[2]. This process is shown in Figure 2.5.

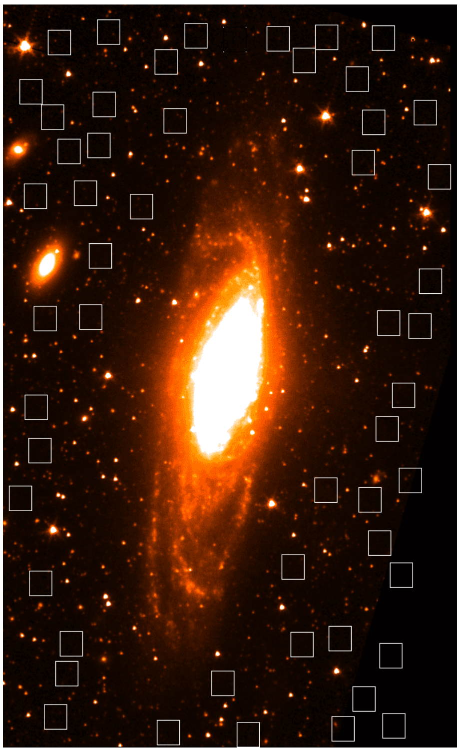

Figure 2.5: Removal of the sky background

In order to avoid the luminosity of foreground stars to be added to the luminosity profile of the galaxy, these stars have been removed using *MIDAS* [20].

[2]E.g., when the image seems to have a high background in one corner that decreases linearly towards the opposite corner, 1 degree polynomials in x and y would be enough to model the sky background. For the more complex situations, 2 and 3 degree polynomials have been used.

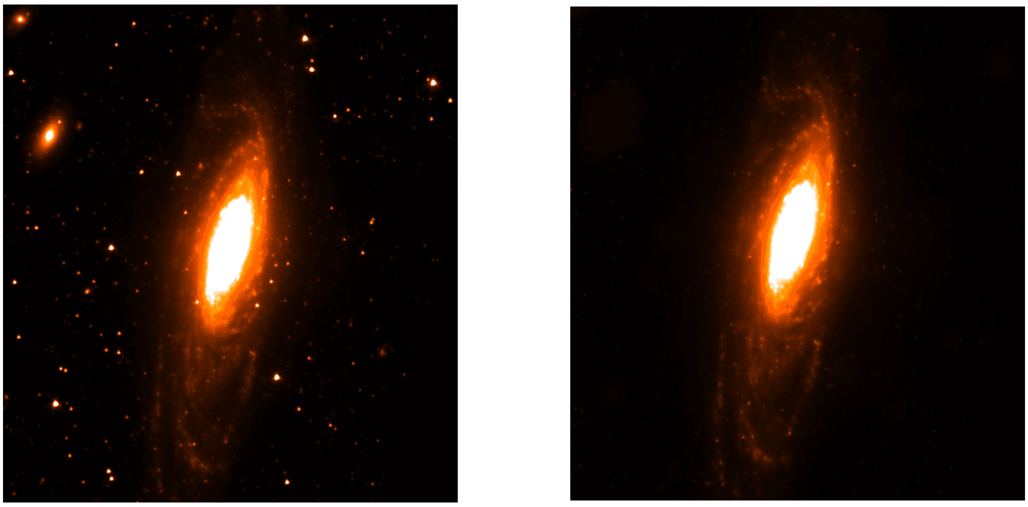

(a) Before star removal (b) After star removal

Figure 2.6: Images from Spitzer IRAC3.6 before and after star removal

2.2.5 Orientation of the galaxy

As mentioned in the introduction of this chapter, the galaxy is assumed to be circular. Since the line-of-sight is not perpendicular to the plane of the galaxy, what is seen in the images is an approximation of an ellipse with a certain semi-major and semi-minor axis. For clarity, a representation of these axes is shown in image 2.7.

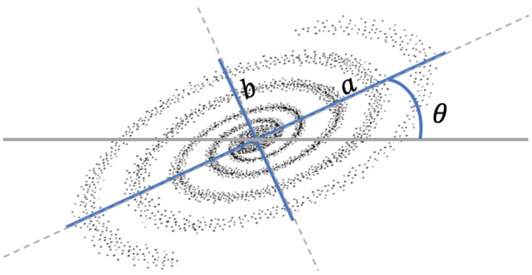

Figure 2.7: Scheme of the orientation of a galaxy

The orientation angle of the galaxy (θ) is defined as the angle between the horizontal (East) and the semi-major axis. To find this angle, the procedure developed by Biernaux *et al.* [21] was used. This consists in applying a circular mask divided in four quarters over the image, with the center of the circle at the center of the galaxy, as illustrated in Figure 2.8. The sum of the luminous intensity in the opposite quarters is registered for each orientation of the mask. When the difference of intensity between the pairs of quarters is at its maximum, the pair with higher luminosity is aligned with the major axis; and the pair with lower luminosity, with the minor axis. In the orientation in which the difference of intensity is equal to zero, the edges of the quarters overlap with the axes of the ellipse, and, since it is assumed that the galaxy has axial symmetry, the four quarters should be identical. The results of this process are shown in Figure 2.9.

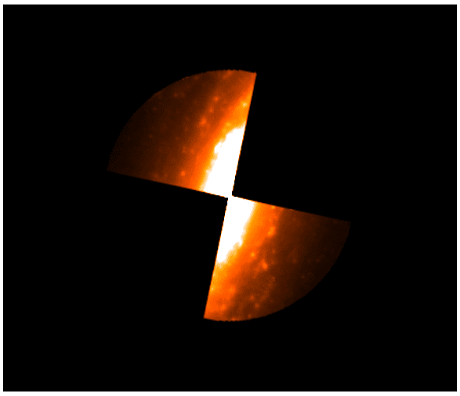

(a) Sectors I

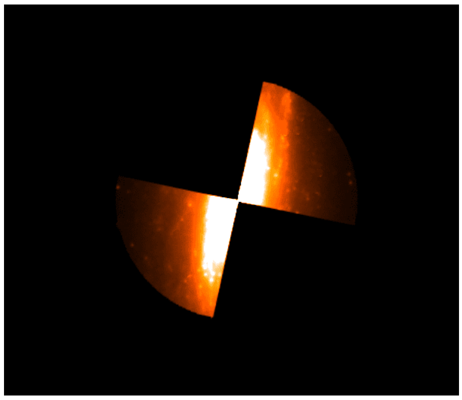

(b) Sectors II

Figure 2.8: Division in sectors to find the orientation at IRAC3.6 image

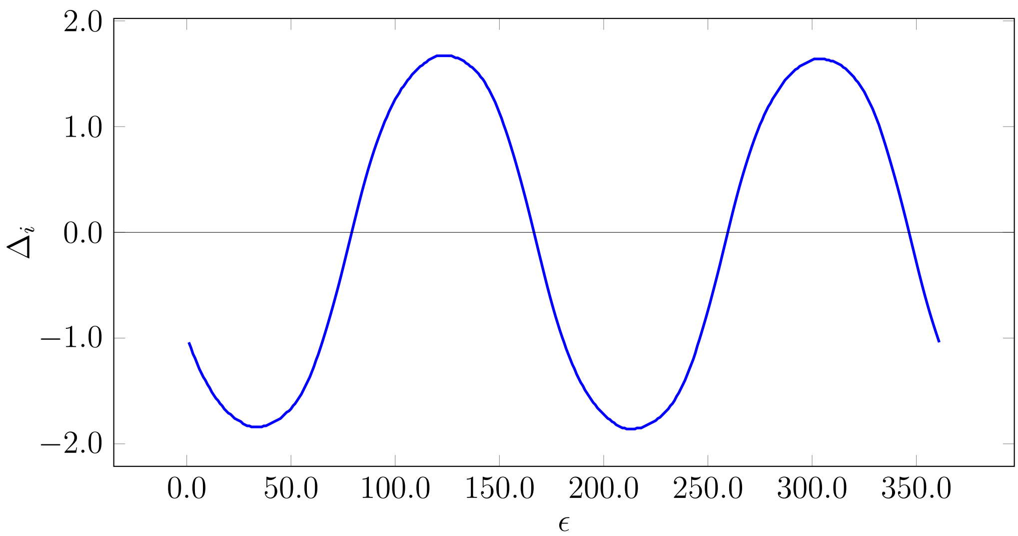

Figure 2.9: Orientation angle

The orientation angle obtained for NGC 7331 is then 80 ± 1 deg.

2.2.6 Ellipticity of the galaxy

As it was stated before, the galaxy is assumed to be circular, its apparent ellipticity being a question of perspective (the inclination of the line of sight with respect to the perpendicular of the galactic plane, i in Figure 2.10). However, this ellipticity is an essential piece of information to later build the isophotes that will allow to obtain the luminosity profile. The ellipticity ϵ is thus defined as:

$$\epsilon = 1 - \frac{b}{a} \tag{2.1}$$

with b and a the semi-minor and semi-major axes respectively. From the geometry, the inclination can be deduced as $i = \arccos(b/a) = \arccos(1 - \epsilon)$

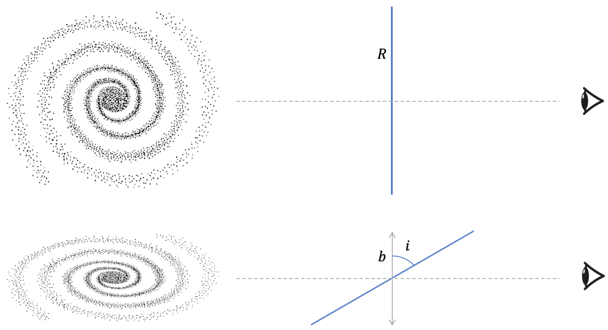

Figure 2.10: Scheme of the inclination-ellipticity of a galaxy

To calculate the ellipticity of the galaxy NGC 7331, a mask with the shape of an elliptical annulus, with variable ellipticity, is applied to the image, following the procedure developed by Biernaux *et al.* [21]. This mask is divided in four quarters, which are oriented with their bisecting lines superposed to the principal axes of the ellipse. The sum of luminous intensity of the opposite sectors normalized by the surface covered is registered for each value of the ellipticity.

The hypothesis here used is that the galaxy emits more light at the center than at the edge, and that this luminosity is the same for all the points in the galaxy that are at the same distance from the center (axial symmetry). Following this logic, if the value of ellipticity applied is smaller than the correct value, the sectors along the major axis (sectors I and III) show a part of the galaxy that is closer to the center (and thus, that has a higher luminosity) than the part shown by the sectors along the minor axis (sectors II and IV). The difference of luminosity between the sectors along the minor axis and the major axis (this result is called Δ_{ii}) is then positive. The opposite is true for a higher value of ellipticity. Therefore, when the ring acquires the correct value of ellipticity, all the sectors have the same value of normalized luminosity intensity and the difference of luminosity (Δ_{ii}) is thus zero.

In the visible and infrared images, some errors might be introduced by taking into account the out-of-plane luminosity of the bulge, which hides the luminosity coming from the left side of the galaxy. A first attempt to avoid these errors was to hide the sector IV for this calculation. In addition to this and with the same goal, the angle covered by each sector was modified to be higher than ninety degrees (specifically, 120 deg), making the sectors that cover the major axis more narrow. This is shown in Figure 2.11. However, the results obtained with this modification were not homogeneous nor satisfactory, which indicates that the contribution from the bulge could not be properly corrected.

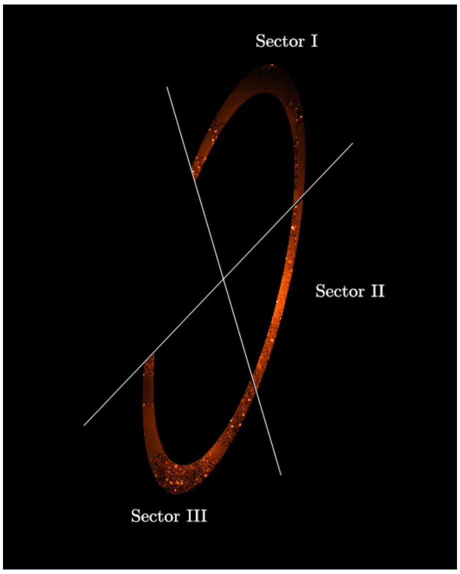

Figure 2.11: Sectors in the attempt of avoiding the luminosity of the bulge

Finally, since the luminosity of the bulge is much lower in the ultraviolet, and thus it does not contaminate the luminosities of further distances, the images from the GALEX telescope (both FUV and NUV) have been used to find the value of the ellipticity (Figure 2.12).

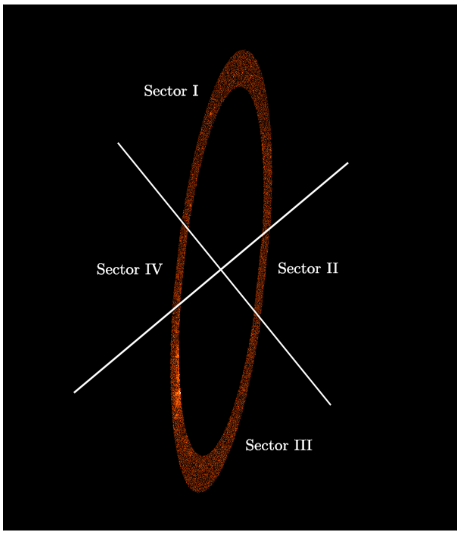

Figure 2.12: Sectors for the obtention of the ellipticity, NUV image

The result of this process is shown in Figure 2.13.

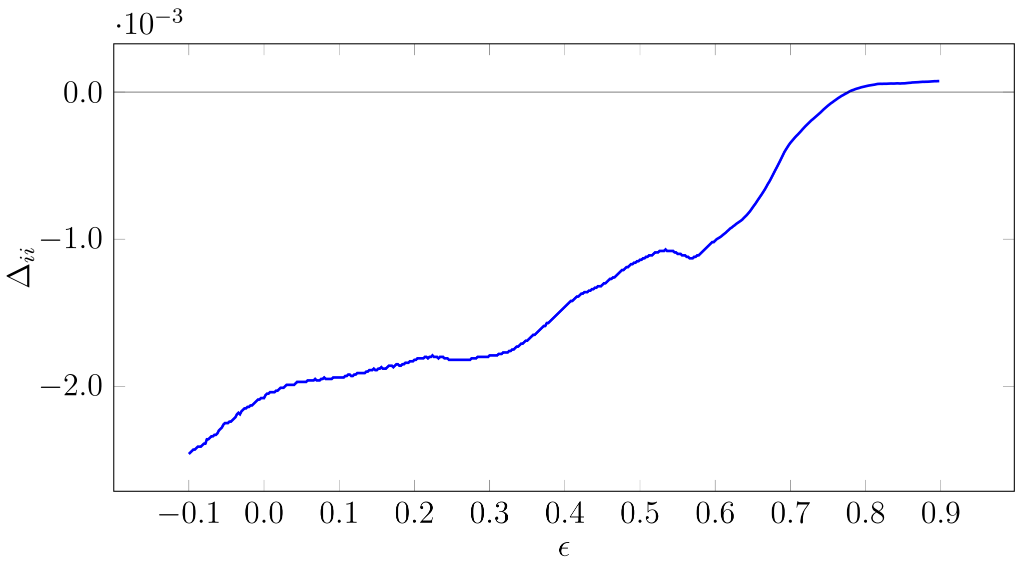

Figure 2.13: Ellipticity

The result of the ellipticity of the galaxy NGC 7331 is 0.78 ± 0.01. With this result, the inclination is then $i = \arccos(1 - 0.78) \simeq 77.3\,\text{deg}$.

2.3 Acquisition of the luminosity profile

In order to obtain the luminosity profile, a series of annuli with the calculated orientation and ellipticity are applied to the image of the galaxy. These rings are concentric and they increase in size from the very center to beyond the edges of the galaxy, and their width is selected so they are wide enough to contain representative information and narrow enough to contain the data relative to a specific distance. For each ring, the sum of the values of intensity in all pixels is obtained and then divided by the surface of the ring, obtaining thus a flux per unit surface.

The surface of the rings, *a priori* expressed in $pixels^2$, is converted to $arcsec^2$ to give it a physical meaning. Also, the flux units are different for the different instruments. Therefore, it is required to convert the variety of units to a selected unit, in this case, Janksy (Jy).

The values of the pixels for the GALEX telescope are given in $counts/s$. For the FUV filter, $1count/s = 1.40 \cdot 10^{-15} erg \cdot s^{-1} cm^{-2}$Å [22]. For the NUV filter, $1count/s = 2.06 \cdot 10^{-16} erg \cdot s^{-1} cm^{-2}$Å. With these units and since the effective wavelength is known, it is possible to convert to $ergs^{-1}cm^{-2}Hz^{-1}$ by multiplying by $\frac{\lambda^2}{c}$. Knowing that $1Jy = 10^{-23} ergs^{-1}cm^{-2}Hz^{-1}$, it is then simple to convert the data obtained by the GALEX telescope to Janksys. In order to express it in $Jy/arcsec^2$, this result is then divided by the surface of the annulus in $arcsec^2$.

In the case of the SDSS instrument, the intensities are expressed in *nanomaggies*. This unusual unit, a maggy (Mg), is the flux f of the source relative to the standard source f_0, which defines the zeropoint of the magnitude scale. The photometry of the SDSS was conceived to resemble the magnitude system AB[3], in which a magnitude 0 object should have the same counts as a source of $F_\nu = 3631Jy$. But in fact,

[3] The AB magnitude is defined as $m_{AB} = -2.5\log_{10}\left(\frac{flux_\nu}{3631Jy}\right)$, where $flux_\nu$ is the flux spectral density at the frequency ν.

the *zeropoints* of the SDSS system are slightly shifted from the AB standard [23]. Therefore, a corrective factor in needed in some cases: for the filters u and z. The corrective factor for the u filter is $-0.04mag$ ($u_{AB} = u_{SDSS} - 0.04$) and for the z filter is $+0.02mag$ ($z_{AB} = z_{SDSS} + 0.02$)[23, 24]. Then, the fluxes in *maggies* can be converted to Jy with the following expression:

$$flux[Jy] = 3631 \cdot flux[maggy] \cdot 10^{(correctivefactor)/-2.5} \tag{2.2}$$

This result is then divided by the surface of the annulus expressed in $arcsec^2$.

The pixel data from the Spitzer telescope are given in MJy/sr [25]. The *steradians* (sr, $1sr = 1rad^2$) can be converted to $arcsec^2$ by using the conversion factor $1sr = 4.25 \cdot 10^{10} arcsec^2$

To conclude, the data of the images from the Herschel telescope are given in $Jy/pixel$ [26]. By converting this pixel size to $arcsec^2$, these fluxes can thus be expressed in $Jy/arcsec^2$

These spectral flux densities per unit surface are multiplied by the respective effective frequencies. The results are shown below. Figure 2.14 illustrates the flux densities per unit surface obtained for the different filters.

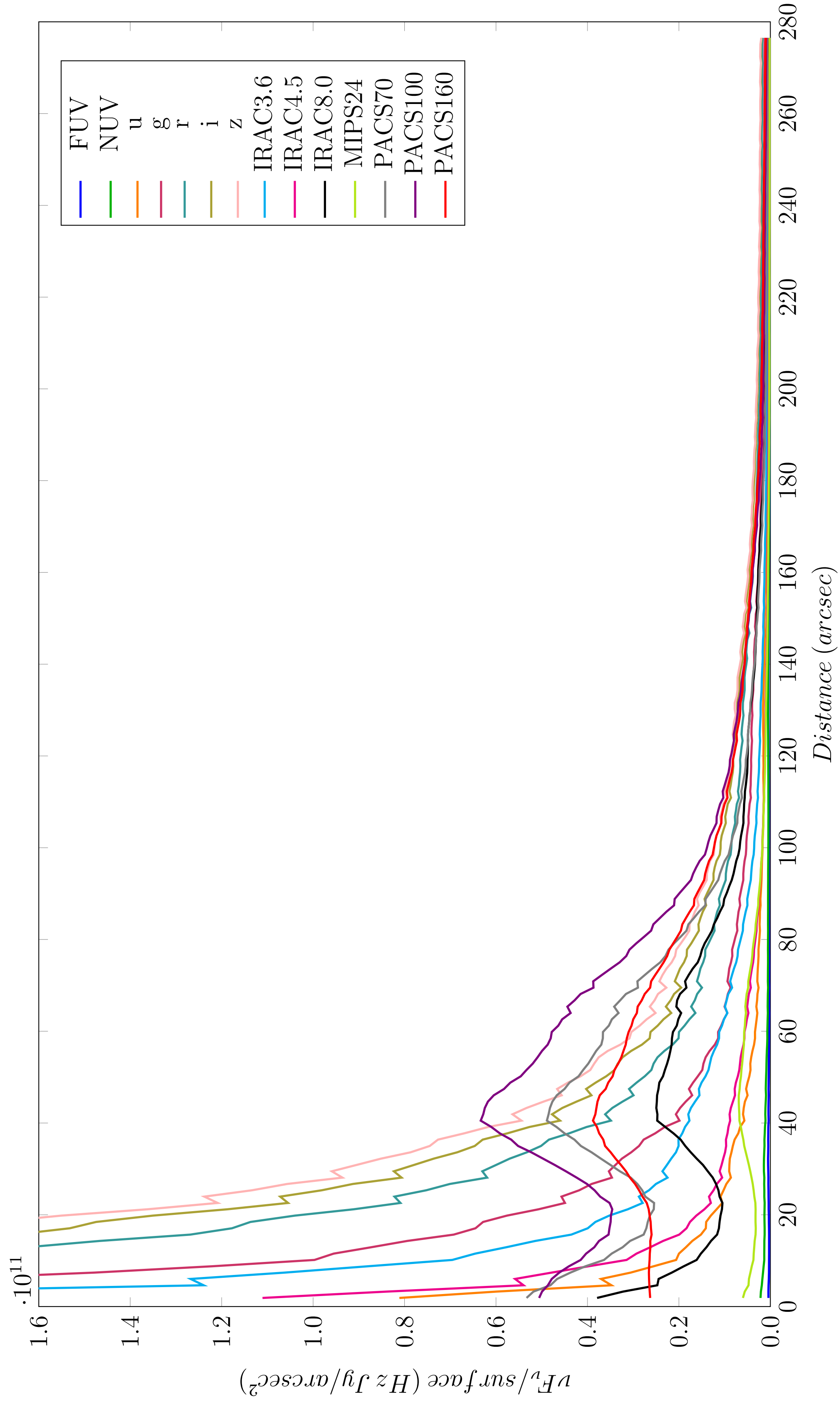

Figure 2.14: Luminosity profile of NGC 7331 before dust correction

Getting accurate error bars in the luminosities would be a long and tedious process, in particular because this model assumes circular symmetry and neglects the inhomogeneities due to the spiral arms. It was therefore decided to derive a simple estimate of the uncertainties on the final masses, as will be explained in Chapter 3, Section 3.4.

2.4 Correction for dust absorption

The incoming light from NGC 7331 is dimmed by the dust present in the galaxy, and also by the dust present in our galaxy that crosses the path of observation. For the first effect, a coefficient that characterizes the amount of dust absorbing light was calculated for each distance, in such a way that the absorption by dust in the ultraviolet and visible wavelengths is equal to the emission of light by this dust in the infrared. For the absorption by the dust in our own galaxy, the relevant coefficients were calculated with the extinction data present in the IRSA (NASA/IPAC Infrared Science Archive) database.

2.4.1 Dust in NGC 7331

The distribution of dust along the line-of-sight in the galaxy is unknown. The assumption used in that the stars and dust are more or less randomly mixed, such that the amount of ultraviolet and visible light absorbed in one specific direction is equal to the amount of far-IR light emitted by the heated dust in the same direction. With this objective, a black body curve is adjusted to the far-IR Herschel fluxes. Planck's law for the spectral density of radiation emitted by a black body in thermal equilibrium at temperature T is used for this purpose:

$$F_\lambda = A\frac{2hc^2}{\lambda^5}\frac{1}{\exp\frac{hc}{\lambda k_B T} - 1} \tag{2.3}$$

where $h = 6.626070 \cdot 10^{-34} Js$ is the Planck constant, $c = 2.99792458 \cdot 10^8 m/s$ is the speed of light, $k_B = 1.380648 \cdot 10^{-23} J/K$ is the Boltzmann constant, λ is the wavelength (expressed in m), T is the temperature of the black body to adjust, and A is a scale factor to adjust too. The adjusted temperature varies from $46K$ at the inner parts of the galaxy to $30K$ at the edge. The results are shown in Table A.1 To avoid confusion, this resulting flux will be called $F_{IR,emitted}$ later on.

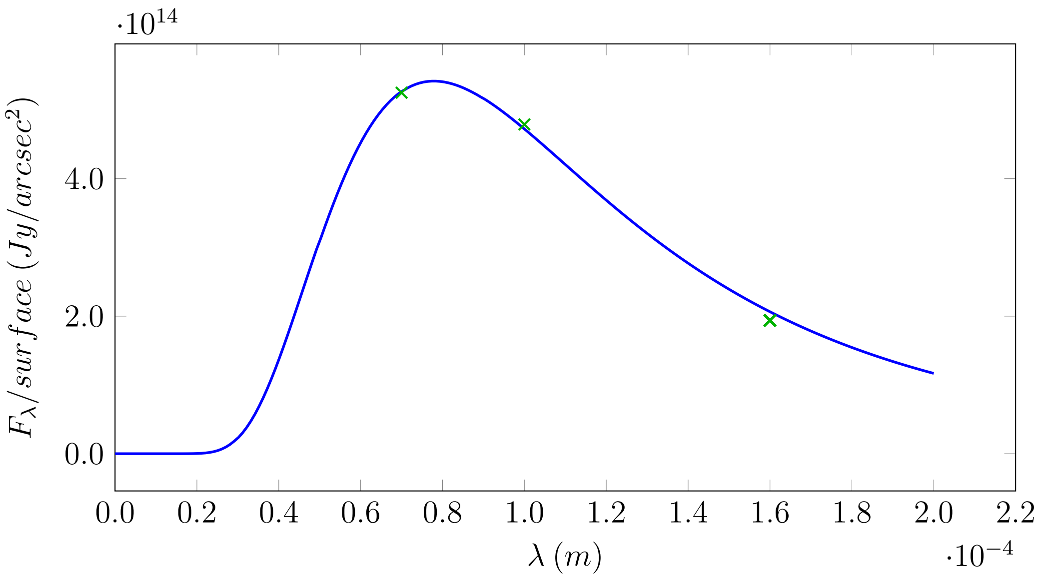

Figure 2.15: Blackbody fitting for the Herschel wavelengths at a distance of 60 arcsec

The extinction of light in the ultraviolet and visible is the difference between the integral of the real (corrected for dust) flux emitted by the galaxy at those wavelengths and the integral of the observed flux. The observed flux can be expressed in function of the real flux as follows:

$$F_\lambda = F_\lambda^* \cdot 10^{-C_{ext}(\lambda)\alpha} \tag{2.4}$$

where F_λ is the observed flux, F_λ^* is the flux corrected for the dust in NGC 7331 and

$C_{ext}(\lambda)$ are the coefficients for the dust models developed by Draine *et al.* [27, 28], shown in Table 2.4. Finally, α are the coefficients that need to be calculated.

Model for dust: C_{ext} selection

Draine *et al.* [28] propose 3 carbonaceous-silicate grain models that reproduce observed interstellar extinction, scattering and infrared emission. The coefficients of these models are shown in Figure 2.16 and in Table 2.4 for the selected wavelengths. When correcting the fluxes with any of these dust models for NGC 7331, unlike for Van de Vyvere's work [19], the obtained spectrum presents a NUV flux higher than the flux in the FUV and u filters. This is a consequence of the bump in the extinction curve at around 220nm (the wavelength of the NUV band is 227nm). The peak in the NUV flux becomes a problem at the next step: adjusting the spectrum to the stellar population models proposed by Maraston[4] [29]. Since the proposed spectra for the stellar population models do not present this characteristic, NGC 7331 FUV and NUV fluxes cannot be fitted simultaneously. Therefore, to avoid this problem the decision was to assume a classical $R_v = 3.1$ extinction, but without the bump at 220nm. This will have only little influence on the derived mass of the very hot stars, which are the ones that significantly contribute to the ultraviolet flux. The small number of these stars, despite their high mass, implies that their contribution to the total mass is rather modest. The *modified* extinction coefficient for the NUV flux is also shown in Figure 2.16 and Table 2.4.

Using the extinction coefficients in the last column of Table 2.4, the corrected luminosity profiles are obtained. The required α coefficients for this correction are the

[4] This process in explained in the next Chapter.

Filter	$C_{ext}(\lambda)$			
	$R_V = 3.1$	$R_V = 4.0$	$R_V = 5.5$	$R_V = 3.1$ modified
FUV	$1.275 \cdot 10^{-21}$	$1.100 \cdot 10^{-21}$	$9.480 \cdot 10^{-22}$	$1.275 \cdot 10^{-21}$
NUV	$1.439 \cdot 10^{-21}$	$1.438 \cdot 10^{-21}$	$1.309 \cdot 10^{-21}$	$1.090 \cdot 10^{-21}$
u	$8.037 \cdot 10^{-22}$	$8.468 \cdot 10^{-22}$	$8.718 \cdot 10^{-22}$	$8.037 \cdot 10^{-22}$
g	$5.968 \cdot 10^{-22}$	$6.808 \cdot 10^{-22}$	$7.625 \cdot 10^{-22}$	$5.968 \cdot 10^{-22}$
r	$4.155 \cdot 10^{-22}$	$5.007 \cdot 10^{-22}$	$5.920 \cdot 10^{-22}$	$4.155 \cdot 10^{-22}$
i	$3.136 \cdot 10^{-22}$	$3.840 \cdot 10^{-22}$	$4.606 \cdot 10^{-22}$	$3.136 \cdot 10^{-22}$
z	$2.390 \cdot 10^{-22}$	$2.929 \cdot 10^{-22}$	$3.507 \cdot 10^{-22}$	$2.390 \cdot 10^{-22}$
IRAC3.6	$2.257 \cdot 10^{-23}$	$2.694 \cdot 10^{-23}$	$3.369 \cdot 10^{-23}$	$2.257 \cdot 10^{-23}$
IRAC4.5	$1.444 \cdot 10^{-23}$	$1.814 \cdot 10^{-23}$	$2.369 \cdot 10^{-23}$	$1.444 \cdot 10^{-23}$
IRAC8.0	$1.307 \cdot 10^{-23}$	$1.429 \cdot 10^{-23}$	$1.714 \cdot 10^{-23}$	$1.307 \cdot 10^{-23}$
MIPS24	$9.461 \cdot 10^{-24}$	$1.012 \cdot 10^{-23}$	$1.163 \cdot 10^{-23}$	$9.461 \cdot 10^{-24}$
PACS70	$1.105 \cdot 10^{-24}$	$1.266 \cdot 10^{-24}$	$1.472 \cdot 10^{-24}$	$1.105 \cdot 10^{-24}$
PACS100	$5.076 \cdot 10^{-25}$	$5.447 \cdot 10^{-25}$	$6.241 \cdot 10^{-25}$	$5.076 \cdot 10^{-25}$
PACS160	$1.850 \cdot 10^{-25}$	$2.075 \cdot 10^{-25}$	$2.340 \cdot 10^{-25}$	$1.850 \cdot 10^{-25}$

Table 2.4: Extinction coefficients for the different dust models

ones that follow the next expression:

$$\int F_{IR,emitted} \mathrm{d}\lambda = \int F^*_\lambda \mathrm{d}\lambda - \int F_\lambda \mathrm{d}\lambda \iff \int F_{IR,emitted} \mathrm{d}\lambda = \int (10^{-C_{ext}(\lambda)\alpha} - 1) F_\lambda \mathrm{d}\lambda \tag{2.5}$$

Once the α coefficients have been calculated, these can be applied to the observed fluxes to find the corrected fluxes with Eq. 2.4

2.4.2 Dust in the Milky Way

Finally, the correction for the absorption of dust of the Milky Way is performed. To do this, it is necessary to know the amount of dust in our galaxy when looking on the direction of NGC 7331. The extinctions (in magnitude) by dust in the Milky Way in a given direction and for different spectral bands can be found in the database Galactic Dust Reddening and Extinction at IRSA (NASA/IPAC Infrared Science Archive) [30]. These extinctions (A_λ) for the relevant case are given for the SDSS

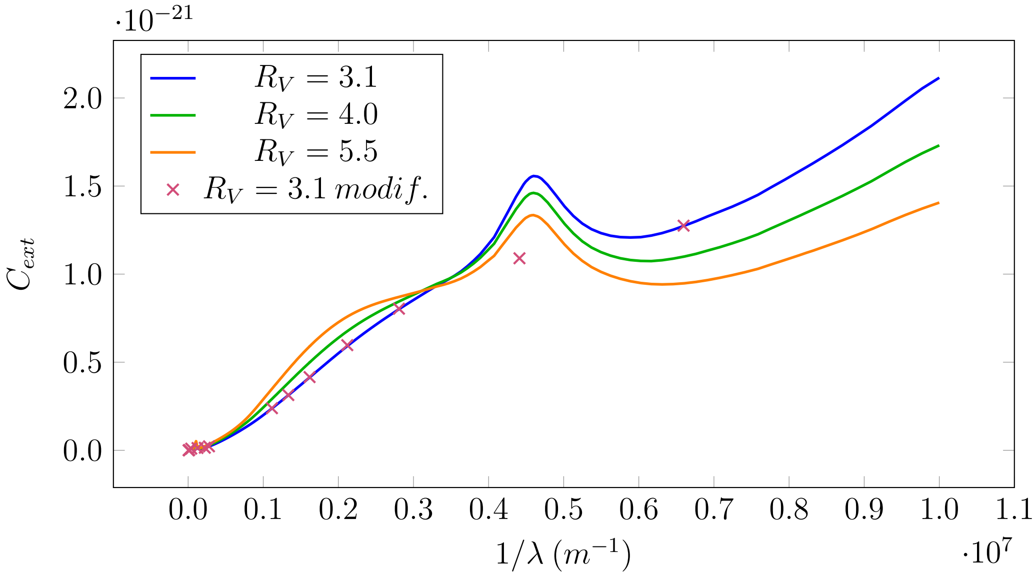

Figure 2.16: Coefficients of extinction by dust in the different models

Filter	A_λ
u	0.386
g	0.301
r	0.208
i	0.155
z	0.115

Table 2.5: Extinctions for the SDSS filters in the Milky Way

bands, among others (Table 2.5). The correction for dust in the Milky Way can be expressed with a β coefficient, similar to the α coefficients used in the previous section:

$$F_\lambda = F_\lambda^{**} \cdot 10^{-C_{ext}(\lambda)\beta} \tag{2.6}$$

where F_λ is the observed flux, F_λ^{**} is the flux corrected for the dust in the Milky Way, $C_{ext}(\lambda)$ are the coefficients for the dust model of $R_v = 3.1$ and shown in Table 2.4, and β is the required coefficient. In this case, the β coefficient does not depend on the distance to the center of the galaxy.

To obtain this β coefficient from the extinction data found at the IRSA database, the following expression proposed by Draine and Draine *et al.* is used [27, 31]:

$$A_\lambda = 2.5 \log \left(\frac{F_\lambda^{**}}{F_\lambda} \right) \tag{2.7}$$

Therefore, with Eqns. 2.6 and 2.7:

$$F_\lambda^{**} = F_\lambda \cdot 10^{C_{ext}(\lambda)\beta} = F_\lambda \cdot 10^{A_\lambda/2.5} \implies \beta = \frac{A_\lambda}{2.5 \cdot C_{ext}(\lambda)} \tag{2.8}$$

with $C_{ext}(\lambda)$ the extinction coefficients for the $R_V = 3.1$ model.

Since β shall not depend on the wavelength, the mean value for the five calculated values (five A_λ data points, for SDSS) is then used. Finally, the flux corrected for the dust both in the Milky Way and in NGC 7331 is obtained with the following expression:

$$F_\lambda^0 = F_\lambda \cdot 10^{(C'_{ext}(\lambda)\cdot\alpha + C_{ext}(\lambda)\cdot\beta)} \tag{2.9}$$

2.5 Results

The resulting fluxes for all filters are shown in this section. Figures 2.17 to 2.20 show the luminosity profiles in each spectral band, after the correction for dust absorption, and Figure 2.21 shows all luminosity profiles in the same graph. These results can also be found in Appendix A, in Tables A.2, A.3 and A.4.

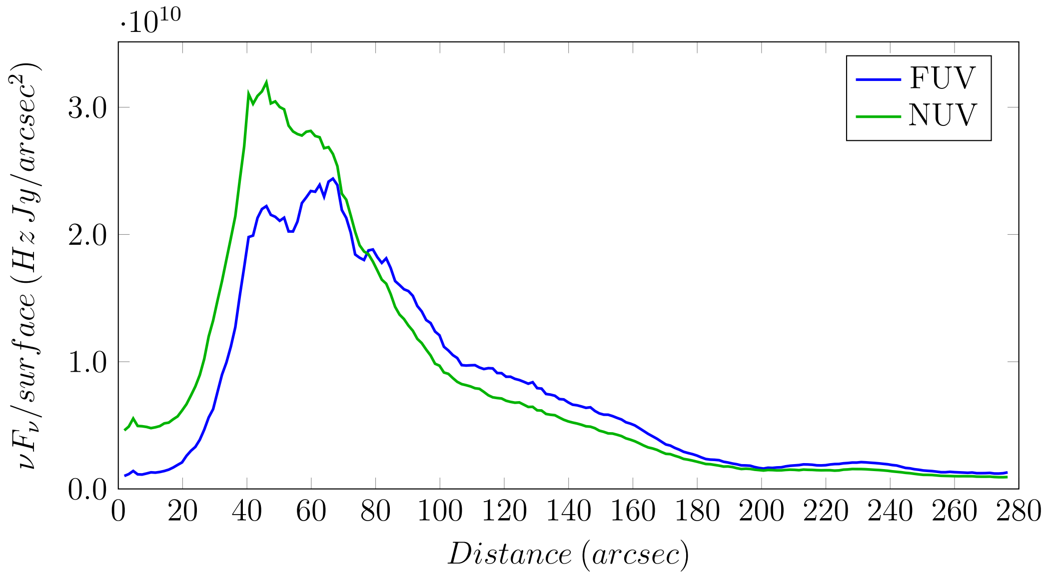

Figure 2.17: Luminosity profile for the GALEX filters in NGC 7331

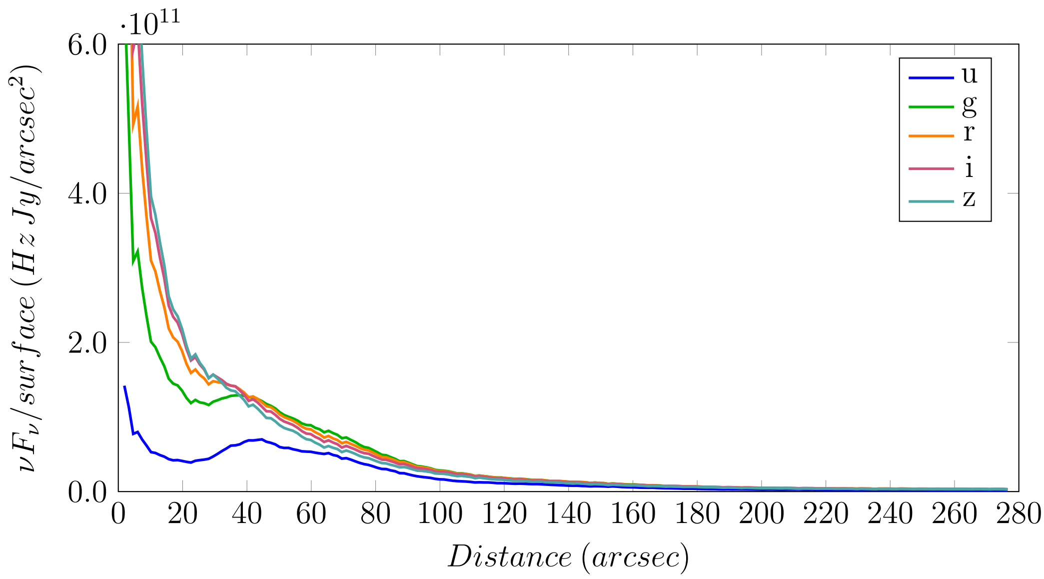

Figure 2.18: Luminosity profile for the SDSS filters in NGC 7331

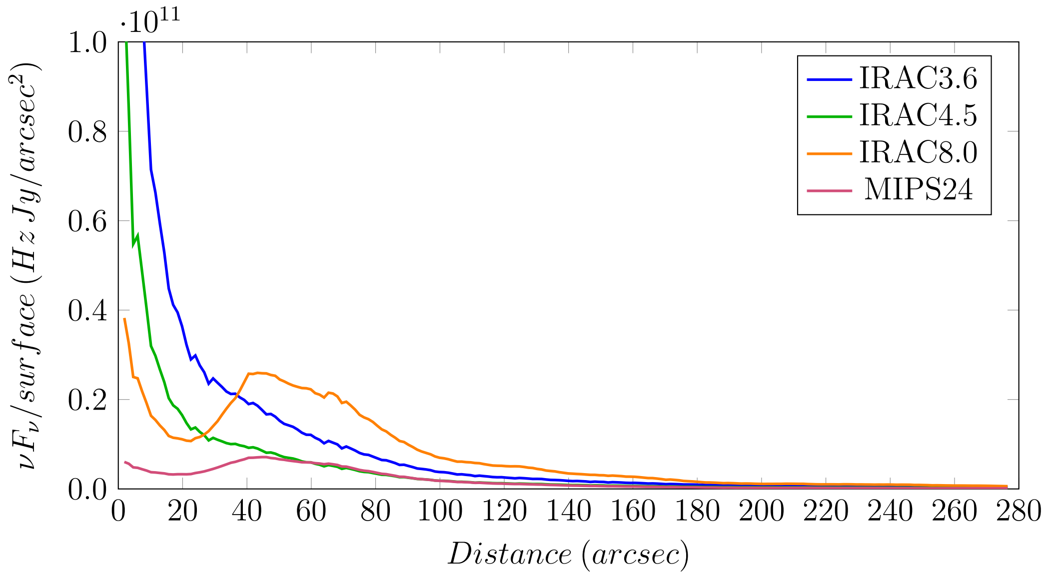

Figure 2.19: Luminosity profile for the Spitzer filters in NGC 7331

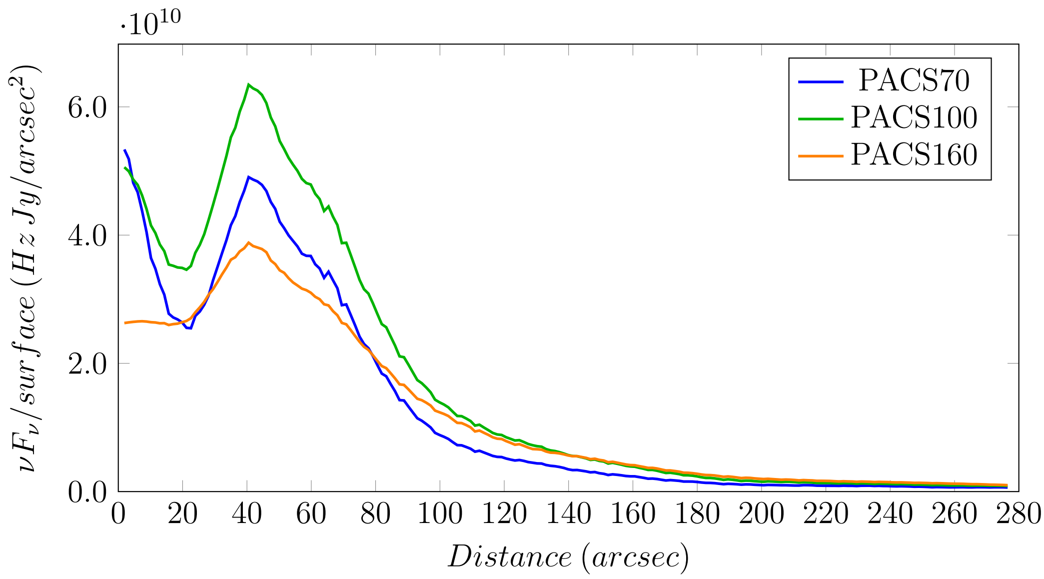

Figure 2.20: Luminosity profile for the Herschel filters in NGC 7331

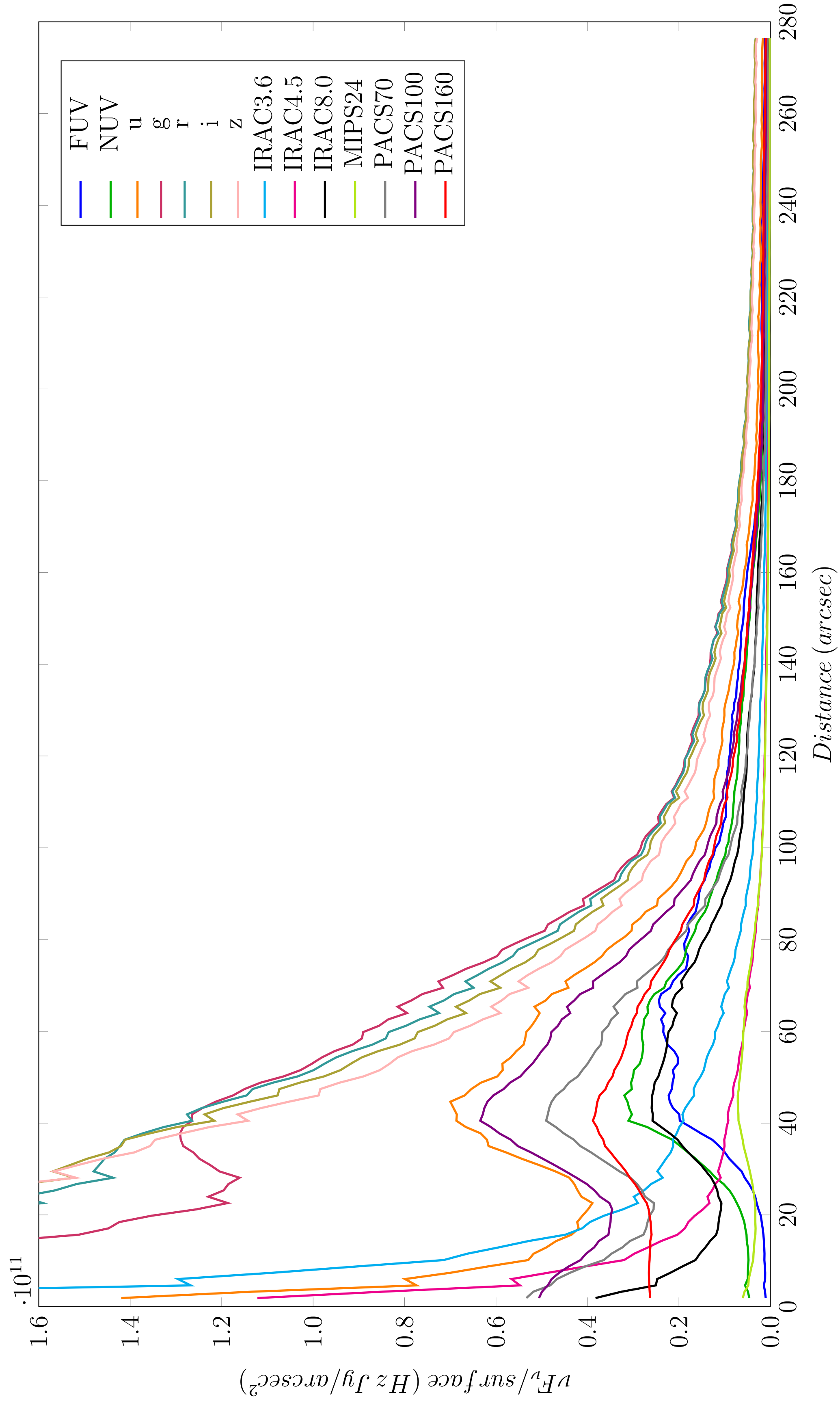

Figure 2.21: Luminosity profile of NGC 7331 after dust correction

Chapter 3

Mass profile

In this chapter, the mass profile of the galaxy is calculated. In first place, Maraston's stellar population models are used to obtain the stellar mass profile from the luminosities previously calculated. Then, with the data for the distribution of gas for NGC 7331, the mass of HI clouds and H_2 is determined. Finally, the mass of helium is taken into account, assuming cosmological abundances. Unless stated otherwise, the same methodology as Van de Vyvere [19] is followed in this Chapter.

3.1 Adjustment to the stellar population model

The *Evolutionary Population Synthesis* (EPS) is a technique used by Maraston to model the spectrophotometric properties of stellar populations, using the knowledge of stellar evolution [29, 32]. In her work, Maraston calculates the spectra of *Simple Stellar Populations* (SSP) for a wide range of ages, metallicities, initial mass functions (Kroupa or Salpeter), and horizontal branch morphologies (*red/intermediate* or *blue*).

The initial mass function (IMF) is a probability density function that describes the initial distribution of stellar masses that form in one star formation event in a given volume of space. For this study, the Kroupa function has been selected, which is similar to the older Salpeter function, the main difference being a smaller proportion of low mass stars ($M < 0.5M_{\odot}$), which presented problems in the Salpeter initial mass function [33]. The Salpeter IMF consists in a power law (of the type $a \cdot m^{-\alpha}$, with m being the mass) [34]. In contrast, the one proposed by Kroupa consists in several segments of different power laws, for different mass categories [35].

Both available horizontal branch morphologies (*red/intermediate* and *blue*) provide very similar spectra. Therefore, either one of them could have been used for the calculations. The morphology chosen for the horizontal branch is *red/intermediate*.

The metallicity Z in general terms is defined as the abundance in a certain object of elements heavier than hydrogen and helium. The choice of the metallicity ($[Z/H] = +0.00$, corresponding to $Z = 1.0Z_{\odot}$) is justified later on.

To compare the fluxes computed by Maraston with the ones calculated in the previous chapter, it is necessary to obtain the resulting spectra for the Maraston data after going through the appropriate filters. This is, filters FUV and NUV from GALEX, filters u, g, r, i and z from SDSS, and filters IRAC3.6 and IRAC4.5 from Spitzer. The remaining Spitzer and Herschel filters are not relevant, since the emission in this spectral domain is mainly produced by dust and not stars. The transmission curves for the filters can be found in the SVO Filter Profile Service [36, 37, 38]. Using the *observation module* of the python library *synphot* for synthetic photometry, the source spectra are convolved with the provided bandpases [39]. Additionally, a factor of correction for the distance to the galaxy (14.7 Mpc [16]) is necessary to be able to compare these fluxed with the ones obtained in the previous chapter, since the spectra of Maraston are integrated at the surface of the star. In the previous chapter, the results were obtained in $\nu \cdot F_{\nu}/surface$. To uniformize the results, these need to be divided by the surface of the different rings. By doing that, these results become dependent of the distance to the center of the galaxy.

This process is followed for all the metallicities provided (this is, $[Z/H] = -2.25$, -1.35, -0.33, $+0.00$, $+0.35$ and $+0.67$). The expected metallicity for this galaxy is around zero or slightly negative. The different results are compared with the observed fluxes, in order to select the right metallicity. In particular, the ratio of luminosity of the SDSS z band and the Spitzer IRAC3.6 seems to be a determinant factor. For the metallicities with $[Z/H] < +0.00$, this ratio is larger than the one found at the observations[1]. Therefore, the smallest metallicity that is able to reproduce the observed fluxes is $[Z/H] = +0.00$. Hence, the populations corresponding to this value of metallicity are selected.

To adjust these Maraston fluxes for each distance to the fluxes obtained in the previous chapter, the first approach was to create groups of stars by intervals of age, and to adjust the proportions of each group in an attempt to reproduce the observed fluxes in the different spectral bands. However, since the spectrum of the younger ages varies a lot from one age to the next, the results for this method were unsatisfactory.

A different approach, providing a more realistic representation of the physical phenomena, was then considered. This approach consists in the modeling of the stellar population using one or more bursts of stellar formation [19]. The adjustable parameters for this model are the intensity of the peak of the burst, the moment when this burst occurred and the rate of decrease. The function used to shape the exponential decrease for this purpose is the following:

$$f_{decrease}(t) = \exp\left(-\frac{t - t_0}{\tau}\right) \tag{3.1}$$

The result of combining this function with a step function is shown in Figure 3.1,

[1]The calculated fluxes show a ratio of $flux_z/flux_{3.6} \simeq 6$. The smallest number for this ratio, for $[Z/H] = -2.25$, -1.35, -0.33 and $+0.00$ is around 11, 10, 8 and 6 respectively.

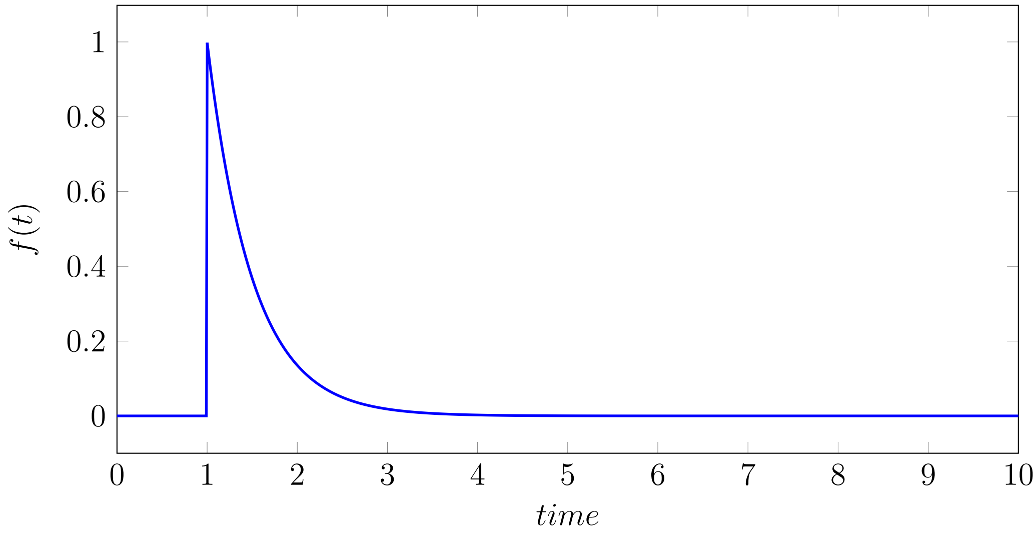

Figure 3.1: Exponential decrease function (Eq. 3.1) combined with Heaviside

for $I = 1$, $t_0 = 1$, $\tau = 0.5$.

This introduces a non-physical discontinuity at t_0. To avoid it, the following function was used to shape the growth of the bursts:

$$f_{growth}(t) = \frac{1}{1 + \exp\left(-\frac{t-t_0}{\tau_{growth}}\right)} \tag{3.2}$$

Which is, in practical terms, a step with softened edges. The shape of this function is shown in Figure 3.2, for $I = 1$, $t_0 = 1$, $\tau_{growth} = 0.1$. The τ_{growth} controls the steepness of the growth: decreasing its value means getting closer to the Heaviside function. For the development of this master thesis, a τ_{growth} of 0.02 was used.

The resulting burst function is, therefore:

$$f_{burst}(t, I, t_0, \tau) = I \frac{\exp\left(-\frac{t-t_0}{\tau}\right)}{1 + \exp\left(-\frac{t-t_0}{\tau_{growth}}\right)} \tag{3.3}$$

The shape of this burst function is shown in Figure 3.3, for $I = 1$, $t_0 = 1$, $\tau = 0.5$, $\tau_{growth} = 0.1$.

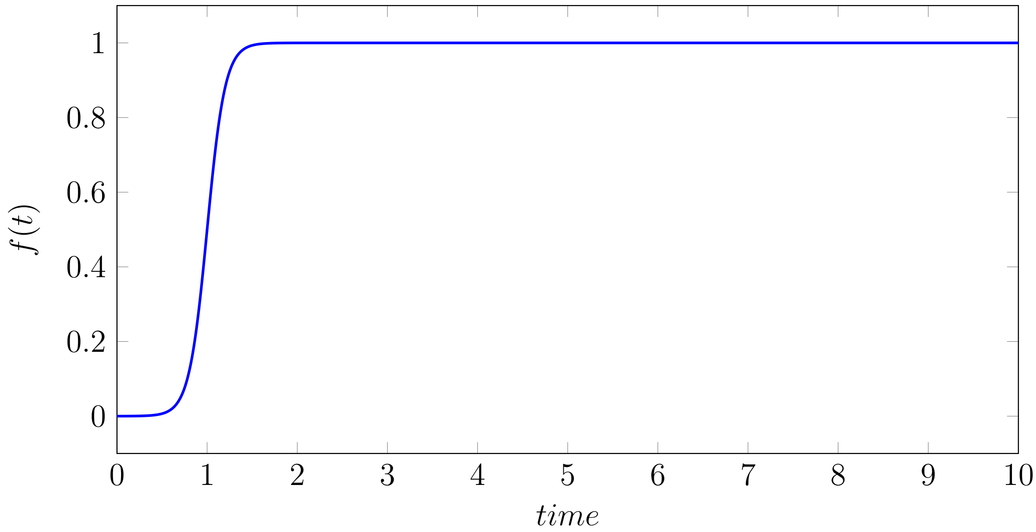

Figure 3.2: Growth function, *smooth Heaviside* (Eq. 3.2)

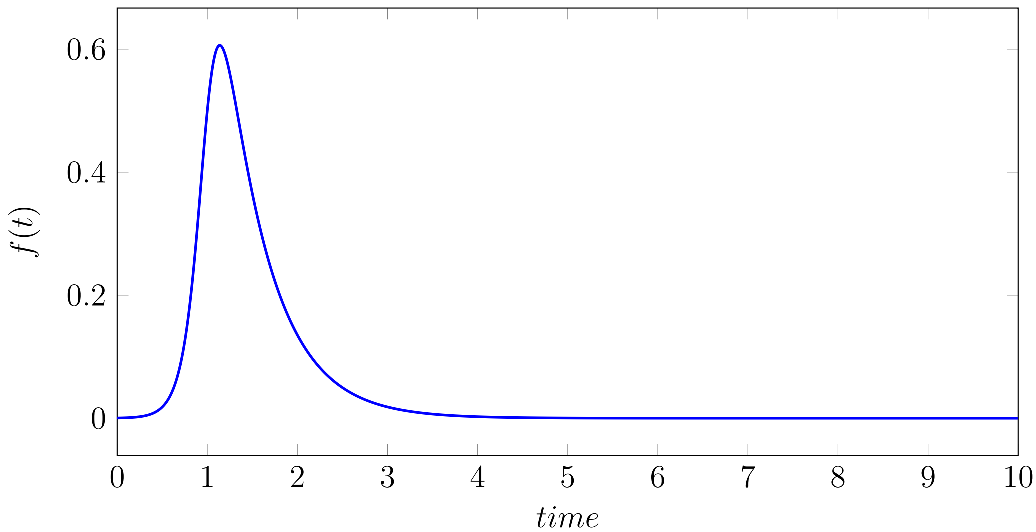

Figure 3.3: Burst function, combination of growth and decrease function (Eq. 3.3)

For a model on n bursts, the final function to adjusted is expressed as a sum of the individual bursts.

$$y(t) = \sum_{i=1}^{n} I_i \frac{\exp\left(-\frac{t-t_{0,i}}{\tau_i}\right)}{1+\exp\left(-\frac{t-t_{0,i}}{\tau_{growth}}\right)} \tag{3.4}$$

This function represents the amount of stars at time t in a star population.

To obtain the flux for the ensemble of stars in a given wavelength, this expression is multiplied by the flux of each star of a given age and this result is then integrated over time to find the total flux. The latter is then integrated over each filter bandpass. The aim of using these burst models is to find a fit that, ideally, for each filter,

$$flux_{obs,filter} = \int y(t) \cdot flux_{Maraston,filter} \mathrm{d}t \qquad \forall filtre \tag{3.5}$$

In practice, an adjustment by the method of least squares is adopted to minimize the difference between the observed flux and the Maraston flux in each filter.

Before performing any additional calculations, a closer examination of the spectra of the observations is taken, in order to estimate the number of bursts and the first guess for the time of the bursts. From the data obtained in the previous chapter, it is possible to make a clear distinction between the shape of the spectrum for the distances within the bulge and the shape of the spectrum for the distances external to the bulge (at the galactic disk). This noticeable difference is depicted in Figures 3.4 and 3.5. Is therefore evident that the spectra for all the distances in the galaxy cannot be adjusted with only one burst. A model with two bursts is then considered.

By taking a closer look at the Maraston spectra, and comparing it with the shape of the spectra of the observed flux (Figures 3.4 and 3.5), the first conclusion to extract is that the bulge of the galaxy is mainly composed of old stars. Figure 3.6[2] shows

[2] The spectra depicted in Figures 3.6 and 3.7 correspond to a distance to the center of the galaxy of 57 *arcsec*. However, a change in this distance (a change in the surface of the ring) will only result in a change of scaling factor, but the shape of the curve will be the same. Therefore, the conclusions here extracted are valid for the Maraston spectra for all distances.

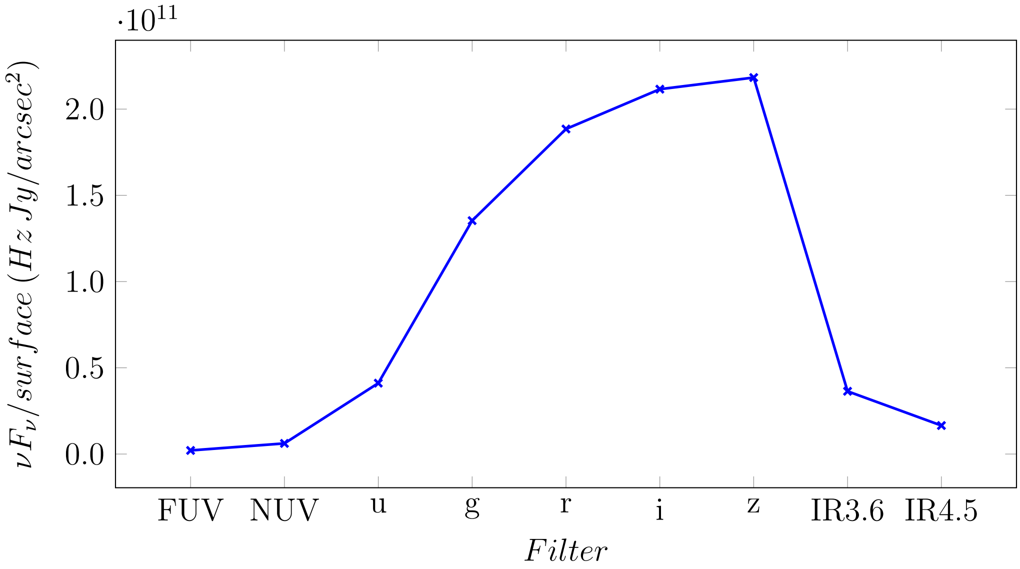

Figure 3.4: Luminosity profile for a distance inside the bulge (20 *arcsec*)

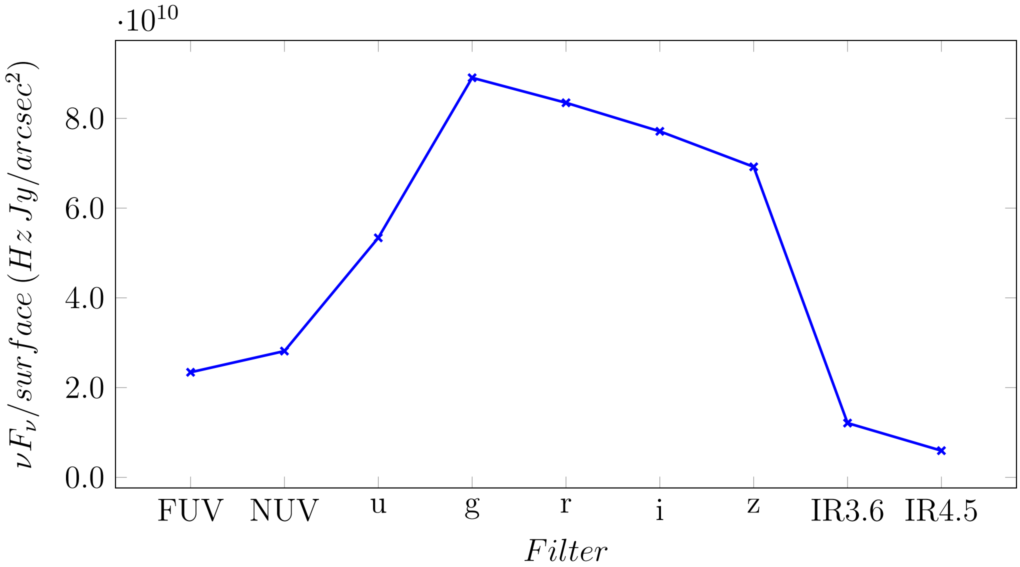

Figure 3.5: Luminosity profile for a distance corresponding to the disk (60 *arcsec*)

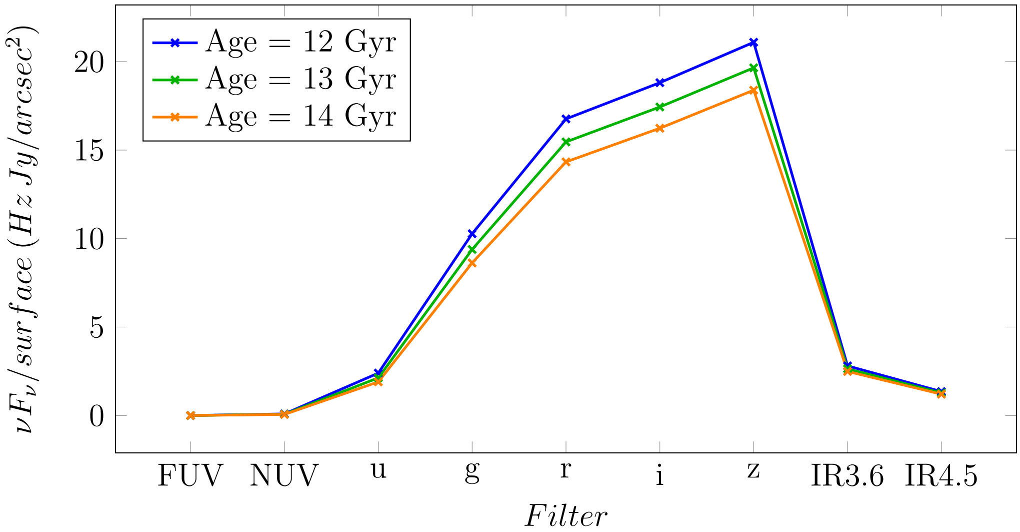

Figure 3.6: Maraston spectra for old stars between 12 and 14 *Gyr*

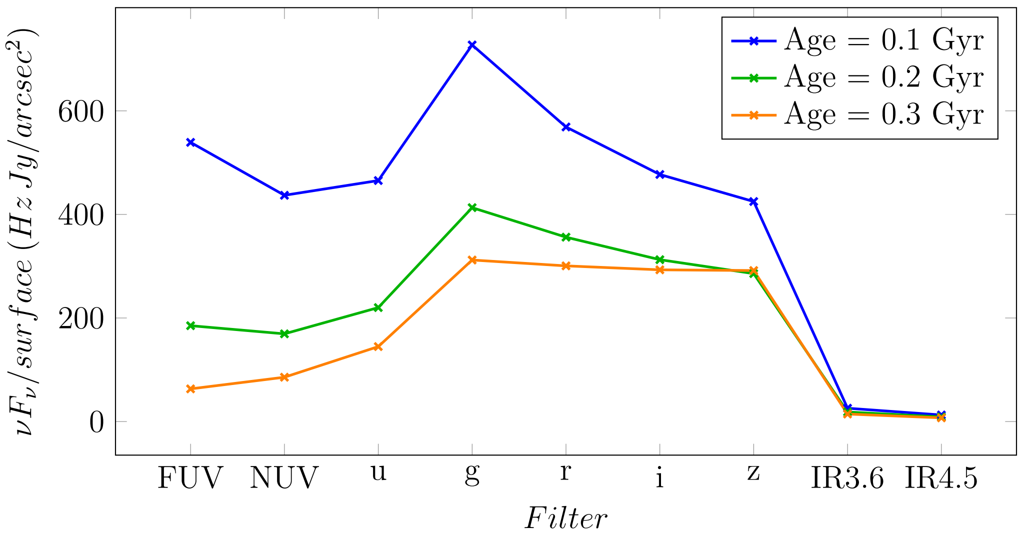

Figure 3.7: Maraston spectra for young stars between 0.1 and 0.3 *Gyr*

that the spectrum is not very sensitive to a change around these ages (old stars evolve slowly). A first guess of $t_0 = 13Gyr$ is then selected.

For the observations of the galactic disk, the flux in the *SDSS g* band is the dominant one. To find a comparable shape within the Maraston spectra, much younger stars have to be considered. As shown in Figure 3.7, for these smaller ages the spectrum is very sensitive to a change in age. Because of the similarity in the general shape, a $t_0 = 0.2Gyr$ is selected as a first guess for this second, younger burst.

The optimization for each distance is then performed, using the *simulated annealing* algorithm from the *Global Optimization Toolbox* in Matlab [40, 41]. This algorithm is a global optimization method for solving unconstrained and bound-constrained optimization problems with a probabilistic heuristic approach.

The results of the burst function for different distances, and the fitting of the spectra for the distances of 20 and 90 *arcsec* are shown in Figures 3.8, 3.9 and 3.10 respectively. The evolution of the *intensity* parameters with distance is shown in Figure 3.11. All the results for the different parameters are shown in Table B.1.

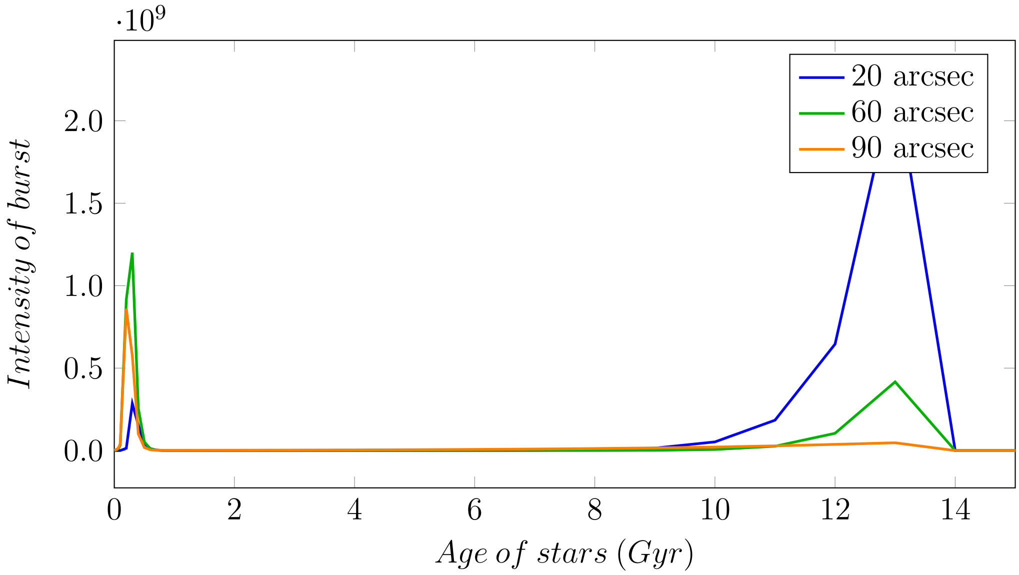

Figure 3.8: Result of the burst function for the distances of 20, 60 and 90 arcsec

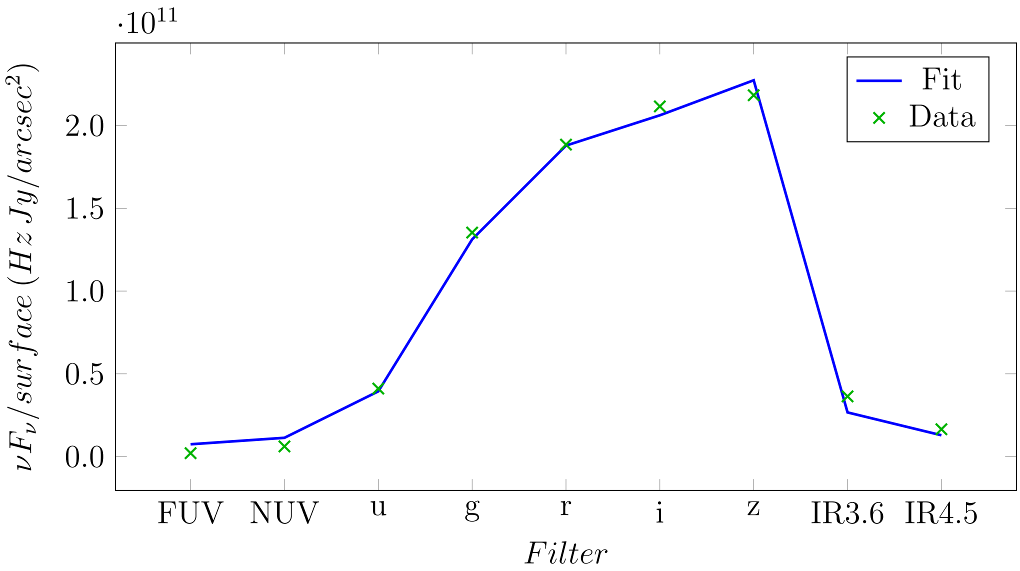

Figure 3.9: Adjustment of the spectrum at a distance of 20 arcsec

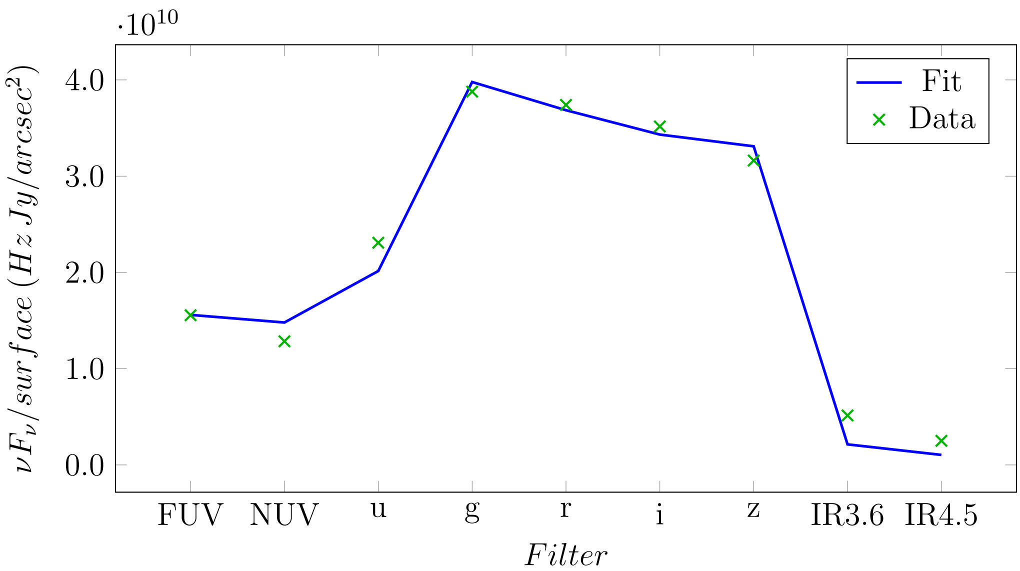

Figure 3.10: Adjustment of the spectrum at a distance of 90 arcsec

3.2 Calculation of the stellar mass

Once the model of the stellar population for NGC 7331 is obtained for each distance to the galactic center, this population can be associated with its corresponding mass, calculated as well by Maraston [29, 32]. Maraston provides a breakdown of the mass

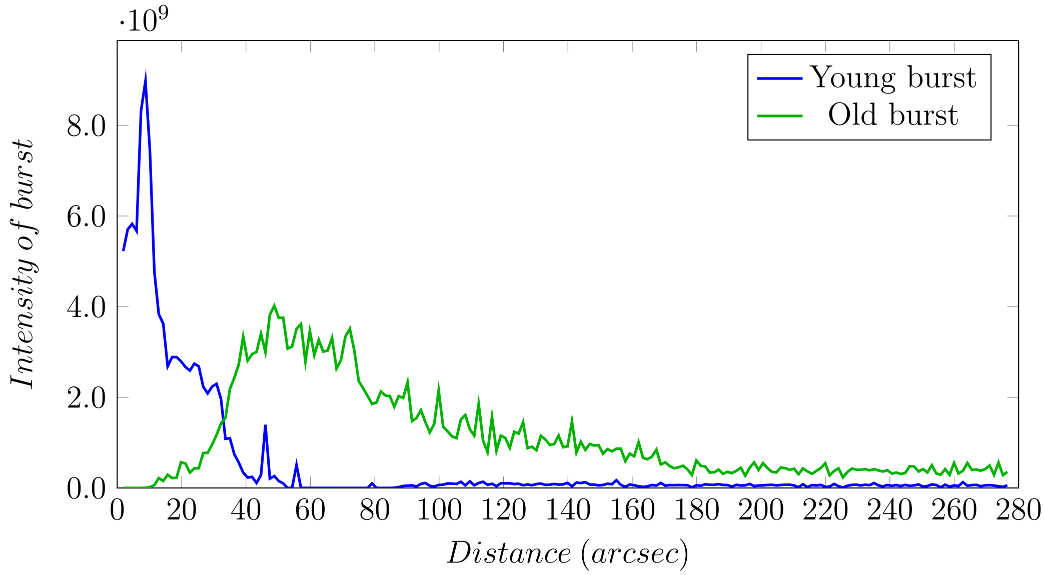

Figure 3.11: Evolution of the intensities of the two bursts with the distance to the galactic center.

in the following categories: alive mass, mass of white dwarfs (WD), mass of neutron stars (NS), mass of black holes (BH).

Using the parameters computed in the previous section, the mass of the different categories and the total mass can be obtained as follows:

$$mass_{calc,category} = \int y(t) \cdot mass_{Maraston,category} \mathrm{d}t \qquad \forall category \tag{3.6}$$

The results for the different stellar categories are shown in Figure 3.12 and Table B.2 of the Appendix B. In Table B.3 and Figure 3.13, the mass of the older stars, formed at the old burst, is shown independently from the mass of the stars formed at the young burst. This separation allows to clearly identify the stars in the bulge (where old stars dominate) and those belonging to the galactic disk (mostly young stars). The total stellar mass in NGC 7331 is $7.463 \cdot 10^{10} M_{\odot}$, with $4.207 \cdot 10^{10} M_{\odot}$ from the old burst and $3.256 \cdot 10^{10} M_{\odot}$ from the young burst.

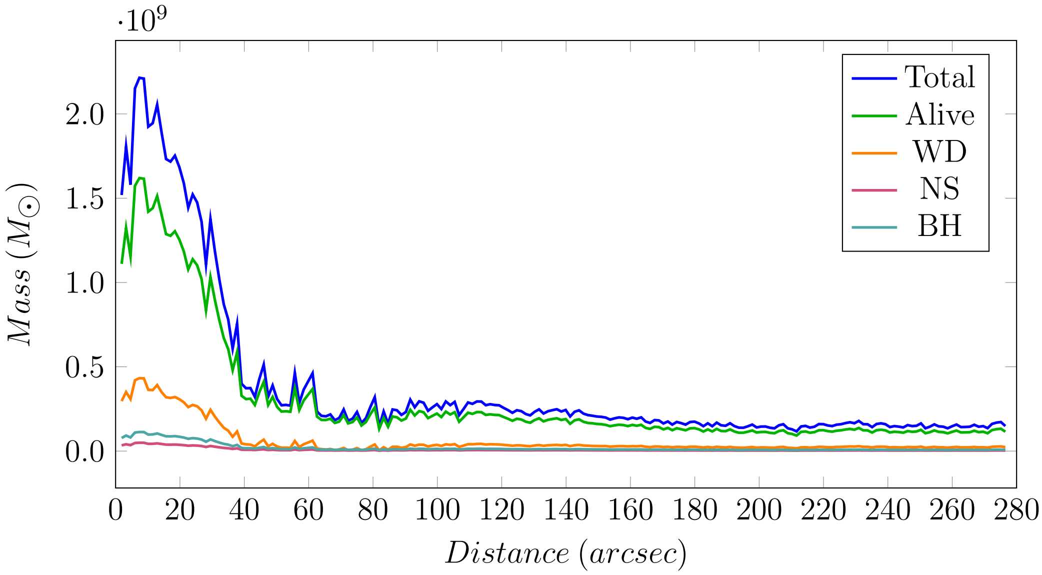

Figure 3.12: Mass profile for the total stellar mass, the alive mass, white dwarfs, neutron stars and black holes in NGC 7331

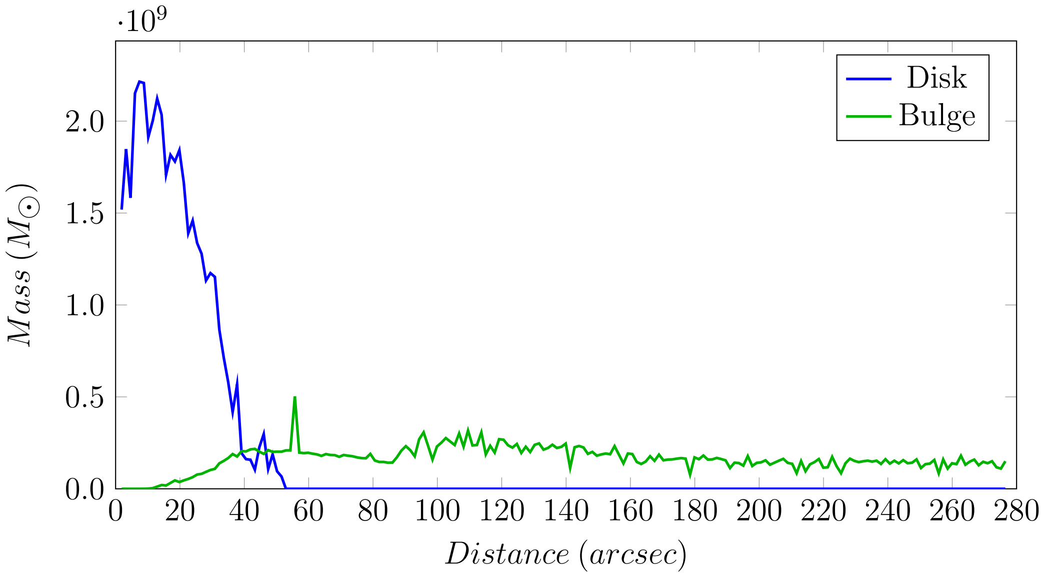

Figure 3.13: Mass profile of the two burst model for galaxy NGC 7331

3.3 Calculation of the mass of gas

Additionally to the mass of the stars, the mass of the gas of the galaxy is also calculated to be added to the mass profile of the galaxy. More specifically, the mass of neutral hydrogen, molecular hydrogen and helium are estimated with the help of the data obtained from the literature.

3.3.1 Mass of HI

The clouds of neutral atomic hydrogen (HI) produce a 21-cm line, observable in the radio-wave domain. The observations of this line allow for the estimation of the surface density of neutral atomic hydrogen in NGC 7331. Bosma [42] mapped the galaxy NGC 7331 in the 21-line, and the results of his studies are shown in Figure 3.14.

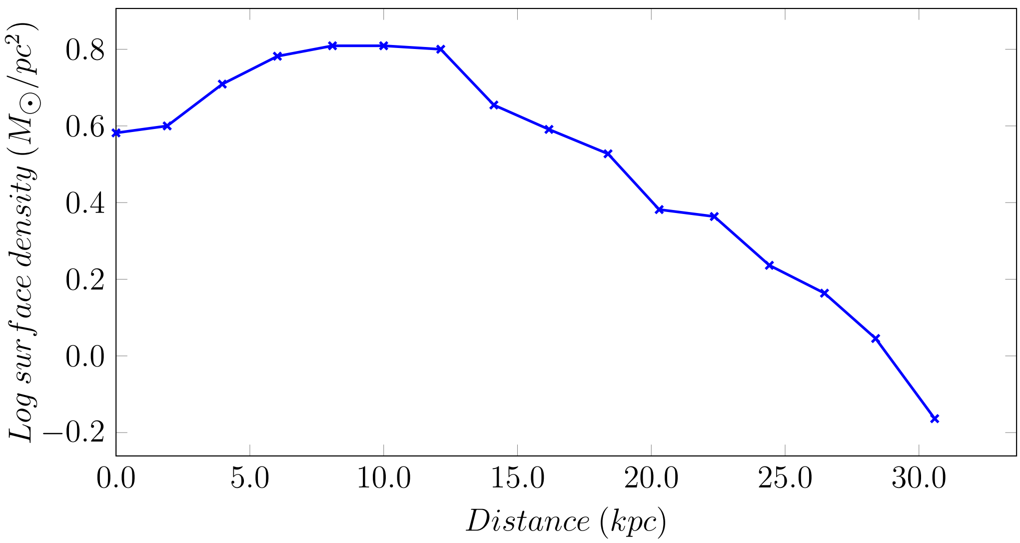

Figure 3.14: Logarithm of the surface density of neutral atomic hydrogen, as observed by Bosma

By converting these data into the units used in the previous section and interpolating, the mass of HI in each ring is calculated. The result of this is shown in Table B.3 and Figure 3.16. The total mass of neutral atomic hydrogen in this galaxy is $1.260 \cdot 10^9 M_\odot$.

3.3.2 Mass of H_2

The surface density of molecular hydrogen was estimated by Leroy *et al.* [43] from CO line emission, assuming a constant CO-to-H2 conversion factor. The data for the molecular hydrogen (H_2) is available is a similar way as HI[43], as shown in Figure 3.15.

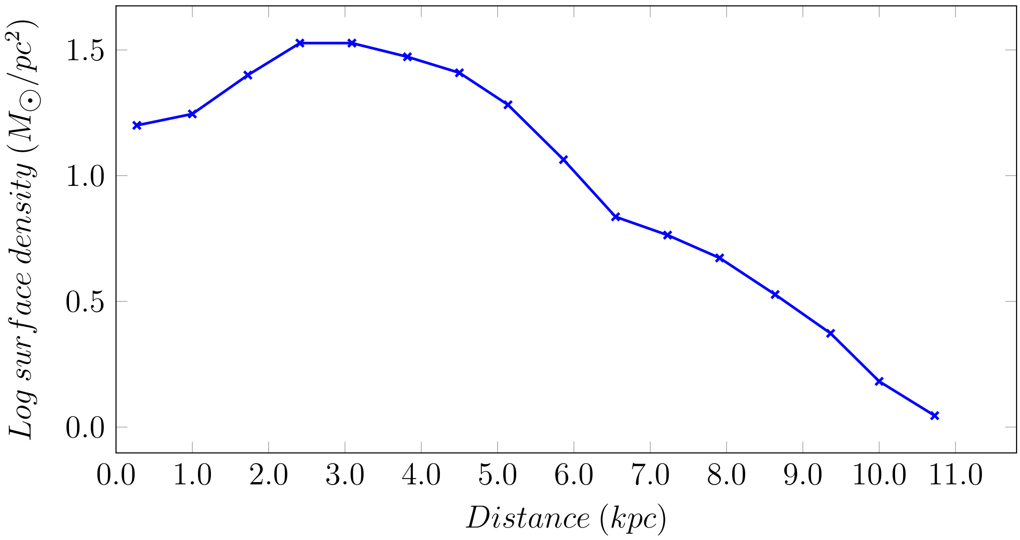

Figure 3.15: Logarithm of the surface density of molecular hydrogen, as observed by Leroy *et al.*

Unlike for neutral atomic hydrogen, the data for molecular hydrogen is only available up to $11kpc \simeq 150arcsec$. After this distance, it is considered negligible. The results for the mass of molecular hydrogen are shown in Table B.3 and Figure 3.16. The total mass of H_2 in NGC 7331 is $7.832 \cdot 10^8 M_\odot$.

3.3.3 Mass of He

To estimate the mass of helium in the galaxy, cosmological abundances are assumed. This hypothesis underestimates the mass of helium present in the galaxy, since the stars produce additional helium. The result obtained by Izotov *et al.* [44] of the mass fraction of primordial helium, $Y_p = 0.2551 \pm 0.0022$, are used to calculate the mass of helium, from the mass of neutral atomic and molecular hydrogen. The estimation of the mass of helium in the galaxy is $6.998 \cdot 10^8 M_\odot$. The results for each distance are shown in Table B.3 and Figure 3.16.

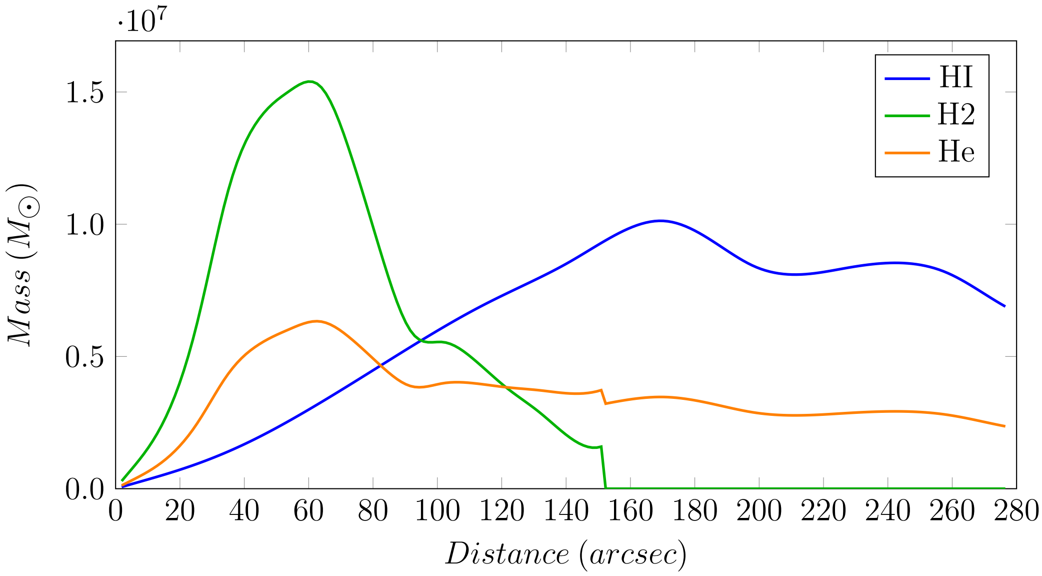

Figure 3.16: Mass profile of neutral atomic hydrogen, molecular hydrogen and helium in galaxy NGC 7331

3.4 Results

The resulting mass profile in shown in this section. Figure 3.17 shows the mass profiles of the different elements and Figure 3.18 shows the total mass profile with error bars. To estimate the errors at each distance, the deviation with the mean value of the contiguous annuli was calculated. Since the mass is proportional to the flux,and the relative error on the emitted flux is twice the relative error on the distance[3], a relative error on the mass of twice the relative error of the distance [45] was applied as a lower bound.

[3]The flux is the energy per unit surface, so the observed flux is the emitted flux diluted on the surface of a sphere whose radius is the distance between the emitter and the observer. Therefore, $\ln(F_{observed}) - \ln(F_{emitted}) = const. - \ln(d^2)$. Differentiating, for a fixed $F_{observed}$: $\delta F_{emitted}/F_{emitted} = 2 \cdot \delta d/d$. The ϵ_r on the emitted flux in then $2 \cdot \epsilon_r$ on the mass.

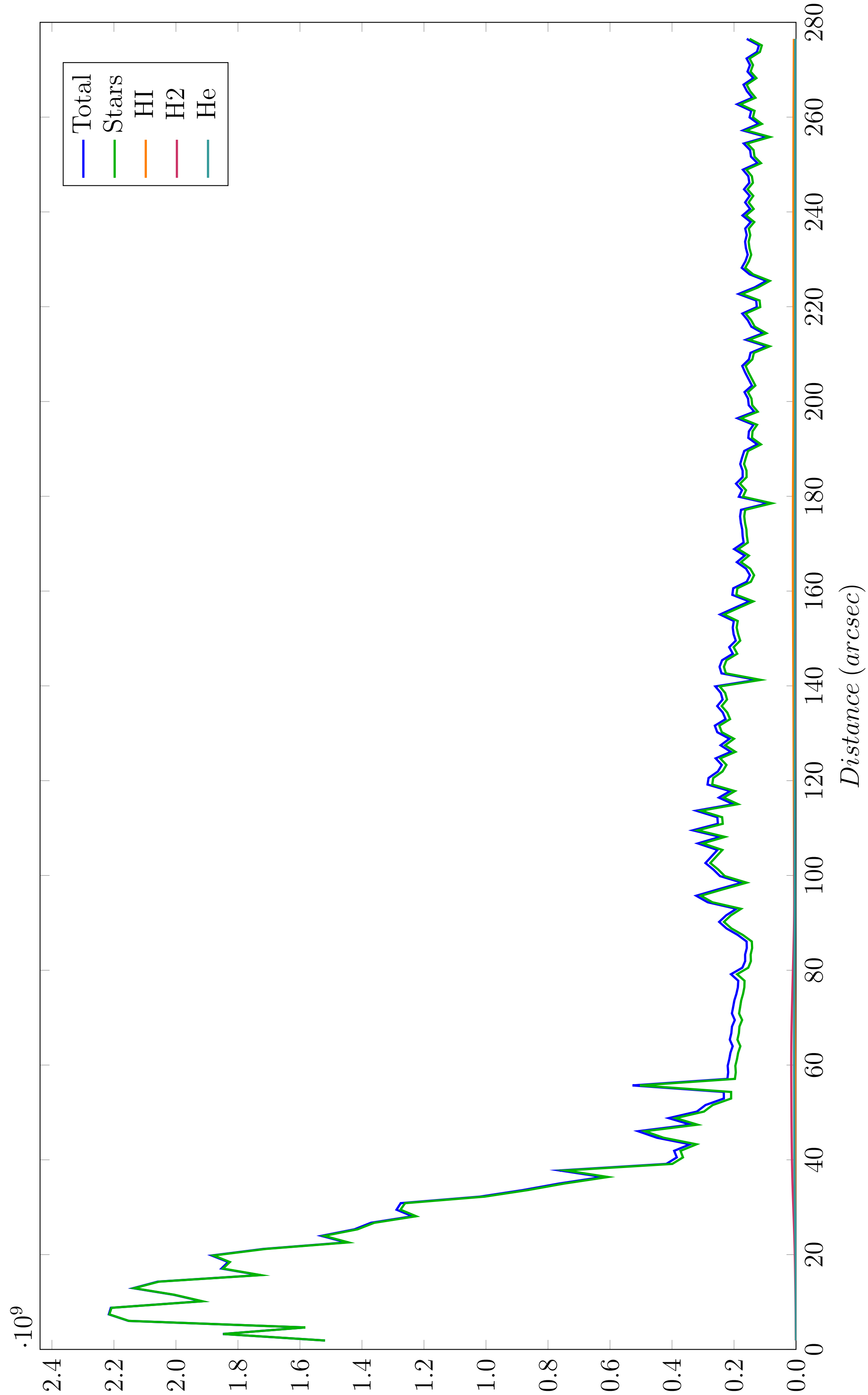

Figure 3.17: Profile of mass of NGC 7331

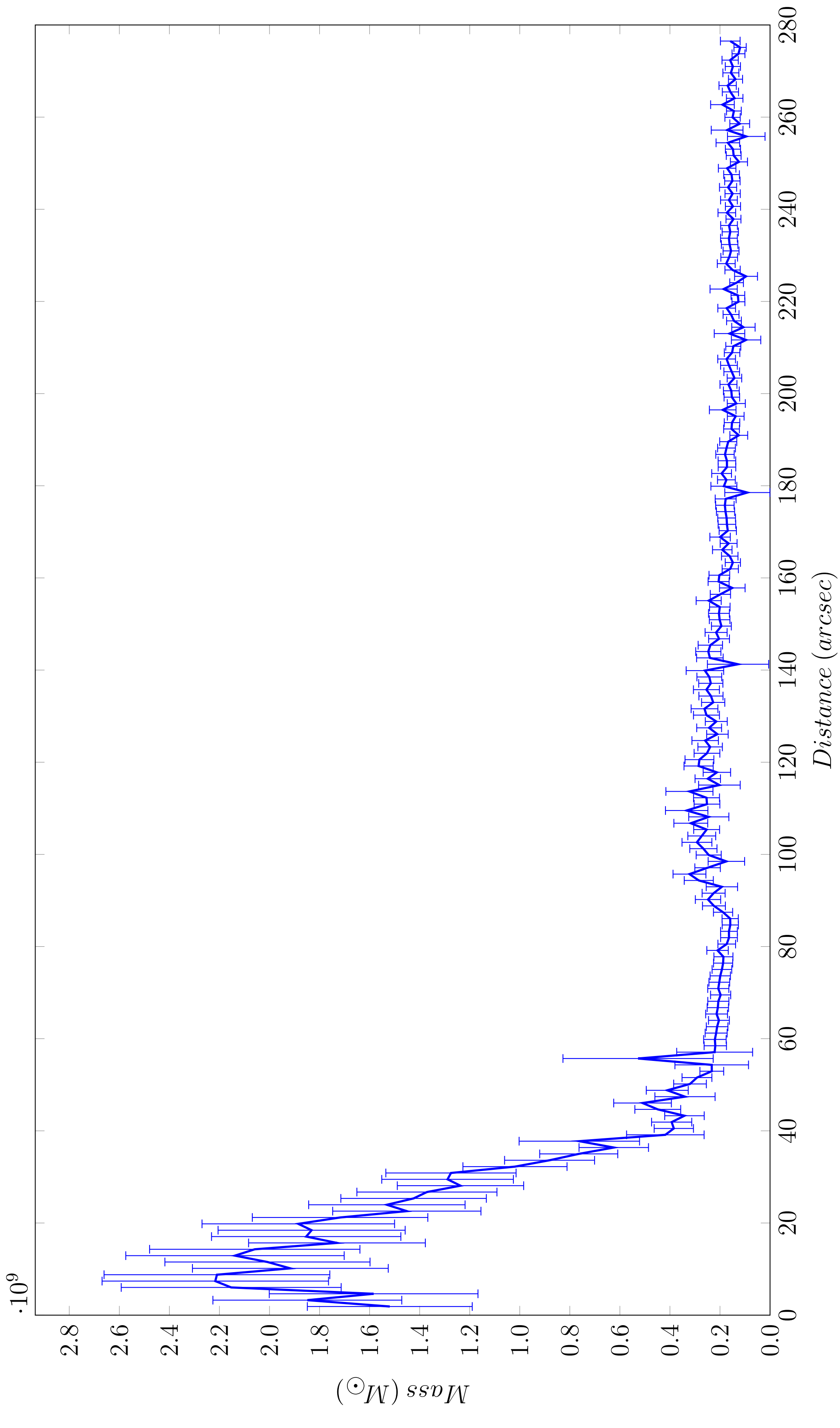

Figure 3.18: Total mass profile with error bars in galaxy NGC 7331

Chapter 4

Rotation curve

In this chapter, the rotation curve for NGC 7331 is calculated, based on the mass profile from the previous chapter. This rotation curve in then compared with the observed curve, determined with the 21-cm line of HI and the $H\alpha$ line in the visible spectrum, and available in the SPARC catalog [45].

4.1 Determination of the rotation curve from the mass profile

The mass of gas and stars was calculated in the previous chapter for each distance to the galactic center. From this mass profile, two different hypotheses were used at different locations for the calculation of the rotation curve: spherical mass distribution or in-plane circular mass distribution. The same methodology as Van de Vyvere [19] is followed in this Section.

In spiral galaxies, the galactic bulge is assumed to have a spherical or ellipsoidal mass distribution, and the surface mass density is commonly considered to follow a de Vaucouleurs' law [12]. The idea of surface mass density of a sphere might be a counter-intuitive concept, but in fact, it is the projection of a spherically distributed mass in a plane. Therefore, the surface mass density for a given distance to the galactic center R is the integral of the volumetric mass in a column at this distance and perpendicular to the galactic plane. This is illustrated in Figure 4.1. Plotting the logarithm of the surface mass density of the stars with distance (Figure 4.2), it is possible to adjust a straight line representing the decrease rate of the surface mass density in the bulge, separating then the spherical mass distribution assumed here from the distribution of mass in the galactic disk (the stellar mass of the bulge and disk can also be found separately in Figure 3.13). For the following calculations it is assumed that the galactic gas is also contained in the galactic disk.

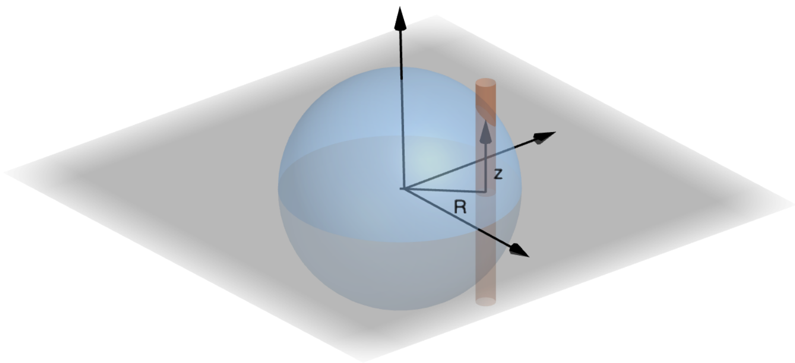

Figure 4.1: Scheme to illustrate the concept of surface mass density

Consequently, for the bulge of the galaxy, with spherical mass distribution:

$$V(R) = \sqrt{\frac{GM(R)}{R}} \tag{4.1}$$

with $V(R)$ the rotational velocity, G the gravitational constant and $M(R)$ the mass inside a sphere of radius R.

However, a different approach is followed for the galactic disk. Where the spherical symmetry is no longer applicable, the mass in the interior of the sphere of radius R (the radius of the orbit) cannot be reduced to a point mass at the galactic center, and the gravitational contribution of the mass outside this radius is not considered null

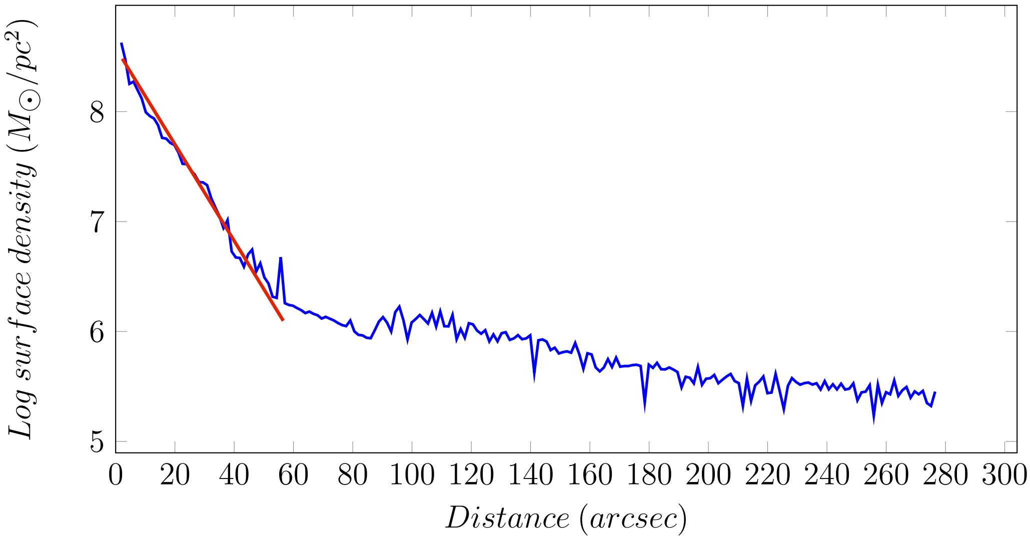

Figure 4.2: Logarithm of the stellar surface density

any longer. Since that simplification is not valid in the disk, a numerical algorithm was developed for calculating the acceleration due to the centripetal force resulting from the gravitational interaction with the rest of the disk at each distance. By calculating the centripetal force, the rotational velocities for each distance were obtained [19].

Finally, the resulting rotation curve is calculated by adding the acceleration due to the bulge and the acceleration due to the disk. The result is shown in Figure 4.3 and Table C.1.

4.2 Comparison with the observed rotation curve

The data of the rotational velocities in the SPARC catalog [45] is given for the distances in kpc, thus a distance conversion to *arcsec* is needed. This SPARC curve is shown in Figure 4.4. In Figure 4.5, both the observed rotation curve and the rotation curve obtained in the previous section are shown. The calculated curve is obtained for two hypotheses: a non-rotating bulge and a bulge rotating in the same direction as the disk. In fact, as stated in Chapter 1, NGC 7331 seems to have a

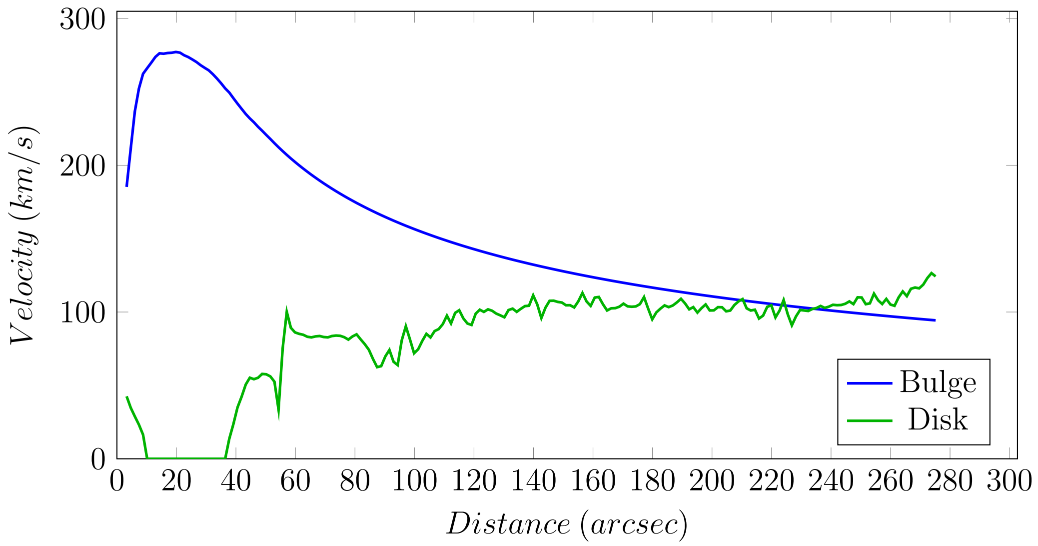

Figure 4.3: Contributions from the bulge and the disk to the rotation curve

counter-rotating bulge [18]. The result from both hypotheses is shown, demonstrating that the rotation of the bulge has no influence in the area where the SPARC data is available (the first data point from the SPARC catalog is at a distance of about $40 arcsec$), except for a couple of points in the transition bulge-disk.

Beyond this distance, there is a deficit of around $100 km/s$ in the calculated curve with respect to the observed curve. To explain this, several argumentations are possible. A few of them are set out in this section.

Underestimation of the distance

The consequences of a possible underestimation of the distance to NGC 7331 are not negligible. For a start, the geometrical dilution applied to the Maraston fluxes for a distance of $14.7 Mpc$ would be smaller than the real one. An underestimation in the geometrical dilution applied to these theoretical fluxes would result on an underestimation of the calculated stellar masses, and thus, on the obtention of rotation velocities below the real ones. The same effect would be present in the calculation of the mass of hydrogen, which is also affected by the factor of dilution.

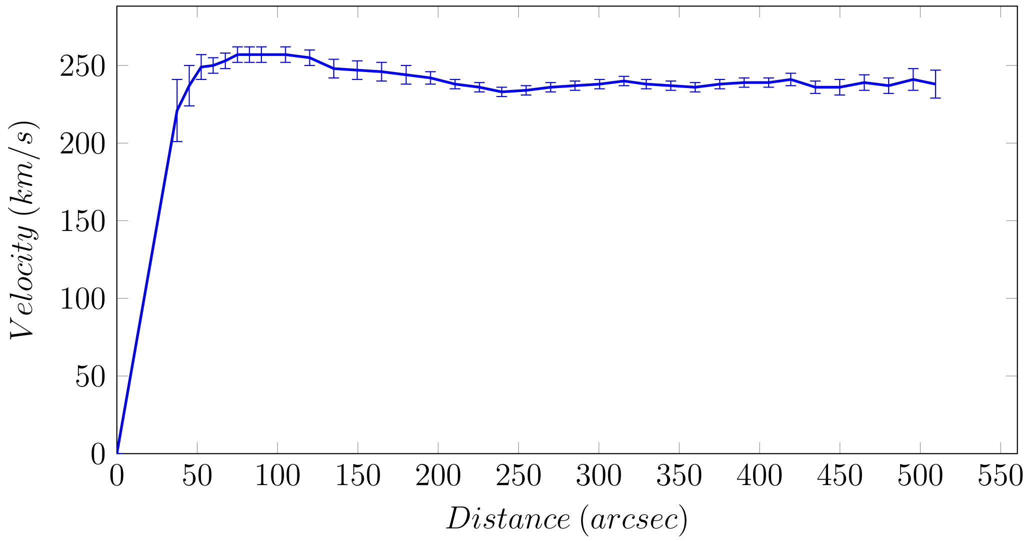

Figure 4.4: Rotation curve with error bars from the *SPARC* catalog

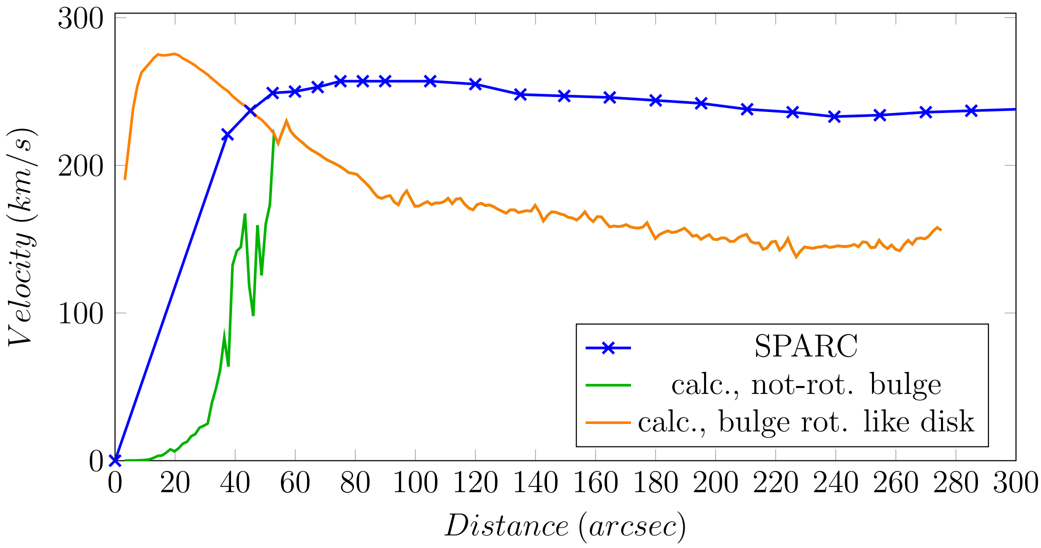

Figure 4.5: Rotation curves comparison

In addition to this, the underestimation of the distance to the galaxy also causes an underestimation of the distances within the galaxy. All of these effects contribute to an underestimation of the calculated rotation velocities.

Interstellar luminosity attenuation

If an interstellar luminosity attenuator (i.e. grey dust [27]) decreases the fluxes of the stars, including those of the cepheids used to calculate the distance [16], the distance to NGC 7331 would be overestimated. In this case, the estimations of mass would not be influenced, since the dilution factor applied to the stellar population models would be the same as the one obtained from the observation of the cepheids. However, the intragalactic distances in NGC 7331, calculated using the distance to the galaxy, would be overestimated, which leads to an underestimation of the velocity of rotation.

Underestimation of the absorption by dust

As discussed in Chapter 2, Section 2.4, very little is known about the morphology and the distribution of dust in the different galaxies, and NGC 7331 is no exception. There are several dust models proposed by Draine [27, 31] that could have been used. With the three of them, the calculated absorption is considerably high, specially in the ultraviolet wavelengths, which leads to think on a high abundance of dust in NGC 7331. The usual assumption is that the mass of dust is around 0.1% of the mass of gas [46], so it was considered negligible with respect to the stellar mass and the mass of gas. This might not be the case for NGC 7331. Furthermore, the coefficient of extinction for the NUV band was modified (in order to fit the spectrum with Maraston's stellar population models). This modification might result on an underestimation of the flux in this wavelength, leading to an underestimation of young stars, which are the dominant population in the disk. The global consequence of these effects is an underestimation of the rotation velocity in the disk.

Underestimation of the mass

In the process of adjusting the fluxes to the stellar population models, a Kroupa function [35] was selected as the initial mass function, but other possibilities were available. For instance, choosing a Salpeter function [34] would have lead to a higher proportion of low mass stars, resulting on an increase in the stellar mass. Another assumption made was using a constant value for the metallicity. Studies show that the metallicity in a galaxy changes not only with the age of the stars but also depending on the area in the galaxy (bulge/inner disk/outer disk) [47]. The influence in the mass profile of using this assumption should be studied more in depth.

Dark matter halo

The difference in the rotation curves could also indicate the presence of a great amount of mass which does not interact with observable electromagnetic radiation, this is, *dark matter*. In fact, rotation curves of spiral galaxies are considered the best observational proof of the existence of dark matter [7]. The necessity of dark matter was proposed more than 80 years ago (Zwicky, 1937 [6] or even Pointcaré, 1906 [5]). However, this theory is still not uniformly accepted: cold dark matter hierarchical models are the main way to explain rotation curves, but the problem of explaining its structure and formation remains [7]. As Navarro [48] remarks: "Our analysis has made use of this surprisingly tight relation between disk luminosity and rotation speed but provides no firm clues to elucidate its origin". Many actual galactic models assume the presence of this dark matter halo. There are several models for the dark matter halo structure. The most widely accepted is the so called "universal" or NFW (Navarro, Frenk and White [49]) halo:

$$\rho(r) = \frac{\rho_0}{\frac{r}{r_s}\left(1 + \frac{r}{r_s}\right)^2} \tag{4.2}$$

where ρ_0 and r_s are the scale factors for density and size respectively, which need to be adjusted. Following this model, the mass of dark matter inside an sphere of radius r is given by:

$$M(r) = m_0 \left(\ln \left(\frac{r_s + r}{r_s} \right) - \frac{r}{r_s + r} \right) \tag{4.3}$$

with $m_0 = 4\pi\rho_0 r_s^3$.

A halo with the parameters $m_0 = 4 \cdot 10^{11} M_{\odot}$ and $r_s = 10kpc(140arcsec)$ provides a good adjustment to the observed rotation curve. The cumulated mass on a sphere of radius r of this halo is shown in Figure 4.6. The obtained rotation curve for the three components (bulge, disk and NFW halo) is shown in Figure 4.7, and the result of adding these three components for a non-rotating bulge and a bulge rotating like the disk is shown in Figure 4.8 (and in Table C.2), together with the rotation curve from the SPARC catalog.

This NFW model of the dark matter halo implies a dark matter to luminous matter ratio of around 2.2 at a radius or 275 arcsec. As seen in Figure 4.8, this type of model provides a satisfactory fit to the observed rotation curve. The fitting of the rotation curve for a NFW halo, for MOND theory (see next Section) and two other schemes was also performed by Bottema and Pestaña [8] for 12 galaxies, being NGC 7331 one of them. However, NFW halos present some challenges like, for example, the obtention of the Tully-Fisher relation and the difficulty to match this theory with the data form the Milky Way (see Navarro and Steinmetz [50], and Battaner and Florido [7]).

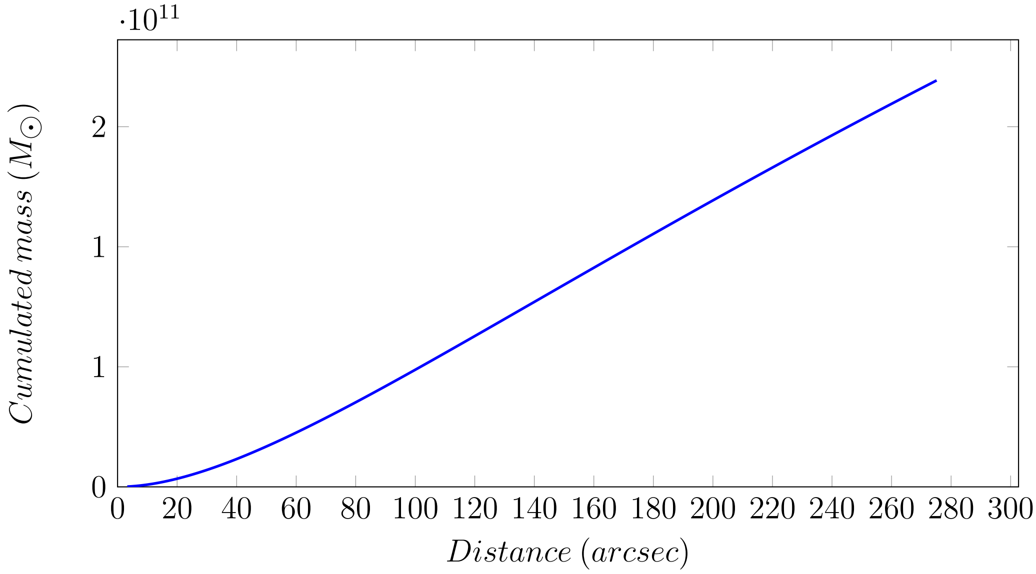

Figure 4.6: Mass profile of the NFW halo

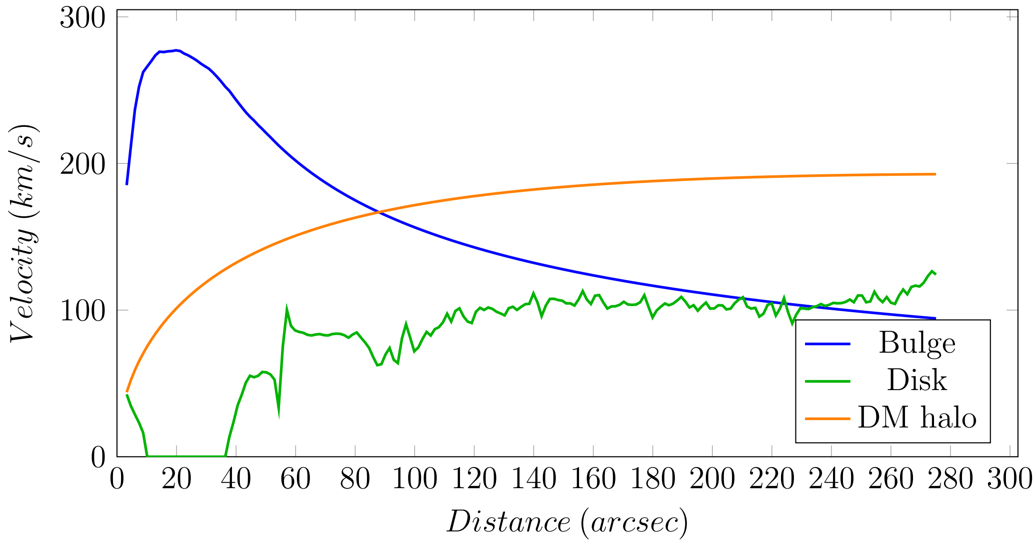

Figure 4.7: Contributions from the bulge, disk and DM halo to the rotation curve

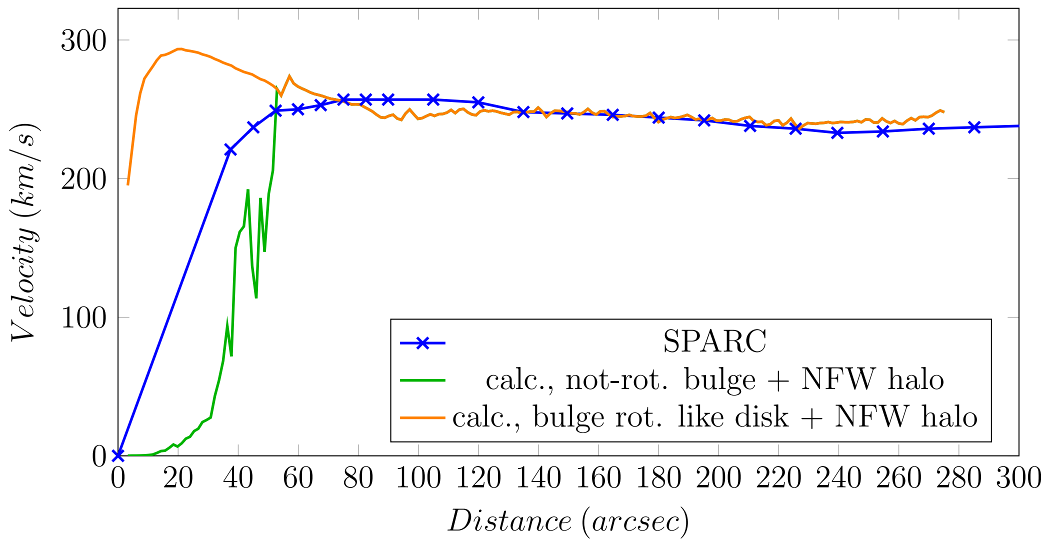

Figure 4.8: Rotation curves comparison with a NFW halo

Alternative theories

There are other theories that could explain this difference between the rotation curve calculated from the luminosity of the galaxy and the observed rotation curve. These other hypotheses were not developed in this dissertation, but an introduction of the concepts is provided.

The MOND theory (Milgrom, 1983 [9]) proposes a modification to Newtonian physics for small accelerations. The basis of this theory is that while Newton's laws have been widely tested in high-acceleration environments, they have not been verified in contexts where the acceleration is extremely low, like the stars in the outer parts of the galaxy [51]. The proposed modification is to assume the gravitational force in the outer parts of the galaxy to be proportional to the inverse of the radius ($\propto 1/r$), instead of being proportional to the inverse of the square radius ($\propto 1/r^2$), like in Newton's law. This modification solves the discrepancy between the two rotation curves, and it is nowadays the main alternative to the dark matter halo theory [7]. Nevertheless, Newtonian dynamics are an approximation that can be derived from General Relativity. A modification of Newtonian Dynamics would, therefore, contradict the theory of General Relativity, unless its deduction can be justified as an application of Einstein's theory in a similar way as Newtonian Dynamics, which has not been done up to date [52].

Another example of an alternative explanation, defended by Combes [3], and Pfenniger and Combes [11], is the possibility of the presence of undetected gas clouds. They have proposed that the evolution of spiral galaxies suggest a gradual transformation of dark matter into visible matter, i.e. into stars. Then, this dark matter should be identified as gas [11]. They suggest that these gas clouds are not detected because they are molecular gas clouds with a fractal structure, and such small clouds would be undetectable by available telescopes. This hypothesis would also explain the similarities in the distribution of gas and dark matter observed by Bosma [42] and Carignan *et al.* [53], since dark matter would in fact be undetected gas.

Finally, the problem of rotational curves in spiral galaxies might also be explained by the action of magnetic fields in the galactic disk. Binney [10] and Battaner *et al.* [54, 55] propose this hypothesis. Unlike gravitational fields, that decrease with the inverse of the squared radius, magnetic fields evolve locally due to gas motions [7]. Therefore, at big enough distances from the galactic center, this magnetic fields might become dominant. Even if this is not the case, observations suggest that ignoring the influence of magnetic fields in the rotation curves may be a completely unrealistic hypothesis. Magnetic fields in the outer parts of the galactic disk might be produced as a consequence of a highly turbulent magnetic diffusion, that merges the extragalactic and galactic magnetic fields. The outer disk would then acquire a magnetic energy gradient necessary to explain the gap in the rotation curves (see Battaner *et al.* [7, 54, 55])

Chapter 5

Conclusion

The objective of this master thesis was to obtain, as precisely as possible, the rotation curve of NGC 7331, based on the luminosity of the galaxy.

The luminosity profile was obtained in 14 wavelengths, from the far ultraviolet to the far infrared. In order to do this, some geometrical parameters were calculated, like the center of the galaxy, the orientation or the ellipticity, using the methods proposed by Biernaux *et al.* [21] and applied by Van de Vyvere [19].

Then, effect in the observed luminosity of the presence of interstellar dust was taken into account. To do this, the models of dust proposed by Draine [27, 31] were explored. The peak of the extinction coefficients at $220nm$ presented some problems for the later step, so a modification of the $R_V = 3.1$ model was used.

Once the corrected luminosity profiles are calculated, and using the data of 9 of the filters (from the FUV to the NIR) for each distance to the galactic center, an adjustment to the spectra of the stellar population models proposed by Maraston [29] is performed. To do this, a model of bursts of stellar formation is applied. The outcome of this is the presence of two stellar formation events (two bursts): an old one, occurred around 13Gyr ago, dominant in the bulge; and a much younger one, around 0.2Gyr ago, dominant in the galactic disk, providing a much *bluer* spectrum.

With the stellar population model, the mass profile of the stars is calculated for the different distances to the galactic center. The mass of neutral atomic hydrogen (HI) and molecular hydrogen (H_2) are calculated using the data obtained by Bosma [42] and Leroy *et al.* [43] respectively. The mass of helium (He) is calculated assuming cosmic abundances, with the mass fraction of primordial helium obtained by Izotov [44]. An improvement for future work would be to take into account the mass of ionized hydrogen and other molecules of gas present in the interstellar medium. For the mass of dust, the usual assumption of 0.1% of the mass of gas in the galaxy [46] was used, and thus this mass was neglected. However, the presence of dust in NGC 7331 might be more important than in other galaxies, so a more precise calculation of this mass of dust is advised for future work.

The rotation curve is then calculated from the galactic mass profile, considering two different situations for the bulge and the disk. The mass of gas is also assumed to be distributed in the disk. The bulge is assumed to have a spherical mass distribution, and the velocity component due to the bulge is easy to calculate. On the other hand, this assumption is not accurate for the disk, where the mass distribution is nearly flat and circular. An algorithm was developed to calculate the velocity, by making the centripetal acceleration equal to the acceleration in the radial direction resulting of the gravitational interaction with the rest of the galaxy.

It is important to note that the hypothesis of circular symmetry was used. By definition, due to the presence of spiral arms, spiral galaxies do not present this type of symmetry. The mass distribution in the disk would be affected by the presence of the arms and, therefore, the dynamics of the stars in the disk would differ from the estimation obtained with this assumption. A more in-depth study would be needed to evaluate the influence of this assumption.

The rotation curve obtained with this method is around 100km/s below the rotation curve obtained from spectroscopy [45], and does not present a decrease with distance. The obtained result behaves better than the usual curves obtained from the luminous disk having more general assumptions. Nevertheless, there is a big difference between the two rotation curves. A few possible causes for this gap, like an underestimation of the distance to the galaxy or the existence of a dark matter halo, were discussed in the previous chapter. Finally, some alternative theories were mentioned but not developed, like the MOND (*MOdified Newtonian Dynamics*) theory or the presence of strong magnetic fields in the outer disk. In order to draw conclusions and compare the adequacy of the different hypotheses, a study of a large number of spiral galaxies of different types would be needed.

Appendix A

Tables of luminosity

Result of the black body parameters and α coefficient for dust correction in NGC 7331

Ring index	Distance ($arcsec$)	Surface ($arcsec^2$)	A	T (K)	α
0	1.88	3.58	8.96E+11	46.36	1.05E+20
1	3.26	6.22	9.24E+11	45.75	1.47E+20
2	4.64	8.85	1.01E+12	44.14	2.36E+20
3	6.02	11.48	1.04E+12	43.64	2.19E+20
4	7.40	14.11	1.09E+12	42.64	2.50E+20
5	8.78	16.75	1.14E+12	41.56	2.80E+20
6	10.16	19.38	1.22E+12	40.15	3.13E+20
7	11.54	22.01	1.25E+12	39.58	3.17E+20
8	12.92	24.64	1.30E+12	38.77	3.30E+20
9	14.30	27.28	1.35E+12	38.09	3.49E+20
10	15.68	29.91	1.44E+12	36.95	3.72E+20
11	17.06	32.54	1.49E+12	36.60	3.92E+20
12	18.44	35.17	1.51E+12	36.45	3.99E+20
13	19.82	37.81	1.56E+12	36.12	4.25E+20
14	21.20	40.44	1.64E+12	35.61	4.63E+20
15	22.58	43.07	1.72E+12	35.30	5.10E+20
16	23.96	45.71	1.73E+12	35.71	5.23E+20
17	25.34	48.34	1.81E+12	35.61	5.68E+20
18	26.72	50.97	1.88E+12	35.61	6.11E+20
19	28.10	53.60	1.97E+12	35.62	6.83E+20
20	29.48	56.24	1.96E+12	36.13	6.96E+20
21	30.86	58.87	2.01E+12	36.37	7.38E+20
22	32.24	61.50	2.07E+12	36.57	7.83E+20
23	33.62	64.13	2.13E+12	36.74	8.38E+20
24	35.00	66.77	2.19E+12	36.92	8.93E+20

Ring index	Distance ($arcsec$)	Surface ($arcsec^2$)	A	T (K)	α
25	36.38	69.40	2.20E+12	37.13	9.22E+20
26	37.76	72.03	2.24E+12	37.35	9.93E+20
27	39.14	74.67	2.25E+12	37.59	1.05E+21
28	40.52	77.30	2.28E+12	37.79	1.15E+21
29	41.90	79.93	2.25E+12	37.84	1.12E+21
30	43.28	82.56	2.24E+12	37.83	1.14E+21
31	44.66	85.20	2.22E+12	37.80	1.17E+21
32	46.04	87.83	2.19E+12	37.77	1.21E+21
33	47.42	90.46	2.11E+12	37.77	1.16E+21
34	48.80	93.09	2.07E+12	37.71	1.18E+21
35	50.18	95.73	2.03E+12	37.54	1.19E+21
36	51.56	98.36	2.00E+12	37.45	1.21E+21
37	52.94	100.99	1.96E+12	37.41	1.20E+21
38	54.32	103.62	1.92E+12	37.39	1.21E+21
39	55.70	106.26	1.90E+12	37.31	1.24E+21
40	57.08	108.89	1.89E+12	37.16	1.27E+21
41	58.46	111.52	1.86E+12	37.21	1.30E+21
42	59.84	114.16	1.82E+12	37.32	1.30E+21
43	61.22	116.79	1.80E+12	37.17	1.31E+21
44	62.60	119.42	1.78E+12	37.13	1.34E+21
45	63.98	122.05	1.73E+12	37.02	1.36E+21
46	65.36	124.69	1.69E+12	37.36	1.33E+21
47	66.74	127.32	1.64E+12	37.28	1.33E+21
48	68.12	129.95	1.63E+12	37.09	1.33E+21
49	69.50	132.58	1.59E+12	36.65	1.34E+21
50	70.88	135.22	1.58E+12	36.75	1.29E+21
51	72.26	137.85	1.54E+12	36.53	1.28E+21
52	73.64	140.48	1.50E+12	36.30	1.26E+21
53	75.02	143.12	1.47E+12	35.99	1.25E+21
54	76.40	145.75	1.43E+12	35.86	1.24E+21
55	77.78	148.38	1.41E+12	35.75	1.22E+21
56	79.16	151.01	1.37E+12	35.58	1.22E+21
57	80.54	153.65	1.34E+12	35.31	1.21E+21
58	81.92	156.28	1.31E+12	35.02	1.20E+21
59	83.30	158.91	1.29E+12	34.95	1.18E+21
60	84.68	161.54	1.26E+12	34.67	1.16E+21
61	86.06	164.18	1.22E+12	34.44	1.14E+21
62	87.44	166.81	1.19E+12	34.07	1.13E+21
63	88.82	169.44	1.18E+12	34.10	1.11E+21
64	90.20	172.07	1.16E+12	33.83	1.10E+21

Ring index	Distance ($arcsec$)	Surface ($arcsec^2$)	A	T (K)	α
65	91.58	174.71	1.12E+12	33.61	1.09E+21
66	92.96	177.34	1.08E+12	33.36	1.08E+21
67	94.34	179.97	1.08E+12	33.20	1.07E+21
68	95.72	182.61	1.06E+12	33.04	1.06E+21
69	97.10	185.24	1.04E+12	32.87	1.05E+21
70	98.48	187.87	9.94E+11	32.61	1.03E+21
71	99.86	190.50	9.86E+11	32.46	1.03E+21
72	101.24	193.14	9.77E+11	32.34	1.02E+21
73	102.62	195.77	9.63E+11	32.22	1.01E+21
74	104.00	198.40	9.33E+11	32.06	1.00E+21
75	105.38	201.03	9.01E+11	31.92	9.93E+20
76	106.76	203.67	9.00E+11	31.91	9.92E+20
77	108.14	206.30	8.82E+11	31.83	9.86E+20
78	109.52	208.93	8.56E+11	31.78	9.76E+20
79	110.90	211.56	8.07E+11	31.72	9.67E+20
80	112.28	214.20	8.08E+11	31.82	9.60E+20
81	113.66	216.83	7.80E+11	31.78	9.48E+20
82	115.04	219.46	7.57E+11	31.71	9.27E+20
83	116.42	222.10	7.26E+11	31.68	9.07E+20
84	117.80	224.73	7.07E+11	31.67	8.98E+20
85	119.18	227.36	7.01E+11	31.69	8.89E+20
86	120.56	229.99	6.75E+11	31.66	8.75E+20
87	121.94	232.63	6.54E+11	31.66	8.65E+20
88	123.32	235.26	6.24E+11	31.76	8.56E+20
89	124.70	237.89	6.23E+11	31.82	8.45E+20
90	126.08	240.52	5.94E+11	31.92	8.28E+20
91	127.46	243.16	5.71E+11	31.92	8.16E+20
92	128.84	245.79	5.47E+11	32.02	8.11E+20
93	130.22	248.42	5.49E+11	31.88	7.97E+20
94	131.60	251.06	5.39E+11	31.94	7.94E+20
95	132.98	253.69	5.16E+11	31.88	7.84E+20
96	134.36	256.32	5.01E+11	31.88	7.83E+20
97	135.74	258.95	5.01E+11	31.79	7.77E+20
98	137.12	261.59	4.96E+11	31.68	7.67E+20
99	138.50	264.22	4.90E+11	31.54	7.64E+20
100	139.88	266.85	4.90E+11	31.24	7.60E+20
101	141.26	269.48	4.88E+11	31.10	7.56E+20
102	142.64	272.12	4.82E+11	31.16	7.48E+20
103	144.02	274.75	4.72E+11	31.10	7.46E+20
104	145.40	277.38	4.64E+11	31.02	7.45E+20

Ring index	Distance ($arcsec$)	Surface ($arcsec^2$)	A	T (K)	α
105	146.78	280.01	4.47E+11	30.96	7.51E+20
106	148.16	282.65	4.52E+11	30.97	7.35E+20
107	149.54	285.28	4.48E+11	30.74	7.28E+20
108	150.93	287.91	4.48E+11	30.59	7.28E+20
109	152.31	290.55	4.26E+11	30.49	7.34E+20
110	153.69	293.18	4.22E+11	30.71	7.21E+20
111	155.06	295.81	4.06E+11	30.77	7.21E+20
112	156.44	298.44	3.92E+11	30.77	7.25E+20
113	157.82	301.08	3.81E+11	30.70	7.30E+20
114	159.21	303.71	3.71E+11	30.72	7.31E+20
115	160.59	306.34	3.64E+11	30.79	7.28E+20
116	161.97	308.97	3.56E+11	30.66	7.28E+20
117	163.34	311.61	3.51E+11	30.48	7.30E+20
118	164.72	314.24	3.48E+11	30.22	7.25E+20
119	166.10	316.87	3.44E+11	30.31	7.24E+20
120	167.49	319.50	3.34E+11	30.28	7.23E+20
121	168.87	322.14	3.25E+11	30.11	7.19E+20
122	170.25	324.77	3.15E+11	29.96	7.11E+20
123	171.63	327.40	3.03E+11	30.28	7.14E+20
124	173.00	330.04	2.94E+11	30.28	7.08E+20
125	174.39	332.67	2.84E+11	30.26	7.01E+20
126	175.77	335.30	2.72E+11	30.14	6.89E+20
127	177.15	337.93	2.69E+11	30.19	6.87E+20
128	178.53	340.57	2.56E+11	30.38	6.81E+20
129	179.91	343.20	2.46E+11	30.38	6.74E+20
130	181.29	345.83	2.38E+11	30.25	6.66E+20
131	182.67	348.46	2.31E+11	30.18	6.56E+20
132	184.05	351.10	2.30E+11	30.18	6.54E+20
133	185.43	353.73	2.27E+11	30.08	6.48E+20
134	186.81	356.36	2.23E+11	29.86	6.38E+20
135	188.19	358.99	2.16E+11	29.71	6.29E+20
136	189.57	361.63	2.16E+11	29.94	6.33E+20
137	190.95	364.26	2.07E+11	30.03	6.30E+20
138	192.33	366.89	1.95E+11	30.10	6.16E+20
139	193.71	369.53	1.86E+11	30.04	6.09E+20
140	195.09	372.16	1.89E+11	30.15	6.17E+20
141	196.47	374.79	1.86E+11	30.18	6.22E+20
142	197.85	377.42	1.81E+11	30.11	6.16E+20
143	199.23	380.06	1.77E+11	30.04	6.15E+20
144	200.61	382.69	1.77E+11	29.90	6.14E+20

Ring index	Distance ($arcsec$)	Surface ($arcsec^2$)	A	T (K)	α
145	201.99	385.32	1.76E+11	30.14	6.15E+20
146	203.37	387.95	1.70E+11	30.27	6.10E+20
147	204.75	390.59	1.64E+11	30.36	6.08E+20
148	206.13	393.22	1.59E+11	30.39	6.04E+20
149	207.51	395.85	1.66E+11	30.21	6.00E+20
150	208.89	398.49	1.68E+11	30.05	5.94E+20
151	210.27	401.12	1.63E+11	30.10	5.91E+20
152	211.65	403.75	1.47E+11	30.54	5.81E+20
153	213.03	406.38	1.43E+11	30.96	5.85E+20
154	214.41	409.02	1.37E+11	31.13	5.78E+20
155	215.79	411.65	1.37E+11	31.04	5.69E+20
156	217.17	414.28	1.33E+11	30.88	5.65E+20
157	218.55	416.91	1.35E+11	30.79	5.60E+20
158	219.93	419.55	1.37E+11	30.67	5.59E+20
159	221.31	422.18	1.35E+11	30.69	5.59E+20
160	222.69	424.81	1.27E+11	30.98	5.56E+20
161	224.07	427.44	1.23E+11	31.07	5.52E+20
162	225.45	430.08	1.25E+11	31.17	5.53E+20
163	226.83	432.71	1.24E+11	31.09	5.51E+20
164	228.21	435.34	1.21E+11	31.22	5.52E+20
165	229.59	437.98	1.17E+11	31.19	5.49E+20
166	230.97	440.61	1.17E+11	31.45	5.49E+20
167	232.35	443.24	1.12E+11	31.65	5.46E+20
168	233.73	445.87	1.07E+11	31.91	5.46E+20
169	235.11	448.51	1.05E+11	31.77	5.47E+20
170	236.49	451.14	1.09E+11	31.72	5.45E+20
171	237.87	453.77	1.10E+11	31.48	5.43E+20
172	239.25	456.40	1.09E+11	31.50	5.36E+20
173	240.63	459.04	1.09E+11	31.34	5.33E+20
174	242.01	461.67	1.09E+11	31.25	5.32E+20
175	243.39	464.30	1.09E+11	31.36	5.36E+20
176	244.77	466.93	1.07E+11	31.33	5.35E+20
177	246.15	469.57	1.07E+11	31.20	5.35E+20
178	247.53	472.20	1.06E+11	31.00	5.27E+20
179	248.91	474.83	1.07E+11	31.03	5.27E+20
180	250.29	477.47	1.06E+11	30.95	5.24E+20
181	251.67	480.10	1.09E+11	30.61	5.23E+20
182	253.05	482.73	1.10E+11	30.27	5.23E+20
183	254.43	485.36	1.08E+11	30.54	5.19E+20
184	255.81	488.00	1.06E+11	30.53	5.15E+20

Ring index	Distance ($arcsec$)	Surface ($arcsec^2$)	A	T (K)	α
185	257.19	490.63	1.05E+11	30.50	5.13E+20
186	258.57	493.26	1.03E+11	30.46	5.11E+20
187	259.95	495.89	9.93E+10	30.69	5.06E+20
188	261.33	498.53	9.71E+10	30.86	5.05E+20
189	262.71	501.16	9.47E+10	31.01	5.03E+20
190	264.09	503.79	9.16E+10	31.04	4.98E+20
191	265.47	506.43	8.86E+10	31.17	4.96E+20
192	266.85	509.06	8.43E+10	31.60	4.90E+20
193	268.23	511.69	8.14E+10	31.77	4.88E+20
194	269.61	514.32	7.97E+10	31.85	4.87E+20
195	270.99	516.96	7.81E+10	31.80	4.85E+20
196	272.37	519.59	7.42E+10	32.22	4.78E+20
197	273.75	522.22	7.12E+10	32.44	4.75E+20
198	275.13	524.85	6.95E+10	32.53	4.75E+20
199	276.51	527.49	6.80E+10	32.45	4.80E+20

Table A.1: Result of the black body parameters and α coefficient for dust correction in NGC 7331

Result of the fluxes after dust correction, filters from GALEX FUV to SDSS r

Ring index	Distance (arcsec)	$\nu F_\nu/surface\ (Hz\ Jy/arcsec^2)$				
		FUV	NUV	u	g	r
0	1.88	1.019E+09	4.602E+09	1.420E+11	6.764E+11	1.181E+12
1	3.26	1.167E+09	4.901E+09	1.134E+11	4.925E+11	8.212E+11
2	4.64	1.413E+09	5.535E+09	7.738E+10	3.091E+11	4.925E+11
3	6.02	1.147E+09	4.950E+09	7.991E+10	3.219E+11	5.164E+11
4	7.40	1.131E+09	4.927E+09	6.990E+10	2.734E+11	4.332E+11
5	8.78	1.213E+09	4.874E+09	6.171E+10	2.351E+11	3.680E+11
6	10.16	1.304E+09	4.780E+09	5.293E+10	2.009E+11	3.098E+11
7	11.54	1.282E+09	4.846E+09	5.178E+10	1.936E+11	2.949E+11
8	12.92	1.332E+09	4.940E+09	4.898E+10	1.801E+11	2.693E+11
9	14.30	1.409E+09	5.153E+09	4.684E+10	1.681E+11	2.472E+11
10	15.68	1.516E+09	5.212E+09	4.349E+10	1.513E+11	2.186E+11
11	17.06	1.683E+09	5.475E+09	4.193E+10	1.448E+11	2.067E+11
12	18.44	1.888E+09	5.702E+09	4.225E+10	1.424E+11	2.010E+11
13	19.82	2.086E+09	6.164E+09	4.110E+10	1.353E+11	1.885E+11
14	21.20	2.601E+09	6.661E+09	3.987E+10	1.256E+11	1.714E+11
15	22.58	2.997E+09	7.342E+09	3.892E+10	1.187E+11	1.591E+11

Ring index	Distance (arcsec)	$\nu F_\nu / surface\ (Hz\ Jy/arcsec^2)$				
		FUV	NUV	u	g	r
16	23.96	3.305E+09	8.057E+09	4.131E+10	1.229E+11	1.638E+11
17	25.34	3.866E+09	8.956E+09	4.216E+10	1.196E+11	1.564E+11
18	26.72	4.659E+09	1.022E+10	4.287E+10	1.185E+11	1.517E+11
19	28.10	5.616E+09	1.198E+10	4.396E+10	1.161E+11	1.437E+11
20	29.48	6.271E+09	1.323E+10	4.700E+10	1.205E+11	1.480E+11
21	30.86	7.633E+09	1.482E+10	5.058E+10	1.225E+11	1.468E+11
22	32.24	8.980E+09	1.633E+10	5.438E+10	1.249E+11	1.456E+11
23	33.62	9.942E+09	1.803E+10	5.781E+10	1.262E+11	1.434E+11
24	35.00	1.119E+10	1.971E+10	6.163E+10	1.284E+11	1.423E+11
25	36.38	1.271E+10	2.144E+10	6.197E+10	1.289E+11	1.412E+11
26	37.76	1.517E+10	2.426E+10	6.334E+10	1.291E+11	1.373E+11
27	39.14	1.744E+10	2.693E+10	6.659E+10	1.284E+11	1.327E+11
28	40.52	1.980E+10	3.104E+10	6.867E+10	1.264E+11	1.265E+11
29	41.90	1.992E+10	3.027E+10	6.857E+10	1.265E+11	1.276E+11
30	43.28	2.130E+10	3.089E+10	6.928E+10	1.242E+11	1.244E+11
31	44.66	2.200E+10	3.124E+10	6.999E+10	1.213E+11	1.197E+11
32	46.04	2.223E+10	3.195E+10	6.683E+10	1.175E+11	1.145E+11
33	47.42	2.154E+10	3.030E+10	6.539E+10	1.150E+11	1.133E+11
34	48.80	2.139E+10	3.046E+10	6.333E+10	1.115E+11	1.088E+11
35	50.18	2.108E+10	3.002E+10	5.970E+10	1.065E+11	1.034E+11
36	51.56	2.132E+10	2.984E+10	5.853E+10	1.027E+11	9.986E+10
37	52.94	2.024E+10	2.856E+10	5.859E+10	1.003E+11	9.752E+10
38	54.32	2.024E+10	2.810E+10	5.675E+10	9.807E+10	9.495E+10
39	55.70	2.102E+10	2.789E+10	5.554E+10	9.528E+10	9.137E+10
40	57.08	2.247E+10	2.778E+10	5.397E+10	9.139E+10	8.709E+10
41	58.46	2.292E+10	2.808E+10	5.361E+10	8.932E+10	8.410E+10
42	59.84	2.342E+10	2.814E+10	5.338E+10	8.904E+10	8.347E+10
43	61.22	2.336E+10	2.774E+10	5.221E+10	8.557E+10	7.967E+10
44	62.60	2.390E+10	2.764E+10	5.127E+10	8.357E+10	7.670E+10
45	63.98	2.297E+10	2.678E+10	5.046E+10	7.945E+10	7.244E+10
46	65.36	2.415E+10	2.687E+10	5.159E+10	8.153E+10	7.457E+10
47	66.74	2.439E+10	2.632E+10	4.911E+10	7.849E+10	7.137E+10
48	68.12	2.388E+10	2.537E+10	4.779E+10	7.611E+10	6.916E+10
49	69.50	2.192E+10	2.321E+10	4.417E+10	7.158E+10	6.490E+10
50	70.88	2.130E+10	2.273E+10	4.481E+10	7.259E+10	6.668E+10
51	72.26	2.015E+10	2.151E+10	4.291E+10	6.940E+10	6.402E+10
52	73.64	1.843E+10	2.021E+10	4.064E+10	6.651E+10	6.158E+10
53	75.02	1.817E+10	1.915E+10	3.851E+10	6.277E+10	5.858E+10
54	76.40	1.799E+10	1.866E+10	3.684E+10	5.977E+10	5.633E+10
55	77.78	1.875E+10	1.845E+10	3.575E+10	5.867E+10	5.524E+10

Ring index	Distance (arcsec)	$\nu F_\nu/surface\ (Hz\ Jy/arcsec^2)$				
		FUV	NUV	u	g	r
56	79.16	1.882E+10	1.787E+10	3.394E+10	5.578E+10	5.227E+10
57	80.54	1.822E+10	1.717E+10	3.191E+10	5.269E+10	4.931E+10
58	81.92	1.777E+10	1.645E+10	3.035E+10	4.934E+10	4.649E+10
59	83.30	1.813E+10	1.613E+10	3.017E+10	4.864E+10	4.601E+10
60	84.68	1.737E+10	1.532E+10	2.840E+10	4.619E+10	4.398E+10
61	86.06	1.634E+10	1.432E+10	2.727E+10	4.387E+10	4.188E+10
62	87.44	1.603E+10	1.371E+10	2.478E+10	4.072E+10	3.915E+10
63	88.82	1.569E+10	1.335E+10	2.460E+10	4.097E+10	3.940E+10
64	90.20	1.555E+10	1.284E+10	2.308E+10	3.878E+10	3.740E+10
65	91.58	1.518E+10	1.243E+10	2.165E+10	3.643E+10	3.521E+10
66	92.96	1.438E+10	1.180E+10	2.050E+10	3.414E+10	3.308E+10
67	94.34	1.395E+10	1.146E+10	1.969E+10	3.358E+10	3.259E+10
68	95.72	1.328E+10	1.096E+10	1.901E+10	3.255E+10	3.167E+10
69	97.10	1.304E+10	1.049E+10	1.835E+10	3.121E+10	3.045E+10
70	98.48	1.237E+10	9.841E+09	1.712E+10	2.915E+10	2.827E+10
71	99.86	1.208E+10	9.688E+09	1.645E+10	2.838E+10	2.760E+10
72	101.24	1.118E+10	9.152E+09	1.624E+10	2.800E+10	2.723E+10
73	102.62	1.088E+10	9.047E+09	1.539E+10	2.716E+10	2.655E+10
74	104.00	1.052E+10	8.716E+09	1.452E+10	2.584E+10	2.530E+10
75	105.38	1.029E+10	8.419E+09	1.406E+10	2.438E+10	2.400E+10
76	106.76	9.731E+09	8.239E+09	1.375E+10	2.454E+10	2.417E+10
77	108.14	9.699E+09	8.155E+09	1.345E+10	2.370E+10	2.332E+10
78	109.52	9.719E+09	8.057E+09	1.296E+10	2.277E+10	2.254E+10
79	110.90	9.729E+09	7.915E+09	1.228E+10	2.105E+10	2.084E+10
80	112.28	9.545E+09	7.869E+09	1.245E+10	2.158E+10	2.142E+10
81	113.66	9.424E+09	7.626E+09	1.225E+10	2.072E+10	2.055E+10
82	115.04	9.492E+09	7.363E+09	1.224E+10	2.005E+10	1.984E+10
83	116.42	9.474E+09	7.200E+09	1.184E+10	1.929E+10	1.905E+10
84	117.80	9.111E+09	7.147E+09	1.133E+10	1.885E+10	1.869E+10
85	119.18	9.099E+09	7.108E+09	1.134E+10	1.877E+10	1.871E+10
86	120.56	8.819E+09	6.932E+09	1.109E+10	1.810E+10	1.800E+10
87	121.94	8.820E+09	6.842E+09	1.074E+10	1.762E+10	1.738E+10
88	123.32	8.652E+09	6.778E+09	1.047E+10	1.705E+10	1.664E+10
89	124.70	8.559E+09	6.799E+09	1.063E+10	1.730E+10	1.706E+10
90	126.08	8.421E+09	6.622E+09	1.048E+10	1.685E+10	1.657E+10
91	127.46	8.271E+09	6.445E+09	1.020E+10	1.625E+10	1.597E+10
92	128.84	8.391E+09	6.454E+09	1.004E+10	1.567E+10	1.542E+10
93	130.22	7.923E+09	6.180E+09	1.007E+10	1.568E+10	1.558E+10
94	131.60	7.887E+09	6.161E+09	9.793E+09	1.558E+10	1.549E+10
95	132.98	7.464E+09	5.893E+09	9.436E+09	1.485E+10	1.480E+10

Ring index	Distance (arcsec)	$\nu F_\nu / surface\ (Hz\ Jy/arcsec^2)$				
		FUV	NUV	u	g	r
96	134.36	7.413E+09	5.832E+09	9.093E+09	1.431E+10	1.435E+10
97	135.74	7.325E+09	5.795E+09	8.886E+09	1.422E+10	1.428E+10
98	137.12	7.063E+09	5.611E+09	8.597E+09	1.409E+10	1.420E+10
99	138.50	7.034E+09	5.436E+09	8.358E+09	1.366E+10	1.379E+10
100	139.88	6.806E+09	5.309E+09	7.997E+09	1.320E+10	1.318E+10
101	141.26	6.622E+09	5.217E+09	7.841E+09	1.308E+10	1.264E+10
102	142.64	6.574E+09	5.141E+09	7.871E+09	1.305E+10	1.298E+10
103	144.02	6.481E+09	5.044E+09	7.531E+09	1.268E+10	1.275E+10
104	145.40	6.374E+09	4.923E+09	7.383E+09	1.237E+10	1.238E+10
105	146.78	6.417E+09	4.893E+09	7.031E+09	1.156E+10	1.133E+10
106	148.16	6.132E+09	4.776E+09	7.275E+09	1.208E+10	1.202E+10
107	149.54	5.939E+09	4.580E+09	7.173E+09	1.158E+10	1.148E+10
108	150.93	5.838E+09	4.488E+09	6.961E+09	1.136E+10	1.121E+10
109	152.31	5.833E+09	4.367E+09	6.579E+09	1.041E+10	1.020E+10
110	153.69	5.724E+09	4.352E+09	6.942E+09	1.083E+10	1.068E+10
111	155.06	5.585E+09	4.260E+09	6.608E+09	1.048E+10	1.032E+10
112	156.44	5.461E+09	4.155E+09	6.153E+09	1.011E+10	9.939E+09
113	157.82	5.240E+09	3.977E+09	5.947E+09	9.669E+09	9.492E+09
114	159.21	5.135E+09	3.874E+09	5.821E+09	9.448E+09	9.258E+09
115	160.59	4.997E+09	3.750E+09	5.657E+09	9.498E+09	9.376E+09
116	161.97	4.780E+09	3.588E+09	5.311E+09	9.148E+09	9.045E+09
117	163.34	4.556E+09	3.414E+09	5.181E+09	8.815E+09	8.693E+09
118	164.72	4.331E+09	3.264E+09	5.116E+09	8.432E+09	8.243E+09
119	166.10	4.138E+09	3.182E+09	5.171E+09	8.492E+09	8.389E+09
120	167.49	3.945E+09	3.070E+09	4.892E+09	8.262E+09	8.167E+09
121	168.87	3.717E+09	2.905E+09	4.661E+09	7.884E+09	7.834E+09
122	170.25	3.495E+09	2.761E+09	4.561E+09	7.486E+09	7.470E+09
123	171.63	3.409E+09	2.735E+09	4.458E+09	7.578E+09	7.657E+09
124	173.00	3.228E+09	2.610E+09	4.283E+09	7.461E+09	7.493E+09
125	174.39	3.089E+09	2.503E+09	4.123E+09	7.244E+09	7.306E+09
126	175.77	2.919E+09	2.359E+09	3.854E+09	6.938E+09	6.992E+09
127	177.15	2.822E+09	2.300E+09	3.877E+09	6.955E+09	7.050E+09
128	178.53	2.735E+09	2.227E+09	3.885E+09	6.811E+09	6.961E+09
129	179.91	2.624E+09	2.142E+09	3.718E+09	6.599E+09	6.780E+09
130	181.29	2.478E+09	2.054E+09	3.476E+09	6.324E+09	6.522E+09
131	182.67	2.351E+09	1.960E+09	3.430E+09	6.129E+09	6.355E+09
132	184.05	2.306E+09	1.942E+09	3.333E+09	6.143E+09	6.376E+09
133	185.43	2.291E+09	1.887E+09	3.314E+09	6.014E+09	6.210E+09
134	186.81	2.258E+09	1.831E+09	3.109E+09	5.805E+09	6.004E+09
135	188.19	2.138E+09	1.759E+09	2.994E+09	5.503E+09	5.703E+09

Ring index	Distance (arcsec)	$\nu F_\nu/surface\ (Hz\ Jy/arcsec^2)$				
		FUV	NUV	u	g	r
136	189.57	2.076E+09	1.767E+09	3.141E+09	5.688E+09	5.922E+09
137	190.95	1.997E+09	1.721E+09	2.939E+09	5.560E+09	5.831E+09
138	192.33	1.938E+09	1.632E+09	3.024E+09	5.363E+09	5.600E+09
139	193.71	1.853E+09	1.567E+09	2.935E+09	5.092E+09	5.300E+09
140	195.09	1.845E+09	1.590E+09	2.931E+09	5.231E+09	5.460E+09
141	196.47	1.825E+09	1.572E+09	2.834E+09	5.157E+09	5.394E+09
142	197.85	1.721E+09	1.515E+09	2.753E+09	4.952E+09	5.200E+09
143	199.23	1.648E+09	1.482E+09	2.657E+09	4.823E+09	5.068E+09
144	200.61	1.602E+09	1.448E+09	2.584E+09	4.741E+09	4.956E+09
145	201.99	1.667E+09	1.489E+09	2.713E+09	4.873E+09	5.061E+09
146	203.37	1.653E+09	1.480E+09	2.708E+09	4.802E+09	4.959E+09
147	204.75	1.686E+09	1.458E+09	2.593E+09	4.702E+09	4.887E+09
148	206.13	1.700E+09	1.462E+09	2.541E+09	4.535E+09	4.740E+09
149	207.51	1.774E+09	1.495E+09	2.615E+09	4.651E+09	4.842E+09
150	208.89	1.823E+09	1.512E+09	2.699E+09	4.583E+09	4.745E+09
151	210.27	1.848E+09	1.501E+09	2.672E+09	4.434E+09	4.610E+09
152	211.65	1.873E+09	1.474E+09	2.754E+09	4.225E+09	4.424E+09
153	213.03	1.929E+09	1.520E+09	2.576E+09	4.429E+09	4.622E+09
154	214.41	1.922E+09	1.504E+09	2.553E+09	4.351E+09	4.622E+09
155	215.79	1.901E+09	1.497E+09	2.642E+09	4.269E+09	4.549E+09
156	217.17	1.855E+09	1.475E+09	2.420E+09	4.116E+09	4.341E+09
157	218.55	1.847E+09	1.465E+09	2.401E+09	4.162E+09	4.346E+09
158	219.93	1.865E+09	1.470E+09	2.349E+09	4.142E+09	4.351E+09
159	221.31	1.921E+09	1.469E+09	2.272E+09	4.123E+09	4.325E+09
160	222.69	1.954E+09	1.439E+09	2.372E+09	3.990E+09	4.183E+09
161	224.07	1.963E+09	1.455E+09	2.290E+09	3.914E+09	4.087E+09
162	225.45	2.014E+09	1.516E+09	2.263E+09	4.054E+09	4.186E+09
163	226.83	2.037E+09	1.532E+09	2.280E+09	3.927E+09	4.064E+09
164	228.21	2.073E+09	1.565E+09	2.104E+09	3.886E+09	4.025E+09
165	229.59	2.071E+09	1.561E+09	2.011E+09	3.717E+09	3.839E+09
166	230.97	2.107E+09	1.559E+09	2.140E+09	3.893E+09	4.010E+09
167	232.35	2.089E+09	1.548E+09	2.216E+09	3.834E+09	3.920E+09
168	233.73	2.062E+09	1.526E+09	2.196E+09	3.785E+09	3.874E+09
169	235.11	2.038E+09	1.504E+09	2.150E+09	3.616E+09	3.654E+09
170	236.49	2.009E+09	1.485E+09	2.242E+09	3.769E+09	3.863E+09
171	237.87	1.972E+09	1.458E+09	2.107E+09	3.741E+09	3.872E+09
172	239.25	1.936E+09	1.428E+09	2.120E+09	3.778E+09	3.877E+09
173	240.63	1.878E+09	1.381E+09	2.161E+09	3.697E+09	3.784E+09
174	242.01	1.842E+09	1.348E+09	2.122E+09	3.668E+09	3.736E+09
175	243.39	1.746E+09	1.312E+09	2.105E+09	3.756E+09	3.877E+09

Ring index	Distance (arcsec)	$\nu F_\nu/surface\,(Hz\,Jy/arcsec^2)$				
		FUV	NUV	u	g	r
176	244.77	1.651E+09	1.266E+09	2.052E+09	3.730E+09	3.824E+09
177	246.15	1.619E+09	1.236E+09	2.056E+09	3.658E+09	3.772E+09
178	247.53	1.549E+09	1.188E+09	2.078E+09	3.544E+09	3.632E+09
179	248.91	1.507E+09	1.145E+09	2.121E+09	3.632E+09	3.757E+09
180	250.29	1.451E+09	1.108E+09	2.055E+09	3.588E+09	3.734E+09
181	251.67	1.424E+09	1.106E+09	1.960E+09	3.568E+09	3.693E+09
182	253.05	1.401E+09	1.095E+09	1.836E+09	3.428E+09	3.528E+09
183	254.43	1.359E+09	1.062E+09	1.891E+09	3.545E+09	3.724E+09
184	255.81	1.314E+09	1.032E+09	1.930E+09	3.496E+09	3.680E+09
185	257.19	1.313E+09	1.023E+09	1.854E+09	3.448E+09	3.604E+09
186	258.57	1.344E+09	1.014E+09	1.912E+09	3.346E+09	3.488E+09
187	259.95	1.318E+09	1.002E+09	1.871E+09	3.375E+09	3.497E+09
188	261.33	1.302E+09	9.974E+08	1.820E+09	3.384E+09	3.528E+09
189	262.71	1.287E+09	1.001E+09	1.872E+09	3.368E+09	3.512E+09
190	264.09	1.268E+09	9.975E+08	1.855E+09	3.272E+09	3.387E+09
191	265.47	1.291E+09	9.971E+08	1.823E+09	3.225E+09	3.318E+09
192	266.85	1.239E+09	9.696E+08	1.868E+09	3.319E+09	3.456E+09
193	268.23	1.238E+09	9.643E+08	1.810E+09	3.304E+09	3.421E+09
194	269.61	1.242E+09	9.631E+08	1.787E+09	3.268E+09	3.394E+09
195	270.99	1.260E+09	9.694E+08	1.776E+09	3.164E+09	3.263E+09
196	272.37	1.211E+09	9.371E+08	1.777E+09	3.217E+09	3.405E+09
197	273.75	1.209E+09	9.218E+08	1.781E+09	3.172E+09	3.381E+09
198	275.13	1.234E+09	9.212E+08	1.714E+09	3.130E+09	3.362E+09
199	276.51	1.302E+09	9.343E+08	1.648E+09	2.972E+09	3.184E+09

Table A.2: Result of the fluxes after dust correction, filters from GALEX FUV to SDSS r

Result of the fluxes after dust correction, filters from SDSS i to Spitzer IRAC8.0

Ring index	Distance (arcsec)	$\nu F_\nu/surface\,(Hz\,Jy/arcsec^2)$				
		i	z	IRAC3.6	IRAC4.5	IRAC8.0
0	1.88	1.428E+12	1.588E+12	2.615E+11	1.122E+11	3.824E+10
1	3.26	9.914E+11	1.115E+12	2.018E+11	8.492E+10	3.255E+10
2	4.64	5.938E+11	6.666E+11	1.268E+11	5.477E+10	2.504E+10
3	6.02	6.232E+11	7.005E+11	1.296E+11	5.661E+10	2.475E+10
4	7.40	5.212E+11	5.831E+11	1.087E+11	4.856E+10	2.184E+10
5	8.78	4.412E+11	4.847E+11	9.023E+10	4.040E+10	1.921E+10

Ring index	Distance (arcsec)	$\nu F_\nu / surface\,(Hz\,Jy/arcsec^2)$				
		i	z	IRAC3.6	IRAC4.5	IRAC8.0
6	10.16	3.668E+11	3.958E+11	7.144E+10	3.198E+10	1.637E+10
7	11.54	3.467E+11	3.709E+11	6.629E+10	2.978E+10	1.543E+10
8	12.92	3.142E+11	3.349E+11	5.940E+10	2.674E+10	1.421E+10
9	14.30	2.859E+11	3.036E+11	5.289E+10	2.389E+10	1.319E+10
10	15.68	2.493E+11	2.619E+11	4.484E+10	2.031E+10	1.185E+10
11	17.06	2.343E+11	2.444E+11	4.118E+10	1.870E+10	1.145E+10
12	18.44	2.267E+11	2.351E+11	3.947E+10	1.793E+10	1.131E+10
13	19.82	2.115E+11	2.183E+11	3.639E+10	1.653E+10	1.111E+10
14	21.20	1.913E+11	1.959E+11	3.226E+10	1.475E+10	1.080E+10
15	22.58	1.757E+11	1.783E+11	2.897E+10	1.332E+10	1.071E+10
16	23.96	1.803E+11	1.840E+11	2.985E+10	1.374E+10	1.135E+10
17	25.34	1.704E+11	1.727E+11	2.762E+10	1.275E+10	1.162E+10
18	26.72	1.635E+11	1.648E+11	2.609E+10	1.203E+10	1.217E+10
19	28.10	1.523E+11	1.519E+11	2.354E+10	1.085E+10	1.293E+10
20	29.48	1.569E+11	1.568E+11	2.472E+10	1.142E+10	1.405E+10
21	30.86	1.532E+11	1.514E+11	2.375E+10	1.100E+10	1.516E+10
22	32.24	1.494E+11	1.460E+11	2.281E+10	1.064E+10	1.660E+10
23	33.62	1.446E+11	1.391E+11	2.178E+10	1.025E+10	1.796E+10
24	35.00	1.420E+11	1.357E+11	2.124E+10	1.002E+10	1.923E+10
25	36.38	1.411E+11	1.345E+11	2.130E+10	1.008E+10	2.029E+10
26	37.76	1.357E+11	1.288E+11	2.048E+10	9.748E+09	2.197E+10
27	39.14	1.298E+11	1.226E+11	1.991E+10	9.555E+09	2.387E+10
28	40.52	1.216E+11	1.142E+11	1.898E+10	9.193E+09	2.577E+10
29	41.90	1.237E+11	1.165E+11	1.923E+10	9.315E+09	2.571E+10
30	43.28	1.196E+11	1.114E+11	1.862E+10	9.034E+09	2.596E+10
31	44.66	1.139E+11	1.053E+11	1.768E+10	8.570E+09	2.587E+10
32	46.04	1.077E+11	9.877E+10	1.668E+10	8.096E+09	2.584E+10
33	47.42	1.074E+11	9.843E+10	1.677E+10	8.156E+09	2.549E+10
34	48.80	1.030E+11	9.427E+10	1.617E+10	7.891E+09	2.531E+10
35	50.18	9.761E+10	8.897E+10	1.524E+10	7.451E+09	2.448E+10
36	51.56	9.398E+10	8.537E+10	1.456E+10	7.118E+09	2.406E+10
37	52.94	9.176E+10	8.327E+10	1.423E+10	6.951E+09	2.355E+10
38	54.32	8.936E+10	8.150E+10	1.389E+10	6.802E+09	2.314E+10
39	55.70	8.572E+10	7.829E+10	1.330E+10	6.517E+09	2.284E+10
40	57.08	8.109E+10	7.363E+10	1.257E+10	6.162E+09	2.257E+10
41	58.46	7.780E+10	7.026E+10	1.213E+10	5.961E+09	2.251E+10
42	59.84	7.711E+10	6.920E+10	1.210E+10	5.951E+09	2.228E+10
43	61.22	7.339E+10	6.564E+10	1.144E+10	5.625E+09	2.142E+10
44	62.60	7.068E+10	6.287E+10	1.098E+10	5.410E+09	2.109E+10
45	63.98	6.655E+10	5.905E+10	1.020E+10	5.059E+09	2.044E+10

Ring index	Distance (arcsec)	$\nu F_\nu/surface\,(Hz\,Jy/arcsec^2)$				
		i	z	IRAC3.6	IRAC4.5	IRAC8.0
46	65.36	6.876E+10	6.105E+10	1.074E+10	5.337E+09	2.153E+10
47	66.74	6.580E+10	5.874E+10	1.035E+10	5.152E+09	2.134E+10
48	68.12	6.353E+10	5.702E+10	9.967E+09	4.952E+09	2.069E+10
49	69.50	5.904E+10	5.293E+10	9.061E+09	4.490E+09	1.922E+10
50	70.88	6.122E+10	5.506E+10	9.491E+09	4.702E+09	1.951E+10
51	72.26	5.890E+10	5.306E+10	9.053E+09	4.484E+09	1.867E+10
52	73.64	5.655E+10	5.064E+10	8.595E+09	4.241E+09	1.774E+10
53	75.02	5.364E+10	4.782E+10	8.048E+09	3.957E+09	1.658E+10
54	76.40	5.160E+10	4.590E+10	7.720E+09	3.803E+09	1.600E+10
55	77.78	5.074E+10	4.490E+10	7.615E+09	3.745E+09	1.560E+10
56	79.16	4.796E+10	4.261E+10	7.229E+09	3.551E+09	1.498E+10
57	80.54	4.539E+10	4.031E+10	6.847E+09	3.364E+09	1.412E+10
58	81.92	4.292E+10	3.828E+10	6.468E+09	3.170E+09	1.332E+10
59	83.30	4.255E+10	3.775E+10	6.408E+09	3.145E+09	1.287E+10
60	84.68	4.079E+10	3.594E+10	6.107E+09	2.995E+09	1.211E+10
61	86.06	3.888E+10	3.450E+10	5.787E+09	2.839E+09	1.147E+10
62	87.44	3.650E+10	3.249E+10	5.374E+09	2.626E+09	1.072E+10
63	88.82	3.704E+10	3.299E+10	5.411E+09	2.639E+09	1.050E+10
64	90.20	3.516E+10	3.162E+10	5.140E+09	2.506E+09	9.881E+09
65	91.58	3.312E+10	2.977E+10	4.877E+09	2.377E+09	9.363E+09
66	92.96	3.121E+10	2.809E+10	4.570E+09	2.224E+09	8.772E+09
67	94.34	3.096E+10	2.783E+10	4.474E+09	2.175E+09	8.365E+09
68	95.72	3.011E+10	2.705E+10	4.356E+09	2.118E+09	8.051E+09
69	97.10	2.893E+10	2.616E+10	4.192E+09	2.033E+09	7.744E+09
70	98.48	2.691E+10	2.436E+10	3.894E+09	1.889E+09	7.264E+09
71	99.86	2.636E+10	2.404E+10	3.780E+09	1.833E+09	6.980E+09
72	101.24	2.619E+10	2.379E+10	3.738E+09	1.821E+09	6.851E+09
73	102.62	2.552E+10	2.293E+10	3.623E+09	1.771E+09	6.642E+09
74	104.00	2.431E+10	2.179E+10	3.433E+09	1.692E+09	6.357E+09
75	105.38	2.301E+10	2.078E+10	3.236E+09	1.594E+09	6.101E+09
76	106.76	2.328E+10	2.107E+10	3.273E+09	1.600E+09	6.106E+09
77	108.14	2.252E+10	2.028E+10	3.162E+09	1.538E+09	5.991E+09
78	109.52	2.175E+10	1.961E+10	3.071E+09	1.493E+09	5.942E+09
79	110.90	1.994E+10	1.801E+10	2.871E+09	1.395E+09	5.803E+09
80	112.28	2.063E+10	1.874E+10	2.969E+09	1.441E+09	5.752E+09
81	113.66	1.982E+10	1.795E+10	2.864E+09	1.392E+09	5.552E+09
82	115.04	1.908E+10	1.723E+10	2.772E+09	1.351E+09	5.391E+09
83	116.42	1.825E+10	1.648E+10	2.657E+09	1.296E+09	5.235E+09
84	117.80	1.786E+10	1.617E+10	2.610E+09	1.273E+09	5.191E+09
85	119.18	1.784E+10	1.606E+10	2.620E+09	1.279E+09	5.171E+09

Ring index	Distance (arcsec)	$\nu F_\nu/surface\ (Hz\ Jy/arcsec^2)$				
		i	z	IRAC3.6	IRAC4.5	IRAC8.0
86	120.56	1.713E+10	1.547E+10	2.529E+09	1.235E+09	5.091E+09
87	121.94	1.656E+10	1.493E+10	2.456E+09	1.200E+09	5.051E+09
88	123.32	1.585E+10	1.424E+10	2.371E+09	1.161E+09	5.063E+09
89	124.70	1.637E+10	1.461E+10	2.451E+09	1.200E+09	5.038E+09
90	126.08	1.588E+10	1.419E+10	2.396E+09	1.173E+09	4.922E+09
91	127.46	1.530E+10	1.384E+10	2.322E+09	1.136E+09	4.763E+09
92	128.84	1.453E+10	1.318E+10	2.240E+09	1.098E+09	4.684E+09
93	130.22	1.483E+10	1.346E+10	2.248E+09	1.104E+09	4.476E+09
94	131.60	1.475E+10	1.342E+10	2.226E+09	1.093E+09	4.350E+09
95	132.98	1.414E+10	1.265E+10	2.110E+09	1.035E+09	4.118E+09
96	134.36	1.362E+10	1.230E+10	2.019E+09	9.894E+08	4.013E+09
97	135.74	1.358E+10	1.226E+10	1.994E+09	9.767E+08	3.923E+09
98	137.12	1.351E+10	1.220E+10	1.957E+09	9.583E+08	3.741E+09
99	138.50	1.308E+10	1.175E+10	1.888E+09	9.242E+08	3.606E+09
100	139.88	1.246E+10	1.126E+10	1.806E+09	8.863E+08	3.463E+09
101	141.26	1.197E+10	1.081E+10	1.750E+09	8.616E+08	3.411E+09
102	142.64	1.224E+10	1.106E+10	1.773E+09	8.699E+08	3.348E+09
103	144.02	1.189E+10	1.077E+10	1.724E+09	8.489E+08	3.298E+09
104	145.40	1.140E+10	1.033E+10	1.673E+09	8.224E+08	3.225E+09
105	146.78	1.069E+10	9.683E+09	1.565E+09	7.710E+08	3.155E+09
106	148.16	1.115E+10	1.010E+10	1.635E+09	8.050E+08	3.151E+09
107	149.54	1.077E+10	9.726E+09	1.578E+09	7.792E+08	3.066E+09
108	150.93	1.060E+10	9.520E+09	1.560E+09	7.710E+08	3.049E+09
109	152.31	9.654E+09	8.743E+09	1.435E+09	7.075E+08	2.938E+09
110	153.69	1.014E+10	9.179E+09	1.509E+09	7.437E+08	2.987E+09
111	155.06	9.833E+09	8.953E+09	1.469E+09	7.228E+08	2.926E+09
112	156.44	9.501E+09	8.649E+09	1.428E+09	7.025E+08	2.861E+09
113	157.82	9.131E+09	8.331E+09	1.372E+09	6.740E+08	2.756E+09
114	159.21	8.881E+09	8.115E+09	1.346E+09	6.611E+08	2.746E+09
115	160.59	9.003E+09	8.295E+09	1.357E+09	6.664E+08	2.712E+09
116	161.97	8.726E+09	7.929E+09	1.314E+09	6.448E+08	2.629E+09
117	163.34	8.401E+09	7.688E+09	1.269E+09	6.221E+08	2.529E+09
118	164.72	7.985E+09	7.278E+09	1.208E+09	5.945E+08	2.430E+09
119	166.10	8.152E+09	7.418E+09	1.229E+09	6.050E+08	2.420E+09
120	167.49	7.930E+09	7.279E+09	1.190E+09	5.852E+08	2.319E+09
121	168.87	7.603E+09	7.027E+09	1.134E+09	5.575E+08	2.197E+09
122	170.25	7.242E+09	6.651E+09	1.064E+09	5.225E+08	2.050E+09
123	171.63	7.425E+09	6.831E+09	1.104E+09	5.411E+08	2.101E+09
124	173.00	7.312E+09	6.646E+09	1.078E+09	5.288E+08	2.017E+09
125	174.39	7.145E+09	6.580E+09	1.048E+09	5.142E+08	1.927E+09

Ring index	Distance (arcsec)	$\nu F_\nu / surface\ (Hz\ Jy/arcsec^2)$				
		i	z	IRAC3.6	IRAC4.5	IRAC8.0
126	175.77	6.814E+09	6.243E+09	9.900E+08	4.857E+08	1.784E+09
127	177.15	6.872E+09	6.335E+09	9.904E+08	4.844E+08	1.730E+09
128	178.53	6.836E+09	6.331E+09	9.806E+08	4.794E+08	1.676E+09
129	179.91	6.649E+09	6.207E+09	9.514E+08	4.655E+08	1.602E+09
130	181.29	6.402E+09	5.955E+09	9.080E+08	4.448E+08	1.512E+09
131	182.67	6.218E+09	5.723E+09	8.749E+08	4.284E+08	1.438E+09
132	184.05	6.282E+09	5.751E+09	8.815E+08	4.321E+08	1.434E+09
133	185.43	6.157E+09	5.643E+09	8.652E+08	4.251E+08	1.398E+09
134	186.81	5.889E+09	5.493E+09	8.333E+08	4.095E+08	1.347E+09
135	188.19	5.616E+09	5.192E+09	7.922E+08	3.893E+08	1.288E+09
136	189.57	5.866E+09	5.365E+09	8.260E+08	4.074E+08	1.313E+09
137	190.95	5.725E+09	5.226E+09	8.056E+08	3.966E+08	1.282E+09
138	192.33	5.497E+09	5.075E+09	7.788E+08	3.827E+08	1.242E+09
139	193.71	5.200E+09	4.815E+09	7.371E+08	3.626E+08	1.197E+09
140	195.09	5.426E+09	4.987E+09	7.694E+08	3.776E+08	1.211E+09
141	196.47	5.339E+09	4.894E+09	7.578E+08	3.713E+08	1.201E+09
142	197.85	5.203E+09	4.797E+09	7.331E+08	3.600E+08	1.162E+09
143	199.23	5.062E+09	4.629E+09	7.167E+08	3.539E+08	1.141E+09
144	200.61	4.934E+09	4.526E+09	7.034E+08	3.463E+08	1.119E+09
145	201.99	5.068E+09	4.646E+09	7.266E+08	3.574E+08	1.136E+09
146	203.37	4.938E+09	4.532E+09	7.107E+08	3.499E+08	1.133E+09
147	204.75	4.831E+09	4.424E+09	6.983E+08	3.434E+08	1.142E+09
148	206.13	4.687E+09	4.306E+09	6.802E+08	3.359E+08	1.141E+09
149	207.51	4.782E+09	4.441E+09	7.110E+08	3.484E+08	1.166E+09
150	208.89	4.716E+09	4.317E+09	7.052E+08	3.475E+08	1.162E+09
151	210.27	4.573E+09	4.093E+09	6.839E+08	3.407E+08	1.153E+09
152	211.65	4.320E+09	3.943E+09	6.512E+08	3.319E+08	1.142E+09
153	213.03	4.551E+09	4.155E+09	6.885E+08	3.446E+08	1.141E+09
154	214.41	4.499E+09	4.093E+09	6.795E+08	3.378E+08	1.085E+09
155	215.79	4.465E+09	4.036E+09	6.636E+08	3.279E+08	1.058E+09
156	217.17	4.259E+09	3.842E+09	6.261E+08	3.102E+08	1.029E+09
157	218.55	4.300E+09	3.994E+09	6.308E+08	3.156E+08	1.019E+09
158	219.93	4.314E+09	4.039E+09	6.335E+08	3.195E+08	1.023E+09
159	221.31	4.292E+09	3.949E+09	6.313E+08	3.166E+08	1.026E+09
160	222.69	4.124E+09	3.783E+09	6.150E+08	3.061E+08	1.022E+09
161	224.07	4.015E+09	3.719E+09	6.085E+08	3.033E+08	1.008E+09
162	225.45	4.155E+09	3.836E+09	6.343E+08	3.155E+08	1.037E+09
163	226.83	4.021E+09	3.770E+09	6.224E+08	3.115E+08	1.035E+09
164	228.21	3.980E+09	3.701E+09	6.154E+08	3.068E+08	1.022E+09
165	229.59	3.782E+09	3.512E+09	5.863E+08	2.908E+08	9.947E+08

Ring index	Distance (arcsec)	$\nu F_\nu/surface\,(Hz\,Jy/arcsec^2)$				
		i	z	IRAC3.6	IRAC4.5	IRAC8.0
166	230.97	3.984E+09	3.720E+09	6.100E+08	3.021E+08	9.993E+08
167	232.35	3.892E+09	3.604E+09	5.943E+08	2.947E+08	9.842E+08
168	233.73	3.831E+09	3.529E+09	5.817E+08	2.891E+08	9.790E+08
169	235.11	3.590E+09	3.351E+09	5.481E+08	2.711E+08	9.587E+08
170	236.49	3.822E+09	3.581E+09	5.807E+08	2.855E+08	9.745E+08
171	237.87	3.817E+09	3.542E+09	5.741E+08	2.810E+08	9.636E+08
172	239.25	3.828E+09	3.513E+09	5.772E+08	2.820E+08	9.779E+08
173	240.63	3.707E+09	3.414E+09	5.595E+08	2.743E+08	9.659E+08
174	242.01	3.703E+09	3.403E+09	5.500E+08	2.708E+08	9.396E+08
175	243.39	3.861E+09	3.535E+09	5.670E+08	2.805E+08	9.540E+08
176	244.77	3.797E+09	3.474E+09	5.558E+08	2.755E+08	9.475E+08
177	246.15	3.730E+09	3.438E+09	5.445E+08	2.693E+08	9.404E+08
178	247.53	3.613E+09	3.349E+09	5.190E+08	2.562E+08	8.885E+08
179	248.91	3.773E+09	3.460E+09	5.378E+08	2.649E+08	8.936E+08
180	250.29	3.760E+09	3.417E+09	5.254E+08	2.579E+08	8.680E+08
181	251.67	3.725E+09	3.400E+09	5.158E+08	2.528E+08	8.475E+08
182	253.05	3.536E+09	3.202E+09	4.821E+08	2.381E+08	8.040E+08
183	254.43	3.756E+09	3.401E+09	5.125E+08	2.536E+08	8.147E+08
184	255.81	3.681E+09	3.350E+09	5.041E+08	2.515E+08	7.992E+08
185	257.19	3.629E+09	3.298E+09	4.931E+08	2.461E+08	7.788E+08
186	258.57	3.496E+09	3.163E+09	4.780E+08	2.419E+08	7.690E+08
187	259.95	3.532E+09	3.211E+09	4.807E+08	2.425E+08	7.504E+08
188	261.33	3.599E+09	3.239E+09	4.874E+08	2.448E+08	7.533E+08
189	262.71	3.553E+09	3.239E+09	4.844E+08	2.428E+08	7.485E+08
190	264.09	3.447E+09	3.147E+09	4.692E+08	2.342E+08	7.396E+08
191	265.47	3.363E+09	3.105E+09	4.588E+08	2.295E+08	7.272E+08
192	266.85	3.497E+09	3.277E+09	4.792E+08	2.388E+08	7.271E+08
193	268.23	3.446E+09	3.195E+09	4.730E+08	2.362E+08	7.188E+08
194	269.61	3.406E+09	3.139E+09	4.645E+08	2.324E+08	7.079E+08
195	270.99	3.263E+09	2.987E+09	4.479E+08	2.252E+08	6.916E+08
196	272.37	3.430E+09	3.226E+09	4.675E+08	2.350E+08	6.697E+08
197	273.75	3.425E+09	3.176E+09	4.640E+08	2.340E+08	6.492E+08
198	275.13	3.386E+09	3.143E+09	4.567E+08	2.314E+08	6.278E+08
199	276.51	3.151E+09	2.862E+09	4.281E+08	2.170E+08	6.069E+08

Table A.3: Result of the fluxes after dust correction, filters from SDSS i to Spitzer IRAC8.0

Result of the fluxes after dust correction, filters from Spitzer MIPS24 to Herschel PACS160

Ring index	Distance (arcsec)	$\nu F_\nu / surface\ (Hz\ Jy/arcsec^2)$			
		MIPS24	PACS70	PACS100	PACS160
0	1.88	6.039E+09	5.336E+10	5.059E+10	2.629E+10
1	3.26	5.642E+09	5.186E+10	4.996E+10	2.639E+10
2	4.64	4.824E+09	4.815E+10	4.867E+10	2.647E+10
3	6.02	4.724E+09	4.669E+10	4.783E+10	2.653E+10
4	7.40	4.406E+09	4.378E+10	4.619E+10	2.656E+10
5	8.78	4.109E+09	4.048E+10	4.407E+10	2.652E+10
6	10.16	3.742E+09	3.642E+10	4.151E+10	2.642E+10
7	11.54	3.682E+09	3.475E+10	4.032E+10	2.637E+10
8	12.92	3.570E+09	3.236E+10	3.853E+10	2.625E+10
9	14.30	3.471E+09	3.072E+10	3.750E+10	2.627E+10
10	15.68	3.275E+09	2.775E+10	3.541E+10	2.598E+10
11	17.06	3.233E+09	2.716E+10	3.522E+10	2.612E+10
12	18.44	3.286E+09	2.685E+10	3.496E+10	2.619E+10
13	19.82	3.288E+09	2.639E+10	3.489E+10	2.641E+10
14	21.20	3.274E+09	2.554E+10	3.460E+10	2.661E+10
15	22.58	3.326E+09	2.547E+10	3.519E+10	2.704E+10
16	23.96	3.556E+09	2.739E+10	3.725E+10	2.796E+10
17	25.34	3.718E+09	2.808E+10	3.849E+10	2.873E+10
18	26.72	3.920E+09	2.914E+10	4.015E+10	2.960E+10
19	28.10	4.193E+09	3.060E+10	4.241E+10	3.072E+10
20	29.48	4.480E+09	3.298E+10	4.476E+10	3.159E+10
21	30.86	4.796E+09	3.505E+10	4.721E+10	3.269E+10
22	32.24	5.140E+09	3.716E+10	4.977E+10	3.387E+10
23	33.62	5.494E+09	3.921E+10	5.235E+10	3.494E+10
24	35.00	5.852E+09	4.155E+10	5.525E+10	3.617E+10
25	36.38	6.055E+09	4.297E+10	5.675E+10	3.656E+10
26	37.76	6.364E+09	4.516E+10	5.927E+10	3.746E+10
27	39.14	6.620E+09	4.692E+10	6.111E+10	3.795E+10
28	40.52	6.968E+09	4.904E+10	6.345E+10	3.882E+10
29	41.90	6.987E+09	4.866E+10	6.289E+10	3.830E+10
30	43.28	7.060E+09	4.837E+10	6.254E+10	3.807E+10
31	44.66	7.120E+09	4.784E+10	6.187E+10	3.783E+10
32	46.04	7.118E+09	4.687E+10	6.059E+10	3.733E+10
33	47.42	6.915E+09	4.517E+10	5.834E+10	3.604E+10
34	48.80	6.822E+09	4.409E+10	5.696E+10	3.548E+10
35	50.18	6.619E+09	4.209E+10	5.468E+10	3.451E+10
36	51.56	6.523E+09	4.109E+10	5.342E+10	3.412E+10
37	52.94	6.355E+09	3.997E+10	5.206E+10	3.329E+10
38	54.32	6.227E+09	3.910E+10	5.100E+10	3.262E+10
39	55.70	6.111E+09	3.824E+10	5.003E+10	3.215E+10

Ring index	Distance (arcsec)	$\nu F_\nu / surface\ (Hz\ Jy/arcsec^2)$			
		MIPS24	PACS70	PACS100	PACS160
40	57.08	5.967E+09	3.710E+10	4.878E+10	3.165E+10
41	58.46	5.947E+09	3.678E+10	4.812E+10	3.142E+10
42	59.84	5.918E+09	3.675E+10	4.789E+10	3.102E+10
43	61.22	5.759E+09	3.546E+10	4.646E+10	3.038E+10
44	62.60	5.683E+09	3.480E+10	4.561E+10	3.001E+10
45	63.98	5.525E+09	3.334E+10	4.376E+10	2.921E+10
46	65.36	5.652E+09	3.429E+10	4.447E+10	2.904E+10
47	66.74	5.513E+09	3.298E+10	4.289E+10	2.815E+10
48	68.12	5.363E+09	3.171E+10	4.158E+10	2.750E+10
49	69.50	5.015E+09	2.907E+10	3.875E+10	2.631E+10
50	70.88	4.988E+09	2.919E+10	3.881E+10	2.609E+10
51	72.26	4.744E+09	2.756E+10	3.691E+10	2.520E+10
52	73.64	4.502E+09	2.591E+10	3.498E+10	2.427E+10
53	75.02	4.244E+09	2.417E+10	3.301E+10	2.336E+10
54	76.40	4.079E+09	2.302E+10	3.156E+10	2.258E+10
55	77.78	3.980E+09	2.236E+10	3.087E+10	2.209E+10
56	79.16	3.800E+09	2.114E+10	2.936E+10	2.125E+10
57	80.54	3.588E+09	1.974E+10	2.772E+10	2.039E+10
58	81.92	3.379E+09	1.840E+10	2.612E+10	1.958E+10
59	83.30	3.302E+09	1.798E+10	2.563E+10	1.926E+10
60	84.68	3.117E+09	1.677E+10	2.419E+10	1.846E+10
61	86.06	2.946E+09	1.564E+10	2.276E+10	1.764E+10
62	87.44	2.724E+09	1.426E+10	2.109E+10	1.672E+10
63	88.82	2.708E+09	1.421E+10	2.096E+10	1.664E+10
64	90.20	2.554E+09	1.326E+10	1.981E+10	1.595E+10
65	91.58	2.408E+09	1.235E+10	1.860E+10	1.521E+10
66	92.96	2.253E+09	1.144E+10	1.740E+10	1.448E+10
67	94.34	2.189E+09	1.106E+10	1.691E+10	1.426E+10
68	95.72	2.101E+09	1.055E+10	1.624E+10	1.387E+10
69	97.10	2.008E+09	1.001E+10	1.549E+10	1.342E+10
70	98.48	1.865E+09	9.160E+09	1.433E+10	1.263E+10
71	99.86	1.806E+09	8.831E+09	1.392E+10	1.237E+10
72	101.24	1.770E+09	8.546E+09	1.358E+10	1.211E+10
73	102.62	1.717E+09	8.211E+09	1.314E+10	1.179E+10
74	104.00	1.638E+09	7.708E+09	1.245E+10	1.124E+10
75	105.38	1.550E+09	7.245E+09	1.179E+10	1.072E+10
76	106.76	1.551E+09	7.212E+09	1.176E+10	1.068E+10
77	108.14	1.505E+09	6.958E+09	1.141E+10	1.038E+10
78	109.52	1.455E+09	6.685E+09	1.100E+10	1.002E+10
79	110.90	1.366E+09	6.222E+09	1.029E+10	9.377E+09

Ring index	Distance (arcsec)	$\nu F_\nu / surface\ (Hz\ Jy/arcsec^2)$			
		MIPS24	PACS70	PACS100	PACS160
80	112.28	1.385E+09	6.369E+09	1.043E+10	9.519E+09
81	113.66	1.330E+09	6.099E+09	9.992E+09	9.174E+09
82	115.04	1.282E+09	5.832E+09	9.583E+09	8.847E+09
83	116.42	1.227E+09	5.563E+09	9.151E+09	8.468E+09
84	117.80	1.201E+09	5.416E+09	8.910E+09	8.250E+09
85	119.18	1.193E+09	5.384E+09	8.830E+09	8.203E+09
86	120.56	1.151E+09	5.158E+09	8.479E+09	7.876E+09
87	121.94	1.121E+09	4.992E+09	8.227E+09	7.608E+09
88	123.32	1.095E+09	4.849E+09	7.967E+09	7.307E+09
89	124.70	1.102E+09	4.924E+09	8.017E+09	7.392E+09
90	126.08	1.072E+09	4.788E+09	7.730E+09	7.137E+09
91	127.46	1.037E+09	4.601E+09	7.418E+09	6.861E+09
92	128.84	1.017E+09	4.500E+09	7.225E+09	6.632E+09
93	130.22	9.885E+08	4.395E+09	7.078E+09	6.598E+09
94	131.60	9.753E+08	4.373E+09	7.000E+09	6.536E+09
95	132.98	9.236E+08	4.145E+09	6.627E+09	6.250E+09
96	134.36	8.915E+08	4.024E+09	6.424E+09	6.075E+09
97	135.74	8.721E+08	3.956E+09	6.326E+09	6.046E+09
98	137.12	8.416E+08	3.844E+09	6.154E+09	5.957E+09
99	138.50	8.076E+08	3.689E+09	5.939E+09	5.810E+09
100	139.88	7.713E+08	3.471E+09	5.693E+09	5.632E+09
101	141.26	7.488E+08	3.349E+09	5.546E+09	5.517E+09
102	142.64	7.386E+08	3.364E+09	5.511E+09	5.528E+09
103	144.02	7.153E+08	3.261E+09	5.348E+09	5.393E+09
104	145.40	6.938E+08	3.153E+09	5.187E+09	5.264E+09
105	146.78	6.679E+08	3.002E+09	4.937E+09	5.054E+09
106	148.16	6.726E+08	3.047E+09	5.001E+09	5.128E+09
107	149.54	6.455E+08	2.868E+09	4.784E+09	4.943E+09
108	150.93	6.308E+08	2.774E+09	4.690E+09	4.845E+09
109	152.31	5.965E+08	2.587E+09	4.375E+09	4.578E+09
110	153.69	6.083E+08	2.688E+09	4.488E+09	4.648E+09
111	155.06	5.906E+08	2.622E+09	4.343E+09	4.513E+09
112	156.44	5.728E+08	2.535E+09	4.191E+09	4.369E+09
113	157.82	5.508E+08	2.429E+09	4.016E+09	4.228E+09
114	159.21	5.434E+08	2.380E+09	3.920E+09	4.135E+09
115	160.59	5.420E+08	2.376E+09	3.877E+09	4.110E+09
116	161.97	5.216E+08	2.260E+09	3.706E+09	3.963E+09
117	163.34	5.003E+08	2.147E+09	3.559E+09	3.840E+09
118	164.72	4.798E+08	2.010E+09	3.380E+09	3.697E+09
119	166.10	4.839E+08	2.028E+09	3.382E+09	3.699E+09

Ring index	Distance (arcsec)	$\nu F_\nu / surface \ (Hz \ Jy/arcsec^2)$			
		MIPS24	PACS70	PACS100	PACS160
120	167.49	4.707E+08	1.962E+09	3.255E+09	3.600E+09
121	168.87	4.470E+08	1.843E+09	3.079E+09	3.446E+09
122	170.25	4.227E+08	1.731E+09	2.902E+09	3.296E+09
123	171.63	4.309E+08	1.790E+09	2.939E+09	3.298E+09
124	173.00	4.190E+08	1.738E+09	2.836E+09	3.208E+09
125	174.39	4.034E+08	1.677E+09	2.724E+09	3.107E+09
126	175.77	3.770E+08	1.566E+09	2.545E+09	2.947E+09
127	177.15	3.746E+08	1.568E+09	2.541E+09	2.934E+09
128	178.53	3.664E+08	1.559E+09	2.483E+09	2.870E+09
129	179.91	3.525E+08	1.505E+09	2.374E+09	2.783E+09
130	181.29	3.313E+08	1.420E+09	2.235E+09	2.668E+09
131	182.67	3.157E+08	1.363E+09	2.130E+09	2.586E+09
132	184.05	3.150E+08	1.354E+09	2.124E+09	2.568E+09
133	185.43	3.061E+08	1.311E+09	2.058E+09	2.515E+09
134	186.81	2.911E+08	1.232E+09	1.954E+09	2.415E+09
135	188.19	2.746E+08	1.155E+09	1.830E+09	2.305E+09
136	189.57	2.843E+08	1.212E+09	1.908E+09	2.361E+09
137	190.95	2.756E+08	1.186E+09	1.845E+09	2.294E+09
138	192.33	2.640E+08	1.143E+09	1.753E+09	2.203E+09
139	193.71	2.512E+08	1.081E+09	1.646E+09	2.104E+09
140	195.09	2.606E+08	1.122E+09	1.707E+09	2.158E+09
141	196.47	2.585E+08	1.113E+09	1.691E+09	2.132E+09
142	197.85	2.495E+08	1.064E+09	1.615E+09	2.056E+09
143	199.23	2.435E+08	1.030E+09	1.568E+09	2.003E+09
144	200.61	2.382E+08	9.927E+08	1.533E+09	1.955E+09
145	201.99	2.433E+08	1.038E+09	1.593E+09	1.994E+09
146	203.37	2.389E+08	1.027E+09	1.571E+09	1.945E+09
147	204.75	2.350E+08	1.011E+09	1.536E+09	1.898E+09
148	206.13	2.312E+08	9.866E+08	1.494E+09	1.849E+09
149	207.51	2.396E+08	9.890E+08	1.532E+09	1.877E+09
150	208.89	2.407E+08	9.653E+08	1.521E+09	1.855E+09
151	210.27	2.400E+08	9.446E+08	1.479E+09	1.808E+09
152	211.65	2.373E+08	9.427E+08	1.415E+09	1.743E+09
153	213.03	2.486E+08	1.005E+09	1.466E+09	1.793E+09
154	214.41	2.453E+08	9.994E+08	1.435E+09	1.760E+09
155	215.79	2.405E+08	9.777E+08	1.408E+09	1.737E+09
156	217.17	2.276E+08	9.277E+08	1.335E+09	1.678E+09
157	218.55	2.225E+08	9.205E+08	1.331E+09	1.678E+09
158	219.93	2.189E+08	9.073E+08	1.328E+09	1.668E+09
159	221.31	2.166E+08	9.019E+08	1.320E+09	1.654E+09

Ring index	Distance (arcsec)	$\nu F_\nu/surface\ (Hz\ Jy/arcsec^2)$			
		MIPS24	PACS70	PACS100	PACS160
160	222.69	2.116E+08	9.000E+08	1.288E+09	1.613E+09
161	224.07	2.078E+08	8.883E+08	1.266E+09	1.580E+09
162	225.45	2.139E+08	9.176E+08	1.314E+09	1.611E+09
163	226.83	2.124E+08	8.966E+08	1.290E+09	1.586E+09
164	228.21	2.112E+08	8.979E+08	1.279E+09	1.571E+09
165	229.59	2.039E+08	8.652E+08	1.223E+09	1.525E+09
166	230.97	2.088E+08	9.109E+08	1.276E+09	1.567E+09
167	232.35	2.066E+08	9.132E+08	1.258E+09	1.549E+09
168	233.73	2.033E+08	9.167E+08	1.237E+09	1.529E+09
169	235.11	1.959E+08	8.787E+08	1.187E+09	1.486E+09
170	236.49	1.984E+08	8.978E+08	1.231E+09	1.515E+09
171	237.87	1.935E+08	8.685E+08	1.207E+09	1.495E+09
172	239.25	1.918E+08	8.618E+08	1.196E+09	1.482E+09
173	240.63	1.867E+08	8.300E+08	1.167E+09	1.442E+09
174	242.01	1.826E+08	8.138E+08	1.148E+09	1.427E+09
175	243.39	1.848E+08	8.306E+08	1.174E+09	1.437E+09
176	244.77	1.808E+08	8.130E+08	1.147E+09	1.413E+09
177	246.15	1.773E+08	7.932E+08	1.126E+09	1.394E+09
178	247.53	1.688E+08	7.559E+08	1.072E+09	1.358E+09
179	248.91	1.710E+08	7.664E+08	1.091E+09	1.370E+09
180	250.29	1.671E+08	7.478E+08	1.063E+09	1.350E+09
181	251.67	1.643E+08	7.196E+08	1.048E+09	1.334E+09
182	253.05	1.565E+08	6.769E+08	1.001E+09	1.296E+09
183	254.43	1.610E+08	7.025E+08	1.029E+09	1.311E+09
184	255.81	1.586E+08	6.906E+08	1.005E+09	1.292E+09
185	257.19	1.552E+08	6.760E+08	9.864E+08	1.268E+09
186	258.57	1.522E+08	6.601E+08	9.618E+08	1.245E+09
187	259.95	1.508E+08	6.668E+08	9.587E+08	1.232E+09
188	261.33	1.521E+08	6.733E+08	9.629E+08	1.225E+09
189	262.71	1.516E+08	6.763E+08	9.639E+08	1.212E+09
190	264.09	1.481E+08	6.586E+08	9.361E+08	1.178E+09
191	265.47	1.452E+08	6.537E+08	9.248E+08	1.155E+09
192	266.85	1.479E+08	6.786E+08	9.395E+08	1.154E+09
193	268.23	1.464E+08	6.755E+08	9.290E+08	1.133E+09
194	269.61	1.445E+08	6.704E+08	9.264E+08	1.112E+09
195	270.99	1.402E+08	6.502E+08	9.052E+08	1.079E+09
196	272.37	1.412E+08	6.690E+08	9.118E+08	1.073E+09
197	273.75	1.399E+08	6.684E+08	9.017E+08	1.053E+09
198	275.13	1.375E+08	6.628E+08	8.954E+08	1.032E+09

Ring index	Distance (arcsec)	$\nu F_\nu / surface \, (Hz \, Jy/arcsec^2)$			
		MIPS24	PACS70	PACS100	PACS160
199	276.51	1.327E+08	6.377E+08	8.690E+08	9.969E+08

Table A.4: Result of the fluxes after dust correction, filters from Spitzer MIPS24 to Herschel PACS160

Appendix B

Tables of mass

Parameters obtained for the two burst fit with simuated annealing

Index	I_{young}	$t_{0,young}$	τ_{young}	I_{old}	$t_{0,old}$	τ_{old}	χ^2
0	0.000E+00	0.371	-0.100	5.226E+09	13.000	-0.039	91.429
1	3.843E-27	0.343	-0.035	5.704E+09	13.023	-0.074	90.904
2	3.306E-09	0.277	-0.081	5.826E+09	12.996	-0.133	93.701
3	7.010E-29	0.270	-0.100	5.671E+09	13.105	-0.240	86.661
4	6.270E+05	0.178	-0.093	8.321E+09	13.042	-0.063	83.533
5	4.209E+06	0.223	-0.099	8.975E+09	13.080	-0.095	74.282
6	1.713E+07	0.359	-0.099	7.443E+09	12.671	-0.637	61.459
7	6.390E+07	0.208	-0.029	4.773E+09	12.505	-0.774	58.495
8	2.165E+08	0.292	-0.030	3.832E+09	13.038	-0.501	60.048
9	1.535E+08	0.262	-0.022	3.624E+09	13.173	-0.639	59.830
10	2.919E+08	0.287	-0.028	2.684E+09	12.643	-1.253	58.865
11	2.179E+08	0.248	-0.022	2.887E+09	13.253	-0.857	68.383
12	2.271E+08	0.246	-0.022	2.887E+09	13.259	-0.844	75.209
13	5.675E+08	0.300	-0.027	2.794E+09	13.169	-0.798	81.164
14	5.389E+08	0.285	-0.025	2.668E+09	13.150	-0.711	89.400
15	3.395E+08	0.248	-0.022	2.590E+09	12.779	-1.194	90.037
16	4.297E+08	0.269	-0.022	2.742E+09	12.830	-1.224	85.895
17	4.357E+08	0.254	-0.022	2.682E+09	12.852	-1.182	94.655
18	7.698E+08	0.289	-0.023	2.234E+09	12.625	-1.130	102.096
19	7.745E+08	0.269	-0.023	2.085E+09	12.652	-1.104	115.771
20	9.550E+08	0.261	-0.023	2.236E+09	12.663	-1.081	118.226
21	1.169E+09	0.259	-0.024	2.296E+09	12.673	-1.052	140.443
22	1.424E+09	0.275	-0.024	1.964E+09	12.874	-1.095	162.938
23	1.549E+09	0.267	-0.024	1.085E+09	12.855	-1.459	200.701
24	2.183E+09	0.282	-0.025	1.097E+09	12.794	-1.192	220.254
25	2.428E+09	0.292	-0.025	7.423E+08	12.793	-1.249	204.610

Index	I_{young}	$t_{0,young}$	τ_{young}	I_{old}	$t_{0,old}$	τ_{old}	χ^2
26	2.726E+09	0.272	-0.027	5.589E+08	13.281	-1.537	204.159
27	3.340E+09	0.288	-0.028	3.383E+08	13.416	-0.943	209.799
28	2.808E+09	0.244	-0.025	2.284E+08	13.260	-0.994	232.753
29	2.955E+09	0.249	-0.025	2.450E+08	13.315	-0.957	219.840
30	3.000E+09	0.243	-0.025	1.089E+08	13.309	-1.463	238.092
31	3.402E+09	0.242	-0.027	2.850E+08	13.222	-1.088	278.199
32	2.998E+09	0.228	-0.026	1.393E+09	12.916	-0.693	284.590
33	3.822E+09	0.252	-0.028	2.059E+08	13.364	-0.804	256.043
34	4.021E+09	0.255	-0.030	2.612E+08	13.212	-0.953	260.347
35	3.752E+09	0.248	-0.028	1.527E+08	12.972	-1.285	237.825
36	3.755E+09	0.246	-0.028	1.017E+08	13.090	-0.686	236.221
37	3.073E+09	0.232	-0.026	8.366E-09	13.237	-0.670	267.047
38	3.119E+09	0.232	-0.026	1.073E-02	13.245	-0.768	249.385
39	3.507E+09	0.234	-0.029	5.083E+08	13.143	-0.724	275.374
40	3.616E+09	0.236	-0.028	5.577E-07	12.891	-2.501	228.968
41	2.788E+09	0.215	-0.026	1.547E-03	12.918	-0.820	243.995
42	3.460E+09	0.227	-0.028	2.679E-17	13.304	-1.411	243.136
43	2.930E+09	0.215	-0.026	1.601E-07	13.351	-0.826	252.246
44	3.268E+09	0.220	-0.028	3.927E+05	13.337	-0.912	250.488
45	3.009E+09	0.214	-0.028	1.410E-64	13.121	-1.157	290.155
46	3.032E+09	0.211	-0.027	7.778E+04	13.143	-0.633	279.742
47	3.309E+09	0.218	-0.029	3.217E-06	13.207	-1.490	248.268
48	2.634E+09	0.201	-0.026	9.130E+04	13.118	-0.786	248.551
49	2.821E+09	0.211	-0.027	1.790E-04	13.165	-1.621	245.401
50	3.341E+09	0.223	-0.028	2.527E-34	13.196	-1.435	253.532
51	3.511E+09	0.230	-0.029	1.497E-06	13.241	-1.127	255.374
52	3.035E+09	0.222	-0.028	3.585E-04	13.226	-1.942	260.667
53	2.359E+09	0.206	-0.026	2.896E-07	13.248	-2.057	251.074
54	2.198E+09	0.202	-0.025	9.523E-08	13.235	-2.611	237.016
55	2.028E+09	0.194	-0.025	2.852E-01	12.918	-0.987	213.994
56	1.855E+09	0.185	-0.025	9.956E+07	12.940	-0.903	199.612
57	1.886E+09	0.190	-0.025	1.945E+06	13.048	-0.846	182.438
58	2.128E+09	0.202	-0.026	4.065E-07	13.425	-2.013	177.518
59	2.039E+09	0.196	-0.026	6.807E+05	13.415	-0.886	184.434
60	2.028E+09	0.199	-0.026	3.417E+04	13.469	-4.145	178.900
61	1.793E+09	0.193	-0.025	2.955E+06	13.476	-3.001	188.744
62	2.027E+09	0.207	-0.028	1.826E+07	13.494	-4.620	156.395
63	1.985E+09	0.205	-0.027	4.381E+07	13.482	-3.259	152.602
64	2.329E+09	0.222	-0.031	5.055E+07	13.059	-3.587	137.942
65	1.473E+09	0.178	-0.025	5.553E+07	13.318	-2.821	131.082
66	1.543E+09	0.189	-0.026	3.348E+07	13.432	-3.423	135.960

Index	I_{young}	$t_{0,young}$	τ_{young}	I_{old}	$t_{0,old}$	τ_{old}	χ^2
67	1.716E+09	0.202	-0.029	8.984E+07	13.395	-3.160	116.031
68	1.453E+09	0.188	-0.027	1.082E+08	13.361	-3.267	119.400
69	1.224E+09	0.179	-0.025	4.732E+07	13.265	-5.052	125.374
70	1.413E+09	0.193	-0.026	2.982E+07	13.234	-3.085	130.649
71	2.152E+09	0.242	-0.037	6.596E+07	13.105	-3.201	108.801
72	1.352E+09	0.196	-0.027	7.103E+07	13.348	-3.824	115.813
73	1.250E+09	0.187	-0.027	9.887E+07	13.471	-3.323	103.412
74	1.139E+09	0.178	-0.026	9.588E+07	13.385	-2.999	98.580
75	1.100E+09	0.175	-0.026	8.666E+07	13.292	-2.884	102.707
76	1.511E+09	0.212	-0.031	1.367E+08	13.282	-2.569	89.811
77	1.610E+09	0.223	-0.031	5.612E+07	13.296	-4.541	99.282
78	1.295E+09	0.198	-0.030	1.458E+08	13.284	-2.687	88.331
79	1.155E+09	0.196	-0.029	5.795E+07	13.056	-4.889	94.605
80	1.853E+09	0.249	-0.040	1.080E+08	13.237	-2.282	100.284
81	1.038E+09	0.166	-0.027	1.365E+08	13.269	-2.812	102.152
82	7.916E+08	0.150	-0.023	6.782E+07	13.359	-2.619	151.678
83	1.564E+09	0.237	-0.040	9.252E+07	13.246	-2.831	128.291
84	8.204E+08	0.161	-0.025	3.806E+07	13.335	-6.545	115.272
85	1.155E+09	0.191	-0.031	1.045E+08	13.322	-3.279	112.557
86	1.103E+09	0.186	-0.031	1.009E+08	13.237	-3.293	117.823
87	8.854E+08	0.150	-0.025	1.015E+08	13.199	-2.659	115.163
88	1.239E+09	0.212	-0.036	8.563E+07	13.205	-3.010	113.703
89	1.199E+09	0.202	-0.034	9.379E+07	13.294	-3.176	121.473
90	1.447E+09	0.231	-0.039	5.866E+07	13.332	-3.751	134.984
91	8.797E+08	0.153	-0.026	7.713E+07	13.204	-3.572	130.267
92	9.096E+08	0.155	-0.027	5.924E+07	13.191	-3.957	136.374
93	8.330E+08	0.150	-0.026	8.685E+07	13.266	-3.437	149.286
94	1.151E+09	0.205	-0.035	9.721E+07	13.045	-2.984	128.059
95	1.069E+09	0.198	-0.033	6.680E+07	13.311	-3.937	142.665
96	9.508E+08	0.176	-0.030	7.273E+07	13.264	-3.840	130.637
97	9.657E+08	0.177	-0.030	8.772E+07	13.178	-3.389	117.508
98	1.155E+09	0.218	-0.037	7.417E+07	13.196	-3.635	109.390
99	8.996E+08	0.169	-0.029	7.846E+07	13.188	-3.624	111.186
100	9.166E+08	0.171	-0.030	1.119E+08	13.228	-2.762	97.482
101	1.464E+09	0.251	-0.043	3.501E+07	13.280	-2.323	111.939
102	7.822E+08	0.150	-0.026	1.182E+08	13.170	-2.183	103.024
103	1.019E+09	0.206	-0.036	1.072E+08	13.204	-2.621	91.660
104	8.406E+08	0.157	-0.027	1.281E+08	13.372	-2.235	97.192
105	9.697E+08	0.213	-0.039	7.487E+07	13.262	-3.059	90.275
106	9.351E+08	0.187	-0.032	7.401E+07	13.195	-3.237	99.766
107	9.444E+08	0.198	-0.033	5.695E+07	13.253	-3.777	116.642

Index	I_{young}	$t_{0,young}$	τ_{young}	I_{old}	$t_{0,old}$	τ_{old}	χ^2
108	7.559E+08	0.155	-0.027	6.541E+07	13.090	-3.269	114.015
109	8.570E+08	0.191	-0.035	9.284E+07	13.356	-2.620	114.105
110	8.085E+08	0.161	-0.028	8.253E+07	13.402	-2.871	136.084
111	8.670E+08	0.181	-0.033	1.705E+08	13.089	-1.469	118.281
112	8.668E+08	0.209	-0.037	6.728E+07	13.452	-3.669	98.942
113	5.911E+08	0.162	-0.026	2.291E+07	13.314	-8.859	111.333
114	7.572E+08	0.177	-0.032	7.604E+07	13.290	-3.291	103.755
115	6.993E+08	0.173	-0.029	5.906E+07	13.338	-4.369	92.353
116	1.009E+09	0.244	-0.042	3.812E+07	13.266	-4.571	98.749
117	6.627E+08	0.200	-0.029	2.236E+07	13.443	-9.428	101.187
118	6.340E+08	0.180	-0.029	3.648E+07	13.351	-5.434	113.381
119	6.897E+08	0.184	-0.030	6.476E+07	13.283	-3.521	119.837
120	8.448E+08	0.225	-0.036	5.223E+07	12.976	-4.049	105.645
121	5.164E+08	0.150	-0.026	1.108E+08	12.979	-2.520	99.218
122	5.651E+08	0.174	-0.027	4.878E+07	13.087	-3.899	118.362
123	4.832E+08	0.158	-0.025	6.389E+07	12.981	-3.503	106.330
124	4.337E+08	0.150	-0.024	6.056E+07	13.309	-3.316	106.204
125	4.559E+08	0.160	-0.025	6.386E+07	13.012	-3.328	95.672
126	4.907E+08	0.173	-0.026	6.204E+07	13.077	-3.290	86.843
127	4.099E+08	0.157	-0.024	5.952E+07	13.081	-3.313	92.914
128	2.862E+08	0.150	-0.022	1.322E+07	13.088	-3.059	163.144
129	6.059E+08	0.211	-0.030	5.969E+07	13.155	-3.677	92.562
130	4.870E+08	0.202	-0.027	4.850E+07	13.142	-4.378	86.649
131	4.732E+08	0.185	-0.027	8.092E+07	13.120	-2.782	94.428
132	3.402E+08	0.156	-0.023	7.029E+07	13.009	-2.934	93.620
133	3.446E+08	0.163	-0.024	6.814E+07	12.987	-3.375	100.326
134	4.050E+08	0.179	-0.026	8.446E+07	12.972	-3.069	74.732
135	3.120E+08	0.152	-0.024	6.591E+07	13.083	-3.040	86.967
136	3.559E+08	0.173	-0.024	6.396E+07	13.005	-3.233	104.313
137	3.265E+08	0.193	-0.023	3.040E+07	12.951	-5.119	105.474
138	3.786E+08	0.185	-0.025	6.849E+07	12.961	-3.115	112.355
139	4.462E+08	0.202	-0.027	5.300E+07	13.032	-3.297	119.910
140	2.706E+08	0.157	-0.023	5.685E+07	12.953	-3.137	118.894
141	4.445E+08	0.198	-0.028	8.945E+07	13.434	-2.827	102.085
142	5.641E+08	0.232	-0.029	4.096E+07	12.982	-4.220	114.331
143	3.962E+08	0.202	-0.026	5.376E+07	13.015	-3.446	110.133
144	5.493E+08	0.225	-0.030	5.636E+07	13.077	-3.105	103.021
145	4.376E+08	0.202	-0.027	6.526E+07	13.072	-2.904	111.016
146	3.555E+08	0.185	-0.025	6.969E+07	12.928	-2.879	116.865
147	3.412E+08	0.180	-0.025	5.477E+07	13.041	-3.222	106.656
148	4.508E+08	0.204	-0.029	6.422E+07	13.111	-3.011	102.356

Index	I_{young}	$t_{0,young}$	τ_{young}	I_{old}	$t_{0,old}$	τ_{old}	χ^2
149	4.363E+08	0.196	-0.028	7.108E+07	13.143	-2.929	100.552
150	4.001E+08	0.186	-0.027	7.209E+07	12.882	-3.103	131.165
151	4.242E+08	0.192	-0.028	5.591E+07	13.001	-3.373	153.878
152	3.038E+08	0.179	-0.024	1.474E+07	13.023	-7.525	215.601
153	4.320E+08	0.191	-0.030	8.235E+07	12.894	-3.028	116.499
154	3.656E+08	0.205	-0.025	1.821E+07	12.979	-7.976	147.805
155	3.121E+08	0.152	-0.024	6.199E+07	12.968	-3.276	163.131
156	3.744E+08	0.175	-0.028	5.369E+07	13.160	-3.599	120.352
157	4.390E+08	0.200	-0.032	6.749E+07	13.070	-3.143	94.432
158	5.436E+08	0.241	-0.032	2.392E+07	13.075	-7.050	99.335
159	2.769E+08	0.185	-0.025	3.031E+07	12.880	-6.428	95.116
160	3.729E+08	0.156	-0.028	8.839E+07	13.084	-2.554	113.808
161	4.333E+08	0.215	-0.033	3.880E+07	12.950	-5.170	104.927
162	2.333E+08	0.187	-0.023	9.353E+06	13.038	-22.937	108.790
163	3.514E+08	0.179	-0.029	4.715E+07	12.972	-4.819	88.572
164	4.269E+08	0.222	-0.042	6.751E+07	13.333	-3.545	63.434
165	4.026E+08	0.224	-0.044	7.141E+07	12.988	-3.342	59.837
166	4.022E+08	0.214	-0.038	5.457E+07	12.894	-4.500	65.516
167	4.140E+08	0.207	-0.039	7.148E+07	12.972	-3.409	79.988
168	3.890E+08	0.174	-0.032	6.163E+07	13.011	-3.625	82.202
169	4.144E+08	0.212	-0.043	1.085E+08	12.754	-2.263	81.043
170	3.860E+08	0.172	-0.031	5.468E+07	13.193	-3.936	90.865
171	3.629E+08	0.194	-0.031	3.420E+07	13.060	-5.886	77.348
172	3.900E+08	0.170	-0.030	6.462E+07	13.187	-3.465	80.310
173	3.173E+08	0.150	-0.026	4.656E+07	13.231	-4.088	100.463
174	3.406E+08	0.150	-0.027	6.299E+07	13.103	-3.208	95.096
175	3.085E+08	0.164	-0.025	4.045E+07	13.093	-4.691	96.608
176	3.311E+08	0.155	-0.026	6.779E+07	13.146	-3.022	89.083
177	4.770E+08	0.216	-0.033	4.691E+07	13.105	-3.917	94.717
178	4.735E+08	0.215	-0.034	5.590E+07	13.065	-3.272	110.494
179	3.629E+08	0.171	-0.027	7.757E+07	13.231	-2.744	125.092
180	4.169E+08	0.215	-0.027	2.872E+07	13.383	-5.443	134.261
181	3.414E+08	0.194	-0.026	4.177E+07	13.155	-4.287	102.490
182	5.018E+08	0.225	-0.034	7.737E+07	12.799	-2.820	85.050
183	3.191E+08	0.179	-0.025	6.451E+07	13.222	-3.294	98.289
184	2.910E+08	0.206	-0.023	1.275E+07	13.144	-8.410	136.296
185	4.159E+08	0.204	-0.029	7.214E+07	13.189	-2.951	96.091
186	2.905E+08	0.188	-0.024	2.821E+07	13.113	-5.049	136.534
187	5.515E+08	0.233	-0.034	5.536E+07	13.048	-3.170	113.513
188	3.188E+08	0.195	-0.025	4.118E+07	13.057	-4.288	114.096
189	3.794E+08	0.184	-0.028	1.278E+08	13.431	-2.041	106.888

Index	I_{young}	$t_{0,young}$	τ_{young}	I_{old}	$t_{0,old}$	τ_{old}	χ^2
190	5.514E+08	0.236	-0.034	4.785E+07	13.207	-3.556	118.680
191	3.981E+08	0.201	-0.029	6.275E+07	13.231	-3.178	102.902
192	4.080E+08	0.205	-0.028	6.733E+07	13.116	-3.068	104.848
193	3.812E+08	0.209	-0.026	3.911E+07	13.145	-4.274	103.953
194	4.150E+08	0.208	-0.029	5.619E+07	13.094	-3.366	97.650
195	4.974E+08	0.222	-0.033	6.199E+07	13.254	-2.945	106.235
196	2.904E+08	0.185	-0.025	5.236E+07	13.139	-3.834	98.248
197	5.599E+08	0.253	-0.033	3.812E+07	12.929	-4.719	124.517
198	2.836E+08	0.210	-0.024	2.349E+07	13.224	-6.669	117.024
199	3.536E+08	0.195	-0.029	5.766E+07	13.257	-3.668	106.423

Table B.1: Parameters obtained for the two burst fit with simuated annealing

Result of the mass for the different stellar categories

Index	M_{alive}	M_{WD}	M_{NS}	M_{BH}	M_T
0	1.111E+09	2.966E+08	3.397E+07	7.762E+07	1.519E+09
1	1.324E+09	3.502E+08	4.038E+07	9.224E+07	1.807E+09
2	1.156E+09	3.084E+08	3.534E+07	8.074E+07	1.580E+09
3	1.573E+09	4.200E+08	4.812E+07	1.099E+08	2.152E+09
4	1.619E+09	4.324E+08	4.953E+07	1.132E+08	2.214E+09
5	1.616E+09	4.315E+08	4.942E+07	1.129E+08	2.210E+09
6	1.420E+09	3.633E+08	4.287E+07	9.794E+07	1.924E+09
7	1.441E+09	3.618E+08	4.324E+07	9.878E+07	1.945E+09
8	1.512E+09	3.918E+08	4.580E+07	1.046E+08	2.055E+09
9	1.402E+09	3.496E+08	4.196E+07	9.586E+07	1.889E+09
10	1.287E+09	3.193E+08	3.844E+07	8.782E+07	1.732E+09
11	1.277E+09	3.151E+08	3.807E+07	8.698E+07	1.717E+09
12	1.304E+09	3.208E+08	3.884E+07	8.872E+07	1.752E+09
13	1.254E+09	3.074E+08	3.729E+07	8.520E+07	1.684E+09
14	1.184E+09	2.896E+08	3.518E+07	8.037E+07	1.589E+09
15	1.078E+09	2.609E+08	3.189E+07	7.286E+07	1.443E+09
16	1.138E+09	2.739E+08	3.360E+07	7.677E+07	1.522E+09
17	1.102E+09	2.659E+08	3.255E+07	7.437E+07	1.475E+09
18	1.020E+09	2.417E+08	2.994E+07	6.839E+07	1.360E+09
19	8.350E+08	1.919E+08	2.421E+07	5.531E+07	1.106E+09
20	1.032E+09	2.447E+08	3.027E+07	6.915E+07	1.377E+09
21	8.964E+08	2.042E+08	2.591E+07	5.920E+07	1.186E+09
22	7.759E+08	1.697E+08	2.210E+07	5.049E+07	1.018E+09
23	6.706E+08	1.386E+08	1.874E+07	4.281E+07	8.708E+08
24	6.050E+08	1.209E+08	1.669E+07	3.814E+07	7.808E+08

Index	M_{alive}	M_{WD}	M_{NS}	M_{BH}	M_T
25	4.803E+08	8.487E+07	1.273E+07	2.909E+07	6.070E+08
26	5.861E+08	1.162E+08	1.609E+07	3.677E+07	7.552E+08
27	3.282E+08	4.489E+07	8.055E+06	1.840E+07	3.995E+08
28	3.083E+08	3.998E+07	7.460E+06	1.704E+07	3.727E+08
29	3.109E+08	3.843E+07	7.437E+06	1.699E+07	3.737E+08
30	2.736E+08	2.767E+07	6.258E+06	1.430E+07	3.219E+08
31	3.487E+08	5.008E+07	8.658E+06	1.978E+07	4.272E+08
32	4.105E+08	6.773E+07	1.061E+07	2.425E+07	5.130E+08
33	2.734E+08	2.902E+07	6.304E+06	1.440E+07	3.231E+08
34	3.209E+08	4.308E+07	7.821E+06	1.787E+07	3.896E+08
35	2.621E+08	2.706E+07	6.014E+06	1.374E+07	3.089E+08
36	2.344E+08	2.033E+07	5.186E+06	1.185E+07	2.717E+08
37	2.362E+08	2.054E+07	5.231E+06	1.195E+07	2.739E+08
38	2.332E+08	1.964E+07	5.134E+06	1.173E+07	2.697E+08
39	3.723E+08	6.026E+07	9.548E+06	2.181E+07	4.639E+08
40	2.437E+08	2.360E+07	5.520E+06	1.261E+07	2.855E+08
41	3.001E+08	4.085E+07	7.339E+06	1.677E+07	3.650E+08
42	3.347E+08	5.094E+07	8.426E+06	1.925E+07	4.133E+08
43	3.684E+08	6.196E+07	9.549E+06	2.182E+07	4.618E+08
44	2.041E+08	1.563E+07	4.406E+06	1.007E+07	2.342E+08
45	1.848E+08	1.161E+07	3.867E+06	8.834E+06	2.091E+08
46	1.845E+08	9.400E+06	3.756E+06	8.580E+06	2.062E+08
47	1.919E+08	1.241E+07	4.032E+06	9.212E+06	2.175E+08
48	1.669E+08	5.786E+06	3.270E+06	7.470E+06	1.834E+08
49	1.747E+08	9.951E+06	3.608E+06	8.243E+06	1.965E+08
50	2.129E+08	1.857E+07	4.706E+06	1.075E+07	2.469E+08
51	1.641E+08	5.683E+06	3.216E+06	7.348E+06	1.803E+08
52	1.719E+08	8.672E+06	3.502E+06	8.000E+06	1.921E+08
53	1.997E+08	1.770E+07	4.432E+06	1.013E+07	2.320E+08
54	1.516E+08	5.311E+06	2.976E+06	6.800E+06	1.667E+08
55	1.720E+08	1.109E+07	3.618E+06	8.265E+06	1.950E+08
56	2.181E+08	2.590E+07	5.143E+06	1.175E+07	2.609E+08
57	2.590E+08	3.922E+07	6.506E+06	1.486E+07	3.196E+08
58	1.326E+08	4.489E+06	2.591E+06	5.920E+06	1.456E+08
59	1.970E+08	2.283E+07	4.615E+06	1.054E+07	2.350E+08
60	1.443E+08	8.434E+06	2.992E+06	6.837E+06	1.626E+08
61	2.052E+08	2.558E+07	4.914E+06	1.123E+07	2.470E+08
62	2.004E+08	2.586E+07	4.839E+06	1.106E+07	2.421E+08
63	1.809E+08	1.982E+07	4.200E+06	9.595E+06	2.145E+08
64	1.925E+08	2.393E+07	4.607E+06	1.052E+07	2.315E+08
65	2.451E+08	3.936E+07	6.294E+06	1.438E+07	3.051E+08

Index	M_{alive}	M_{WD}	M_{NS}	M_{BH}	M_T
66	2.111E+08	3.142E+07	5.302E+06	1.211E+07	2.599E+08
67	2.370E+08	3.824E+07	6.096E+06	1.393E+07	2.952E+08
68	2.303E+08	3.730E+07	5.924E+06	1.353E+07	2.870E+08
69	1.955E+08	2.750E+07	4.842E+06	1.106E+07	2.389E+08
70	2.091E+08	3.303E+07	5.345E+06	1.221E+07	2.596E+08
71	2.227E+08	3.689E+07	5.774E+06	1.319E+07	2.785E+08
72	2.017E+08	3.074E+07	5.107E+06	1.167E+07	2.492E+08
73	2.342E+08	4.014E+07	6.140E+06	1.403E+07	2.945E+08
74	2.169E+08	3.678E+07	5.663E+06	1.294E+07	2.723E+08
75	2.306E+08	4.111E+07	6.120E+06	1.398E+07	2.918E+08
76	1.739E+08	2.511E+07	4.335E+06	9.903E+06	2.132E+08
77	2.004E+08	3.243E+07	5.167E+06	1.180E+07	2.498E+08
78	2.277E+08	4.082E+07	6.054E+06	1.383E+07	2.884E+08
79	2.206E+08	4.019E+07	5.897E+06	1.347E+07	2.801E+08
80	2.317E+08	4.233E+07	6.198E+06	1.416E+07	2.943E+08
81	2.307E+08	4.287E+07	6.204E+06	1.417E+07	2.939E+08
82	2.145E+08	3.879E+07	5.720E+06	1.307E+07	2.720E+08
83	2.180E+08	4.080E+07	5.873E+06	1.342E+07	2.781E+08
84	2.145E+08	3.986E+07	5.768E+06	1.318E+07	2.733E+08
85	2.136E+08	3.927E+07	5.726E+06	1.308E+07	2.717E+08
86	2.022E+08	3.669E+07	5.395E+06	1.233E+07	2.566E+08
87	1.917E+08	3.464E+07	5.106E+06	1.167E+07	2.431E+08
88	1.796E+08	3.173E+07	4.749E+06	1.085E+07	2.269E+08
89	1.917E+08	3.411E+07	5.084E+06	1.162E+07	2.425E+08
90	1.873E+08	3.338E+07	4.968E+06	1.135E+07	2.370E+08
91	1.743E+08	3.033E+07	4.586E+06	1.048E+07	2.197E+08
92	1.681E+08	2.906E+07	4.421E+06	1.010E+07	2.117E+08
93	1.840E+08	3.301E+07	4.892E+06	1.118E+07	2.331E+08
94	1.946E+08	3.581E+07	5.216E+06	1.192E+07	2.475E+08
95	1.761E+08	3.136E+07	4.669E+06	1.067E+07	2.228E+08
96	1.854E+08	3.449E+07	4.988E+06	1.140E+07	2.363E+08
97	1.902E+08	3.563E+07	5.129E+06	1.172E+07	2.427E+08
98	1.945E+08	3.657E+07	5.252E+06	1.200E+07	2.483E+08
99	1.845E+08	3.410E+07	4.958E+06	1.133E+07	2.349E+08
100	1.901E+08	3.687E+07	5.180E+06	1.184E+07	2.440E+08
101	1.618E+08	2.947E+07	4.316E+06	9.861E+06	2.054E+08
102	1.825E+08	3.459E+07	4.936E+06	1.128E+07	2.333E+08
103	1.884E+08	3.654E+07	5.135E+06	1.173E+07	2.418E+08
104	1.738E+08	3.295E+07	4.699E+06	1.074E+07	2.221E+08
105	1.667E+08	3.192E+07	4.525E+06	1.034E+07	2.135E+08
106	1.648E+08	3.043E+07	4.419E+06	1.010E+07	2.097E+08

Index	M_{alive}	M_{WD}	M_{NS}	M_{BH}	M_T
107	1.609E+08	2.999E+07	4.326E+06	9.884E+06	2.051E+08
108	1.595E+08	2.962E+07	4.284E+06	9.787E+06	2.032E+08
109	1.553E+08	2.976E+07	4.215E+06	9.629E+06	1.989E+08
110	1.475E+08	2.636E+07	3.916E+06	8.948E+06	1.867E+08
111	1.527E+08	2.812E+07	4.095E+06	9.356E+06	1.943E+08
112	1.565E+08	2.944E+07	4.227E+06	9.657E+06	1.998E+08
113	1.542E+08	2.927E+07	4.178E+06	9.544E+06	1.972E+08
114	1.482E+08	2.784E+07	4.001E+06	9.141E+06	1.892E+08
115	1.555E+08	2.927E+07	4.206E+06	9.610E+06	1.986E+08
116	1.501E+08	2.836E+07	4.059E+06	9.274E+06	1.917E+08
117	1.559E+08	3.028E+07	4.257E+06	9.726E+06	2.001E+08
118	1.371E+08	2.577E+07	3.704E+06	8.461E+06	1.751E+08
119	1.319E+08	2.347E+07	3.504E+06	8.006E+06	1.669E+08
120	1.439E+08	2.717E+07	3.895E+06	8.899E+06	1.839E+08
121	1.420E+08	2.710E+07	3.857E+06	8.811E+06	1.818E+08
122	1.286E+08	2.389E+07	3.462E+06	7.910E+06	1.639E+08
123	1.377E+08	2.570E+07	3.717E+06	8.492E+06	1.756E+08
124	1.238E+08	2.247E+07	3.306E+06	7.554E+06	1.571E+08
125	1.355E+08	2.524E+07	3.658E+06	8.356E+06	1.728E+08
126	1.297E+08	2.454E+07	3.513E+06	8.025E+06	1.658E+08
127	1.235E+08	2.258E+07	3.308E+06	7.557E+06	1.569E+08
128	1.345E+08	2.569E+07	3.655E+06	8.351E+06	1.722E+08
129	1.364E+08	2.607E+07	3.709E+06	8.474E+06	1.746E+08
130	1.287E+08	2.408E+07	3.479E+06	7.948E+06	1.642E+08
131	1.159E+08	2.146E+07	3.116E+06	7.120E+06	1.476E+08
132	1.287E+08	2.461E+07	3.499E+06	7.994E+06	1.648E+08
133	1.164E+08	2.082E+07	3.105E+06	7.093E+06	1.474E+08
134	1.316E+08	2.546E+07	3.597E+06	8.218E+06	1.689E+08
135	1.192E+08	2.303E+07	3.251E+06	7.427E+06	1.529E+08
136	1.182E+08	2.156E+07	3.171E+06	7.244E+06	1.501E+08
137	1.286E+08	2.490E+07	3.515E+06	8.031E+06	1.651E+08
138	1.161E+08	2.154E+07	3.131E+06	7.154E+06	1.479E+08
139	1.087E+08	2.044E+07	2.940E+06	6.716E+06	1.388E+08
140	1.091E+08	1.974E+07	2.919E+06	6.668E+06	1.384E+08
141	1.150E+08	2.166E+07	3.113E+06	7.111E+06	1.468E+08
142	1.223E+08	2.398E+07	3.353E+06	7.661E+06	1.573E+08
143	1.102E+08	2.045E+07	2.972E+06	6.791E+06	1.404E+08
144	1.133E+08	2.187E+07	3.090E+06	7.059E+06	1.453E+08
145	1.138E+08	2.174E+07	3.093E+06	7.066E+06	1.457E+08
146	1.083E+08	2.040E+07	2.930E+06	6.695E+06	1.383E+08
147	1.057E+08	1.980E+07	2.855E+06	6.523E+06	1.349E+08

Index	M_{alive}	M_{WD}	M_{NS}	M_{BH}	M_T
148	1.185E+08	2.361E+07	3.267E+06	7.463E+06	1.529E+08
149	1.235E+08	2.466E+07	3.407E+06	7.783E+06	1.594E+08
150	1.063E+08	1.961E+07	2.862E+06	6.539E+06	1.353E+08
151	1.013E+08	1.855E+07	2.721E+06	6.216E+06	1.288E+08
152	9.218E+07	1.646E+07	2.456E+06	5.612E+06	1.167E+08
153	1.140E+08	2.188E+07	3.110E+06	7.106E+06	1.461E+08
154	1.164E+08	2.258E+07	3.185E+06	7.278E+06	1.494E+08
155	1.088E+08	2.078E+07	2.960E+06	6.763E+06	1.393E+08
156	1.122E+08	2.203E+07	3.081E+06	7.040E+06	1.444E+08
157	1.236E+08	2.525E+07	3.439E+06	7.856E+06	1.602E+08
158	1.239E+08	2.449E+07	3.417E+06	7.806E+06	1.596E+08
159	1.185E+08	2.287E+07	3.243E+06	7.410E+06	1.520E+08
160	1.153E+08	2.259E+07	3.168E+06	7.238E+06	1.483E+08
161	1.208E+08	2.471E+07	3.362E+06	7.681E+06	1.565E+08
162	1.233E+08	2.489E+07	3.418E+06	7.808E+06	1.594E+08
163	1.280E+08	2.631E+07	3.572E+06	8.162E+06	1.660E+08
164	1.314E+08	2.749E+07	3.689E+06	8.427E+06	1.710E+08
165	1.267E+08	2.665E+07	3.562E+06	8.139E+06	1.651E+08
166	1.373E+08	2.903E+07	3.867E+06	8.834E+06	1.790E+08
167	1.231E+08	2.520E+07	3.430E+06	7.837E+06	1.596E+08
168	1.224E+08	2.534E+07	3.421E+06	7.815E+06	1.590E+08
169	1.100E+08	2.199E+07	3.043E+06	6.952E+06	1.420E+08
170	1.237E+08	2.562E+07	3.457E+06	7.898E+06	1.607E+08
171	1.268E+08	2.624E+07	3.545E+06	8.098E+06	1.646E+08
172	1.229E+08	2.528E+07	3.426E+06	7.827E+06	1.594E+08
173	1.104E+08	2.202E+07	3.046E+06	6.959E+06	1.424E+08
174	1.146E+08	2.311E+07	3.175E+06	7.253E+06	1.481E+08
175	1.129E+08	2.198E+07	3.094E+06	7.068E+06	1.451E+08
176	1.090E+08	2.150E+07	2.993E+06	6.837E+06	1.403E+08
177	1.188E+08	2.458E+07	3.313E+06	7.569E+06	1.542E+08
178	1.146E+08	2.328E+07	3.178E+06	7.261E+06	1.483E+08
179	1.163E+08	2.326E+07	3.210E+06	7.334E+06	1.501E+08
180	1.263E+08	2.647E+07	3.538E+06	8.084E+06	1.644E+08
181	1.057E+08	2.001E+07	2.870E+06	6.557E+06	1.352E+08
182	1.120E+08	2.256E+07	3.098E+06	7.079E+06	1.447E+08
183	1.226E+08	2.477E+07	3.397E+06	7.762E+06	1.585E+08
184	1.140E+08	2.248E+07	3.133E+06	7.157E+06	1.467E+08
185	1.123E+08	2.227E+07	3.091E+06	7.062E+06	1.447E+08
186	1.053E+08	2.042E+07	2.879E+06	6.577E+06	1.352E+08
187	1.140E+08	2.280E+07	3.148E+06	7.191E+06	1.471E+08
188	1.216E+08	2.474E+07	3.378E+06	7.717E+06	1.575E+08

Index	M_{alive}	M_{WD}	M_{NS}	M_{BH}	M_T
189	1.107E+08	2.184E+07	3.041E+06	6.948E+06	1.425E+08
190	1.110E+08	2.201E+07	3.056E+06	6.982E+06	1.430E+08
191	1.119E+08	2.242E+07	3.091E+06	7.062E+06	1.444E+08
192	1.208E+08	2.448E+07	3.349E+06	7.651E+06	1.562E+08
193	1.123E+08	2.208E+07	3.083E+06	7.044E+06	1.445E+08
194	1.148E+08	2.290E+07	3.167E+06	7.235E+06	1.481E+08
195	1.057E+08	2.080E+07	2.903E+06	6.632E+06	1.361E+08
196	1.246E+08	2.531E+07	3.460E+06	7.905E+06	1.612E+08
197	1.300E+08	2.694E+07	3.634E+06	8.301E+06	1.688E+08
198	1.326E+08	2.760E+07	3.713E+06	8.483E+06	1.723E+08
199	1.149E+08	2.321E+07	3.185E+06	7.277E+06	1.485E+08

Table B.2: Result of the mass for the different stellar categories

Result of the masses in the galaxy NGC 7331

Index	M_{HI}	M_{H2}	M_{He}	M_{bulge}	M_{disk}	M_{total}
0	6.685E+04	2.880E+05	1.215E+05	1.519E+09	0.000E+00	1.519E+09
1	1.152E+05	4.897E+05	2.072E+05	1.848E+09	1.646E-28	1.849E+09
2	1.632E+05	6.887E+05	2.917E+05	1.583E+09	2.034E-10	1.584E+09
3	2.109E+05	8.896E+05	3.769E+05	2.152E+09	4.926E-30	2.153E+09
4	2.585E+05	1.097E+06	4.643E+05	2.215E+09	3.876E+04	2.217E+09
5	3.063E+05	1.316E+06	5.556E+05	2.208E+09	3.108E+05	2.210E+09
6	3.544E+05	1.551E+06	6.524E+05	1.913E+09	1.230E+06	1.917E+09
7	4.029E+05	1.805E+06	7.561E+05	2.002E+09	3.565E+06	2.008E+09
8	4.520E+05	2.083E+06	8.682E+05	2.123E+09	1.188E+07	2.138E+09
9	5.018E+05	2.389E+06	9.901E+05	2.034E+09	2.051E+07	2.059E+09
10	5.525E+05	2.727E+06	1.123E+06	1.708E+09	1.799E+07	1.730E+09
11	6.042E+05	3.100E+06	1.269E+06	1.816E+09	3.193E+07	1.853E+09
12	6.570E+05	3.512E+06	1.428E+06	1.781E+09	4.555E+07	1.832E+09
13	7.109E+05	3.966E+06	1.602E+06	1.842E+09	3.672E+07	1.885E+09
14	7.662E+05	4.466E+06	1.792E+06	1.665E+09	4.580E+07	1.718E+09
15	8.229E+05	5.013E+06	1.999E+06	1.390E+09	5.359E+07	1.451E+09
16	8.810E+05	5.612E+06	2.224E+06	1.459E+09	6.335E+07	1.531E+09
17	9.407E+05	6.265E+06	2.468E+06	1.337E+09	7.755E+07	1.424E+09
18	1.002E+06	6.963E+06	2.728E+06	1.279E+09	8.138E+07	1.371E+09
19	1.065E+06	7.697E+06	3.001E+06	1.133E+09	9.216E+07	1.237E+09
20	1.130E+06	8.450E+06	3.281E+06	1.173E+09	1.024E+08	1.288E+09
21	1.196E+06	9.206E+06	3.562E+06	1.152E+09	1.085E+08	1.275E+09
22	1.264E+06	9.944E+06	3.838E+06	8.655E+08	1.386E+08	1.019E+09
23	1.334E+06	1.064E+07	4.101E+06	7.129E+08	1.520E+08	8.809E+08

Index	M_{HI}	M_{H2}	M_{He}	M_{bulge}	M_{disk}	M_{total}
24	1.406E+06	1.128E+07	4.343E+06	5.800E+08	1.674E+08	7.644E+08
25	1.480E+06	1.184E+07	4.562E+06	4.175E+08	1.890E+08	6.245E+08
26	1.555E+06	1.234E+07	4.759E+06	5.678E+08	1.756E+08	7.620E+08
27	1.633E+06	1.277E+07	4.934E+06	1.940E+08	2.051E+08	4.184E+08
28	1.712E+06	1.315E+07	5.089E+06	1.613E+08	2.033E+08	3.845E+08
29	1.793E+06	1.347E+07	5.227E+06	1.582E+08	2.144E+08	3.931E+08
30	1.875E+06	1.375E+07	5.351E+06	1.038E+08	2.172E+08	3.420E+08
31	1.960E+06	1.399E+07	5.463E+06	2.252E+08	2.020E+08	4.486E+08
32	2.045E+06	1.421E+07	5.566E+06	2.977E+08	1.899E+08	5.094E+08
33	2.133E+06	1.439E+07	5.659E+06	1.072E+08	2.105E+08	3.399E+08
34	2.222E+06	1.455E+07	5.745E+06	1.874E+08	2.009E+08	4.108E+08
35	2.313E+06	1.470E+07	5.825E+06	9.517E+07	2.018E+08	3.198E+08
36	2.404E+06	1.482E+07	5.900E+06	6.706E+07	2.019E+08	2.921E+08
37	2.498E+06	1.495E+07	5.973E+06	0.000E+00	2.093E+08	2.328E+08
38	2.592E+06	1.506E+07	6.046E+06	0.000E+00	2.093E+08	2.330E+08
39	2.687E+06	1.518E+07	6.118E+06	0.000E+00	5.034E+08	5.274E+08
40	2.783E+06	1.528E+07	6.185E+06	0.000E+00	1.971E+08	2.214E+08
41	2.881E+06	1.535E+07	6.245E+06	0.000E+00	1.943E+08	2.188E+08
42	2.979E+06	1.539E+07	6.292E+06	0.000E+00	1.958E+08	2.204E+08
43	3.077E+06	1.539E+07	6.323E+06	0.000E+00	1.905E+08	2.153E+08
44	3.177E+06	1.532E+07	6.333E+06	0.000E+00	1.867E+08	2.115E+08
45	3.277E+06	1.517E+07	6.317E+06	0.000E+00	1.795E+08	2.043E+08
46	3.378E+06	1.494E+07	6.275E+06	0.000E+00	1.890E+08	2.136E+08
47	3.480E+06	1.465E+07	6.208E+06	0.000E+00	1.843E+08	2.086E+08
48	3.582E+06	1.429E+07	6.120E+06	0.000E+00	1.826E+08	2.066E+08
49	3.684E+06	1.388E+07	6.014E+06	0.000E+00	1.739E+08	1.974E+08
50	3.787E+06	1.342E+07	5.893E+06	0.000E+00	1.838E+08	2.069E+08
51	3.891E+06	1.293E+07	5.761E+06	0.000E+00	1.802E+08	2.028E+08
52	3.995E+06	1.242E+07	5.622E+06	0.000E+00	1.769E+08	1.989E+08
53	4.099E+06	1.189E+07	5.477E+06	0.000E+00	1.709E+08	1.923E+08
54	4.203E+06	1.135E+07	5.327E+06	0.000E+00	1.667E+08	1.876E+08
55	4.308E+06	1.080E+07	5.173E+06	0.000E+00	1.660E+08	1.863E+08
56	4.413E+06	1.024E+07	5.018E+06	0.000E+00	1.901E+08	2.098E+08
57	4.517E+06	9.680E+06	4.862E+06	0.000E+00	1.540E+08	1.730E+08
58	4.622E+06	9.123E+06	4.707E+06	0.000E+00	1.456E+08	1.640E+08
59	4.727E+06	8.573E+06	4.555E+06	0.000E+00	1.464E+08	1.642E+08
60	4.832E+06	8.041E+06	4.408E+06	0.000E+00	1.416E+08	1.588E+08
61	4.937E+06	7.534E+06	4.271E+06	0.000E+00	1.426E+08	1.593E+08
62	5.041E+06	7.064E+06	4.146E+06	0.000E+00	1.715E+08	1.878E+08
63	5.145E+06	6.641E+06	4.037E+06	0.000E+00	2.084E+08	2.242E+08
64	5.249E+06	6.278E+06	3.948E+06	0.000E+00	2.325E+08	2.479E+08

Index	M_{HI}	M_{H2}	M_{He}	M_{bulge}	M_{disk}	M_{total}
65	5.353E+06	5.986E+06	3.883E+06	0.000E+00	2.102E+08	2.254E+08
66	5.456E+06	5.776E+06	3.847E+06	0.000E+00	1.773E+08	1.924E+08
67	5.559E+06	5.641E+06	3.835E+06	0.000E+00	2.697E+08	2.848E+08
68	5.661E+06	5.566E+06	3.845E+06	0.000E+00	3.069E+08	3.219E+08
69	5.762E+06	5.537E+06	3.870E+06	0.000E+00	2.344E+08	2.496E+08
70	5.863E+06	5.536E+06	3.904E+06	0.000E+00	1.592E+08	1.745E+08
71	5.963E+06	5.546E+06	3.942E+06	0.000E+00	2.297E+08	2.451E+08
72	6.062E+06	5.549E+06	3.976E+06	0.000E+00	2.508E+08	2.664E+08
73	6.160E+06	5.526E+06	4.002E+06	0.000E+00	2.765E+08	2.922E+08
74	6.258E+06	5.476E+06	4.018E+06	0.000E+00	2.571E+08	2.728E+08
75	6.354E+06	5.402E+06	4.026E+06	0.000E+00	2.376E+08	2.534E+08
76	6.449E+06	5.307E+06	4.026E+06	0.000E+00	3.009E+08	3.167E+08
77	6.543E+06	5.194E+06	4.020E+06	0.000E+00	2.290E+08	2.448E+08
78	6.635E+06	5.068E+06	4.008E+06	0.000E+00	3.174E+08	3.331E+08
79	6.726E+06	4.932E+06	3.993E+06	0.000E+00	2.363E+08	2.520E+08
80	6.816E+06	4.790E+06	3.975E+06	0.000E+00	2.383E+08	2.538E+08
81	6.904E+06	4.643E+06	3.955E+06	0.000E+00	3.066E+08	3.221E+08
82	6.991E+06	4.494E+06	3.933E+06	0.000E+00	1.869E+08	2.024E+08
83	7.076E+06	4.345E+06	3.911E+06	0.000E+00	2.335E+08	2.489E+08
84	7.160E+06	4.196E+06	3.889E+06	0.000E+00	1.972E+08	2.124E+08
85	7.243E+06	4.050E+06	3.867E+06	0.000E+00	2.703E+08	2.855E+08
86	7.325E+06	3.908E+06	3.847E+06	0.000E+00	2.671E+08	2.822E+08
87	7.406E+06	3.773E+06	3.829E+06	0.000E+00	2.370E+08	2.520E+08
88	7.487E+06	3.645E+06	3.812E+06	0.000E+00	2.245E+08	2.394E+08
89	7.567E+06	3.521E+06	3.797E+06	0.000E+00	2.444E+08	2.593E+08
90	7.647E+06	3.400E+06	3.783E+06	0.000E+00	1.954E+08	2.103E+08
91	7.728E+06	3.279E+06	3.769E+06	0.000E+00	2.286E+08	2.434E+08
92	7.808E+06	3.157E+06	3.755E+06	0.000E+00	2.001E+08	2.148E+08
93	7.889E+06	3.032E+06	3.740E+06	0.000E+00	2.394E+08	2.541E+08
94	7.971E+06	2.901E+06	3.723E+06	0.000E+00	2.473E+08	2.619E+08
95	8.054E+06	2.762E+06	3.704E+06	0.000E+00	2.128E+08	2.273E+08
96	8.138E+06	2.619E+06	3.684E+06	0.000E+00	2.217E+08	2.361E+08
97	8.224E+06	2.474E+06	3.663E+06	0.000E+00	2.399E+08	2.542E+08
98	8.311E+06	2.328E+06	3.644E+06	0.000E+00	2.225E+08	2.368E+08
99	8.401E+06	2.187E+06	3.626E+06	0.000E+00	2.285E+08	2.427E+08
100	8.493E+06	2.051E+06	3.611E+06	0.000E+00	2.461E+08	2.603E+08
101	8.588E+06	1.925E+06	3.600E+06	0.000E+00	1.138E+08	1.279E+08
102	8.686E+06	1.812E+06	3.595E+06	0.000E+00	2.263E+08	2.404E+08
103	8.786E+06	1.714E+06	3.596E+06	0.000E+00	2.326E+08	2.467E+08
104	8.886E+06	1.636E+06	3.604E+06	0.000E+00	2.245E+08	2.386E+08
105	8.988E+06	1.581E+06	3.619E+06	0.000E+00	1.896E+08	2.038E+08

Index	M_{HI}	M_{H2}	M_{He}	M_{bulge}	M_{disk}	M_{total}
106	9.090E+06	1.552E+06	3.645E+06	0.000E+00	2.013E+08	2.155E+08
107	9.191E+06	1.554E+06	3.680E+06	0.000E+00	1.800E+08	1.944E+08
108	9.291E+06	1.590E+06	3.726E+06	0.000E+00	1.868E+08	2.014E+08
109	9.389E+06	0.000E+00	3.216E+06	0.000E+00	1.916E+08	2.042E+08
110	9.485E+06	0.000E+00	3.248E+06	0.000E+00	1.880E+08	2.007E+08
111	9.577E+06	0.000E+00	3.280E+06	0.000E+00	2.323E+08	2.452E+08
112	9.665E+06	0.000E+00	3.310E+06	0.000E+00	1.854E+08	1.984E+08
113	9.748E+06	0.000E+00	3.338E+06	0.000E+00	1.377E+08	1.508E+08
114	9.825E+06	0.000E+00	3.365E+06	0.000E+00	1.923E+08	2.055E+08
115	9.896E+06	0.000E+00	3.389E+06	0.000E+00	1.893E+08	2.026E+08
116	9.958E+06	0.000E+00	3.410E+06	0.000E+00	1.456E+08	1.590E+08
117	1.001E+07	0.000E+00	3.429E+06	0.000E+00	1.352E+08	1.486E+08
118	1.006E+07	0.000E+00	3.445E+06	0.000E+00	1.476E+08	1.611E+08
119	1.009E+07	0.000E+00	3.456E+06	0.000E+00	1.774E+08	1.909E+08
120	1.012E+07	0.000E+00	3.465E+06	0.000E+00	1.520E+08	1.655E+08
121	1.013E+07	0.000E+00	3.468E+06	0.000E+00	1.861E+08	1.997E+08
122	1.013E+07	0.000E+00	3.468E+06	0.000E+00	1.554E+08	1.689E+08
123	1.011E+07	0.000E+00	3.462E+06	0.000E+00	1.587E+08	1.723E+08
124	1.008E+07	0.000E+00	3.452E+06	0.000E+00	1.600E+08	1.736E+08
125	1.004E+07	0.000E+00	3.438E+06	0.000E+00	1.645E+08	1.780E+08
126	9.985E+06	0.000E+00	3.419E+06	0.000E+00	1.671E+08	1.805E+08
127	9.920E+06	0.000E+00	3.397E+06	0.000E+00	1.641E+08	1.774E+08
128	9.846E+06	0.000E+00	3.372E+06	0.000E+00	7.752E+07	9.073E+07
129	9.764E+06	0.000E+00	3.344E+06	0.000E+00	1.713E+08	1.844E+08
130	9.674E+06	0.000E+00	3.313E+06	0.000E+00	1.614E+08	1.743E+08
131	9.577E+06	0.000E+00	3.280E+06	0.000E+00	1.807E+08	1.936E+08
132	9.475E+06	0.000E+00	3.245E+06	0.000E+00	1.594E+08	1.721E+08
133	9.369E+06	0.000E+00	3.208E+06	0.000E+00	1.598E+08	1.723E+08
134	9.260E+06	0.000E+00	3.171E+06	0.000E+00	1.676E+08	1.801E+08
135	9.149E+06	0.000E+00	3.133E+06	0.000E+00	1.617E+08	1.740E+08
136	9.038E+06	0.000E+00	3.095E+06	0.000E+00	1.549E+08	1.670E+08
137	8.928E+06	0.000E+00	3.058E+06	0.000E+00	1.130E+08	1.249E+08
138	8.821E+06	0.000E+00	3.021E+06	0.000E+00	1.421E+08	1.540E+08
139	8.717E+06	0.000E+00	2.985E+06	0.000E+00	1.403E+08	1.520E+08
140	8.619E+06	0.000E+00	2.952E+06	0.000E+00	1.256E+08	1.372E+08
141	8.527E+06	0.000E+00	2.920E+06	0.000E+00	1.777E+08	1.892E+08
142	8.443E+06	0.000E+00	2.892E+06	0.000E+00	1.235E+08	1.349E+08
143	8.370E+06	0.000E+00	2.866E+06	0.000E+00	1.414E+08	1.526E+08
144	8.305E+06	0.000E+00	2.844E+06	0.000E+00	1.436E+08	1.547E+08
145	8.251E+06	0.000E+00	2.826E+06	0.000E+00	1.551E+08	1.661E+08
146	8.205E+06	0.000E+00	2.810E+06	0.000E+00	1.312E+08	1.422E+08

Index	M_{HI}	M_{H2}	M_{He}	M_{bulge}	M_{disk}	M_{total}
147	8.168E+06	0.000E+00	2.797E+06	0.000E+00	1.422E+08	1.532E+08
148	8.139E+06	0.000E+00	2.787E+06	0.000E+00	1.532E+08	1.642E+08
149	8.118E+06	0.000E+00	2.780E+06	0.000E+00	1.626E+08	1.735E+08
150	8.104E+06	0.000E+00	2.775E+06	0.000E+00	1.409E+08	1.517E+08
151	8.097E+06	0.000E+00	2.773E+06	0.000E+00	1.360E+08	1.468E+08
152	8.096E+06	0.000E+00	2.773E+06	0.000E+00	8.491E+07	9.577E+07
153	8.101E+06	0.000E+00	2.774E+06	0.000E+00	1.511E+08	1.620E+08
154	8.111E+06	0.000E+00	2.778E+06	0.000E+00	9.552E+07	1.064E+08
155	8.125E+06	0.000E+00	2.783E+06	0.000E+00	1.333E+08	1.442E+08
156	8.144E+06	0.000E+00	2.789E+06	0.000E+00	1.449E+08	1.558E+08
157	8.167E+06	0.000E+00	2.797E+06	0.000E+00	1.624E+08	1.733E+08
158	8.192E+06	0.000E+00	2.805E+06	0.000E+00	1.153E+08	1.263E+08
159	8.219E+06	0.000E+00	2.815E+06	0.000E+00	1.175E+08	1.285E+08
160	8.248E+06	0.000E+00	2.825E+06	0.000E+00	1.744E+08	1.854E+08
161	8.278E+06	0.000E+00	2.835E+06	0.000E+00	1.226E+08	1.337E+08
162	8.309E+06	0.000E+00	2.845E+06	0.000E+00	8.478E+07	9.593E+07
163	8.339E+06	0.000E+00	2.856E+06	0.000E+00	1.385E+08	1.497E+08
164	8.368E+06	0.000E+00	2.866E+06	0.000E+00	1.639E+08	1.751E+08
165	8.396E+06	0.000E+00	2.875E+06	0.000E+00	1.520E+08	1.632E+08
166	8.422E+06	0.000E+00	2.884E+06	0.000E+00	1.445E+08	1.558E+08
167	8.446E+06	0.000E+00	2.892E+06	0.000E+00	1.502E+08	1.616E+08
168	8.468E+06	0.000E+00	2.900E+06	0.000E+00	1.529E+08	1.643E+08
169	8.488E+06	0.000E+00	2.907E+06	0.000E+00	1.475E+08	1.589E+08
170	8.505E+06	0.000E+00	2.912E+06	0.000E+00	1.525E+08	1.639E+08
171	8.518E+06	0.000E+00	2.917E+06	0.000E+00	1.347E+08	1.462E+08
172	8.529E+06	0.000E+00	2.921E+06	0.000E+00	1.613E+08	1.727E+08
173	8.536E+06	0.000E+00	2.923E+06	0.000E+00	1.367E+08	1.482E+08
174	8.539E+06	0.000E+00	2.924E+06	0.000E+00	1.527E+08	1.642E+08
175	8.538E+06	0.000E+00	2.924E+06	0.000E+00	1.380E+08	1.495E+08
176	8.532E+06	0.000E+00	2.922E+06	0.000E+00	1.563E+08	1.678E+08
177	8.522E+06	0.000E+00	2.918E+06	0.000E+00	1.391E+08	1.505E+08
178	8.506E+06	0.000E+00	2.913E+06	0.000E+00	1.424E+08	1.538E+08
179	8.485E+06	0.000E+00	2.906E+06	0.000E+00	1.601E+08	1.715E+08
180	8.458E+06	0.000E+00	2.897E+06	0.000E+00	1.129E+08	1.243E+08
181	8.425E+06	0.000E+00	2.885E+06	0.000E+00	1.341E+08	1.454E+08
182	8.386E+06	0.000E+00	2.872E+06	0.000E+00	1.369E+08	1.482E+08
183	8.339E+06	0.000E+00	2.856E+06	0.000E+00	1.575E+08	1.687E+08
184	8.285E+06	0.000E+00	2.837E+06	0.000E+00	8.394E+07	9.506E+07
185	8.224E+06	0.000E+00	2.816E+06	0.000E+00	1.605E+08	1.715E+08
186	8.155E+06	0.000E+00	2.793E+06	0.000E+00	1.102E+08	1.212E+08
187	8.078E+06	0.000E+00	2.766E+06	0.000E+00	1.390E+08	1.498E+08

Index	M_{HI}	M_{H2}	M_{He}	M_{bulge}	M_{disk}	M_{total}
188	7.994E+06	0.000E+00	2.738E+06	0.000E+00	1.338E+08	1.445E+08
189	7.904E+06	0.000E+00	2.707E+06	0.000E+00	1.796E+08	1.902E+08
190	7.809E+06	0.000E+00	2.674E+06	0.000E+00	1.308E+08	1.413E+08
191	7.710E+06	0.000E+00	2.640E+06	0.000E+00	1.480E+08	1.584E+08
192	7.608E+06	0.000E+00	2.605E+06	0.000E+00	1.592E+08	1.694E+08
193	7.504E+06	0.000E+00	2.570E+06	0.000E+00	1.279E+08	1.379E+08
194	7.398E+06	0.000E+00	2.534E+06	0.000E+00	1.466E+08	1.565E+08
195	7.292E+06	0.000E+00	2.497E+06	0.000E+00	1.387E+08	1.485E+08
196	7.187E+06	0.000E+00	2.461E+06	0.000E+00	1.498E+08	1.594E+08
197	7.084E+06	0.000E+00	2.426E+06	0.000E+00	1.166E+08	1.261E+08
198	6.985E+06	0.000E+00	2.392E+06	0.000E+00	1.103E+08	1.197E+08
199	6.889E+06	0.000E+00	2.359E+06	0.000E+00	1.497E+08	1.590E+08
Total	1.260E+09	7.832E+08	6.998E+08	4.207E+10	3.256E+10	7.738E+10

Table B.3: Result of the masses in the galaxy NGC 7331

Appendix C

Tables of velocities

Result of the rotation velocities in the galaxy NGC 7331

Ring index	V_{bulge}	V_{disk}	V_{total} bulge not rotating	V_{total} bulge rot. like disk
0	185.23	42.55	0.08	190.06
1	211.42	34.74	0.15	214.26
2	236.70	28.85	0.16	238.45
3	252.28	23.23	0.21	253.34
4	262.33	16.38	0.30	262.84
5	266.14	0.00	0.53	266.12
6	269.87	0.00	0.88	269.26
7	273.80	0.00	1.95	272.76
8	276.26	0.00	3.26	275.11
9	276.00	0.00	3.55	274.49
10	276.48	0.00	5.47	274.58
11	276.67	0.00	7.68	275.05
12	277.18	0.00	6.28	275.50
13	276.71	0.00	8.44	274.53
14	274.96	0.00	11.53	272.48
15	273.72	0.00	12.76	270.97
16	272.08	0.00	16.49	269.35
17	270.36	0.00	17.97	267.63
18	268.21	0.00	22.29	265.33
19	266.40	0.00	23.58	263.48
20	264.67	0.00	25.11	261.39
21	262.05	0.00	39.03	258.84
22	259.10	0.00	48.95	256.60
23	255.90	0.00	61.30	254.10
24	252.38	0.00	83.49	251.95
25	249.55	13.61	63.69	249.92

Ring index	V_{bulge}	V_{disk}	V_{total} bulge not rotating	V_{total} bulge rot. like disk
26	245.72	23.58	132.41	246.85
27	241.99	34.97	141.94	244.51
28	238.45	42.25	144.70	242.17
29	234.93	50.56	167.36	240.31
30	231.93	55.23	118.73	238.41
31	229.28	54.22	97.93	235.60
32	226.22	55.20	159.43	232.86
33	223.52	57.81	125.56	230.87
34	220.68	57.57	160.19	228.07
35	217.89	56.12	173.34	225.00
36	215.03	52.51	221.35	221.35
37	212.28	33.55	214.92	214.92
38	209.63	75.28	222.74	222.74
39	207.08	100.11	230.01	230.01
40	204.63	89.25	223.24	223.24
41	202.25	86.11	219.82	219.82
42	199.96	85.14	217.33	217.33
43	197.74	84.49	215.04	215.04
44	195.60	83.15	212.54	212.54
45	193.52	82.71	210.46	210.46
46	191.51	83.38	208.87	208.87
47	189.56	83.65	207.20	207.20
48	187.67	82.95	205.19	205.19
49	185.83	82.72	203.41	203.41
50	184.05	83.64	202.16	202.16
51	182.32	83.97	200.73	200.73
52	180.63	83.79	199.12	199.12
53	178.99	82.84	197.24	197.24
54	177.40	81.19	195.10	195.10
55	175.85	83.35	194.60	194.60
56	174.33	84.79	193.86	193.86
57	172.86	81.33	191.04	191.04
58	171.42	78.07	188.36	188.36
59	170.02	74.24	185.52	185.52
60	168.65	67.95	181.82	181.82
61	167.31	62.45	178.59	178.59
62	166.01	63.12	177.61	177.61
63	164.73	69.77	178.90	178.90
64	163.49	74.15	179.52	179.52
65	162.27	66.14	175.23	175.23

Ring index	V_{bulge}	V_{disk}	V_{total} bulge not rotating	V_{total} bulge rot. like disk
66	161.08	63.86	173.28	173.28
67	159.91	80.68	179.11	179.11
68	158.77	90.34	182.67	182.67
69	157.66	81.29	177.38	177.38
70	156.56	71.88	172.27	172.27
71	155.49	74.63	172.48	172.48
72	154.44	80.31	174.07	174.07
73	153.42	85.13	175.45	175.45
74	152.41	82.68	173.39	173.39
75	151.42	87.01	174.64	174.64
76	150.45	88.36	174.48	174.48
77	149.50	91.77	175.42	175.42
78	148.57	97.53	177.72	177.72
79	147.65	92.20	174.07	174.07
80	146.75	99.40	177.25	177.25
81	145.87	101.22	177.55	177.55
82	145.00	95.65	173.71	173.71
83	144.15	92.16	171.09	171.09
84	143.31	91.18	169.86	169.86
85	142.49	98.86	173.43	173.43
86	141.68	101.57	174.33	174.33
87	140.89	100.08	172.81	172.81
88	140.10	101.82	173.19	173.19
89	139.34	100.86	172.01	172.01
90	138.58	98.94	170.28	170.28
91	137.83	97.73	168.97	168.97
92	137.10	96.40	167.60	167.60
93	136.38	101.33	169.91	169.91
94	135.67	102.30	169.92	169.92
95	134.97	100.12	168.06	168.06
96	134.29	102.17	168.74	168.74
97	133.61	104.02	169.33	169.33
98	132.94	104.30	168.97	168.97
99	132.28	111.37	172.92	172.92
100	131.64	105.16	168.48	168.48
101	131.00	95.88	162.34	162.34
102	130.37	102.99	166.14	166.14
103	129.75	107.63	168.58	168.58
104	129.14	107.72	168.17	168.17
105	128.53	106.88	167.16	167.16

Ring index	V_{bulge}	V_{disk}	V_{total} bulge not rotating	V_{total} bulge rot. like disk
106	127.94	106.45	166.43	166.43
107	127.35	104.59	164.80	164.80
108	126.78	104.63	164.37	164.37
109	126.20	103.11	162.97	162.97
110	125.64	107.28	165.21	165.21
111	125.09	112.97	168.55	168.55
112	124.54	107.24	164.35	164.35
113	124.00	104.17	161.95	161.95
114	123.46	109.86	165.26	165.26
115	122.94	110.24	165.12	165.12
116	122.42	105.26	161.45	161.45
117	121.90	101.05	158.34	158.34
118	121.39	102.51	158.89	158.89
119	120.89	102.63	158.58	158.58
120	120.40	103.63	158.86	158.86
121	119.91	105.70	159.85	159.85
122	119.43	103.85	158.26	158.26
123	118.95	103.59	157.73	157.73
124	118.48	103.80	157.51	157.51
125	118.01	105.37	158.21	158.21
126	117.55	110.18	161.11	161.11
127	117.10	102.32	155.50	155.50
128	116.65	95.01	150.44	150.44
129	116.20	99.74	153.14	153.14
130	115.76	102.30	154.48	154.48
131	115.33	104.51	155.64	155.64
132	114.90	103.32	154.52	154.52
133	114.47	104.44	154.96	154.96
134	114.05	106.54	156.07	156.07
135	113.63	109.02	157.48	157.48
136	113.22	105.81	154.97	154.97
137	112.82	101.82	151.97	151.97
138	112.41	103.34	152.69	152.69
139	112.02	99.61	149.90	149.90
140	111.62	102.63	151.63	151.63
141	111.23	105.16	153.07	153.07
142	110.85	101.05	149.99	149.99
143	110.46	101.12	149.76	149.76
144	110.09	103.30	150.96	150.96
145	109.71	103.22	150.63	150.63

Ring index	V_{bulge}	V_{disk}	V_{total} bulge not rotating	V_{total} bulge rot. like disk
146	109.34	100.47	148.49	148.49
147	108.97	101.00	148.58	148.58
148	108.61	104.75	150.90	150.90
149	108.25	107.22	152.36	152.36
150	107.90	108.82	153.25	153.25
151	107.54	102.48	148.55	148.55
152	107.19	101.02	147.29	147.29
153	106.85	101.56	147.42	147.42
154	106.51	95.57	143.10	143.10
155	106.17	97.54	144.17	144.17
156	105.83	103.54	148.06	148.06
157	105.50	104.61	148.57	148.57
158	105.17	96.30	142.60	142.60
159	104.84	100.98	145.57	145.57
160	104.52	108.19	150.43	150.43
161	104.20	98.43	143.34	143.34
162	103.88	90.94	138.07	138.07
163	103.57	96.98	141.89	141.89
164	103.26	101.39	144.71	144.71
165	102.95	101.04	144.25	144.25
166	102.64	100.71	143.80	143.80
167	102.34	102.08	144.55	144.55
168	102.04	102.71	144.78	144.78
169	101.74	104.13	145.58	145.58
170	101.44	102.81	144.43	144.43
171	101.15	103.63	144.81	144.81
172	100.86	104.93	145.54	145.54
173	100.57	104.64	145.13	145.13
174	100.29	104.78	145.04	145.04
175	100.00	105.61	145.45	145.45
176	99.72	107.23	146.44	146.44
177	99.44	105.36	144.88	144.88
178	99.17	110.01	148.11	148.11
179	98.89	109.90	147.85	147.85
180	98.62	105.34	144.30	144.30
181	98.35	105.89	144.52	144.52
182	98.09	112.53	149.28	149.28
183	97.82	107.99	145.71	145.71
184	97.56	105.44	143.65	143.65
185	97.30	108.92	146.05	146.05

Ring index	V_{bulge}	V_{disk}	V_{total} bulge not rotating	V_{total} bulge rot. like disk
186	97.04	105.10	143.05	143.05
187	96.78	104.22	142.23	142.23
188	96.53	109.94	146.30	146.30
189	96.28	114.04	149.25	149.25
190	96.02	110.80	146.62	146.62
191	95.78	115.82	150.29	150.29
192	95.53	116.70	150.81	150.81
193	95.28	116.12	150.21	150.21
194	95.04	118.67	152.04	152.04
195	94.80	123.16	155.42	155.42
196	94.56	126.50	157.94	157.94
197	94.32	124.27	156.01	156.01

Table C.1: Result of the rotation velocities in the galaxy NGC 7331

Result of the rotation velocities in the galaxy NGC 7331 with a NFW halo

Ring index	V_{bulge}	V_{disk}	$V_{NFWhalo}$	V_{total} bulge not rot. + NFW	V_{total} bulge rot. like disk + NFW
0	185.23	42.55	44.02	0.09	195.09
1	211.42	34.74	52.18	0.16	220.52
2	236.70	28.85	59.07	0.17	245.66
3	252.28	23.23	65.08	0.22	261.57
4	262.33	16.38	70.45	0.31	272.12
5	266.14	0.00	75.32	0.55	276.57
6	269.87	0.00	79.78	0.91	280.83
7	273.80	0.00	83.91	2.04	285.37
8	276.26	0.00	87.74	3.42	288.76
9	276.00	0.00	91.33	3.74	289.29
10	276.48	0.00	94.71	5.78	290.45
11	276.67	0.00	97.88	8.15	291.95
12	277.18	0.00	100.89	6.69	293.39
13	276.71	0.00	103.74	9.02	293.48
14	274.96	0.00	106.45	12.38	292.54
15	273.72	0.00	109.04	13.75	292.09
16	272.08	0.00	111.50	17.85	291.51
17	270.36	0.00	113.86	19.53	290.84
18	268.21	0.00	116.11	24.33	289.63

Ring index	V_{bulge}	V_{disk}	$V_{NFWhalo}$	V_{total} bulge not rot. + NFW	V_{total} bulge rot. like disk + NFW
19	266.40	0.00	118.27	25.84	288.81
20	264.67	0.00	120.35	27.64	287.77
21	262.05	0.00	122.34	43.17	286.29
22	259.10	0.00	124.26	54.39	285.11
23	255.90	0.00	126.11	68.43	283.67
24	252.38	0.00	127.88	93.63	282.55
25	249.55	13.61	129.60	71.75	281.52
26	245.72	23.58	131.26	149.97	279.57
27	241.99	34.97	132.86	161.54	278.27
28	238.45	42.25	134.40	165.49	276.96
29	234.93	50.56	135.90	192.26	276.07
30	231.93	55.23	137.34	137.02	275.14
31	229.28	54.22	138.74	113.65	273.42
32	226.22	55.20	140.10	186.07	271.75
33	223.52	57.81	141.41	147.24	270.74
34	220.68	57.57	142.69	188.96	269.03
35	217.89	56.12	143.93	205.77	267.09
36	215.03	52.51	145.13	264.68	264.68
37	212.28	33.55	146.29	259.98	259.98
38	209.63	75.28	147.42	267.11	267.11
39	207.08	100.11	148.52	273.80	273.80
40	204.63	89.25	149.59	268.73	268.73
41	202.25	86.11	150.63	266.48	266.48
42	199.96	85.14	151.64	265.00	265.00
43	197.74	84.49	152.62	263.69	263.69
44	195.60	83.15	153.57	262.22	262.22
45	193.52	82.71	154.50	261.08	261.08
46	191.51	83.38	155.41	260.35	260.35
47	189.56	83.65	156.29	259.53	259.53
48	187.67	82.95	157.15	258.45	258.45
49	185.83	82.72	157.99	257.56	257.56
50	184.05	83.64	158.80	257.08	257.08
51	182.32	83.97	159.60	256.44	256.44
52	180.63	83.79	160.37	255.68	255.68
53	178.99	82.84	161.13	254.69	254.69
54	177.40	81.19	161.87	253.50	253.50
55	175.85	83.35	162.58	253.58	253.58
56	174.33	84.79	163.29	253.47	253.47
57	172.86	81.33	163.97	251.76	251.76

Ring index	V_{bulge}	V_{disk}	$V_{NFWhalo}$	V_{total} bulge not rot. + NFW	V_{total} bulge rot. like disk + NFW
58	171.42	78.07	164.64	250.17	250.17
59	170.02	74.24	165.29	248.47	248.47
60	168.65	67.95	165.93	246.15	246.15
61	167.31	62.45	166.55	244.20	244.20
62	166.01	63.12	167.16	243.89	243.89
63	164.73	69.77	167.75	245.24	245.24
64	163.49	74.15	168.33	246.09	246.09
65	162.27	66.14	168.89	243.37	243.37
66	161.08	63.86	169.44	242.36	242.36
67	159.91	80.68	169.98	246.93	246.93
68	158.77	90.34	170.51	249.89	249.89
69	157.66	81.29	171.03	246.40	246.40
70	156.56	71.88	171.53	243.11	243.11
71	155.49	74.63	172.02	243.60	243.60
72	154.44	80.31	172.51	245.07	245.07
73	153.42	85.13	172.98	246.38	246.38
74	152.41	82.68	173.44	245.24	245.24
75	151.42	87.01	173.89	246.45	246.45
76	150.45	88.36	174.33	246.64	246.64
77	149.50	91.77	174.76	247.61	247.61
78	148.57	97.53	175.18	249.54	249.54
79	147.65	92.20	175.59	247.25	247.25
80	146.75	99.40	176.00	249.78	249.78
81	145.87	101.22	176.39	250.28	250.28
82	145.00	95.65	176.78	247.84	247.84
83	144.15	92.16	177.16	246.29	246.29
84	143.31	91.18	177.53	245.70	245.70
85	142.49	98.86	177.89	248.44	248.44
86	141.68	101.57	178.24	249.32	249.32
87	140.89	100.08	178.59	248.51	248.51
88	140.10	101.82	178.93	249.02	249.02
89	139.34	100.86	179.26	248.44	248.44
90	138.58	98.94	179.58	247.48	247.48
91	137.83	97.73	179.90	246.81	246.81
92	137.10	96.40	180.21	246.10	246.10
93	136.38	101.33	180.52	247.90	247.90
94	135.67	102.30	180.82	248.13	248.13
95	134.97	100.12	181.11	247.07	247.07
96	134.29	102.17	181.40	247.74	247.74

Ring index	V_{bulge}	V_{disk}	$V_{NFWhalo}$	V_{total} bulge not rot. + NFW	V_{total} bulge rot. like disk + NFW
97	133.61	104.02	181.68	248.35	248.35
98	132.94	104.30	181.95	248.31	248.31
99	132.28	111.37	182.22	251.21	251.21
100	131.64	105.16	182.48	248.37	248.37
101	131.00	95.88	182.74	244.43	244.43
102	130.37	102.99	182.99	247.16	247.16
103	129.75	107.63	183.24	248.99	248.99
104	129.14	107.72	183.48	248.89	248.89
105	128.53	106.88	183.72	248.38	248.38
106	127.94	106.45	183.95	248.07	248.07
107	127.35	104.59	184.17	247.14	247.14
108	126.78	104.63	184.40	247.02	247.02
109	126.20	103.11	184.61	246.25	246.25
110	125.64	107.28	184.83	247.90	247.90
111	125.09	112.97	185.03	250.29	250.29
112	124.54	107.24	185.24	247.63	247.63
113	124.00	104.17	185.44	246.20	246.20
114	123.46	109.86	185.63	248.54	248.54
115	122.94	110.24	185.83	248.59	248.59
116	122.42	105.26	186.01	246.31	246.31
117	121.90	101.05	186.20	244.42	244.42
118	121.39	102.51	186.38	244.91	244.91
119	120.89	102.63	186.55	244.85	244.85
120	120.40	103.63	186.72	245.16	245.16
121	119.91	105.70	186.89	245.93	245.93
122	119.43	103.85	187.06	245.02	245.02
123	118.95	103.59	187.22	244.81	244.81
124	118.48	103.80	187.38	244.79	244.79
125	118.01	105.37	187.53	245.35	245.35
126	117.55	110.18	187.68	247.35	247.35
127	117.10	102.32	187.83	243.84	243.84
128	116.65	95.01	187.98	240.76	240.76
129	116.20	99.74	188.12	242.57	242.57
130	115.76	102.30	188.26	243.53	243.53
131	115.33	104.51	188.39	244.37	244.37
132	114.90	103.32	188.52	243.76	243.76
133	114.47	104.44	188.65	244.14	244.14
134	114.05	106.54	188.78	244.94	244.94
135	113.63	109.02	188.91	245.94	245.94

Ring index	V_{bulge}	V_{disk}	$V_{NFWhalo}$	V_{total} bulge not rot. + NFW	V_{total} bulge rot. like disk + NFW
136	113.22	105.81	189.03	244.43	244.43
137	112.82	101.82	189.15	242.63	242.63
138	112.41	103.34	189.26	243.18	243.18
139	112.02	99.61	189.38	241.52	241.52
140	111.62	102.63	189.49	242.69	242.69
141	111.23	105.16	189.59	243.67	243.67
142	110.85	101.05	189.70	241.83	241.83
143	110.46	101.12	189.80	241.77	241.77
144	110.09	103.30	189.90	242.60	242.60
145	109.71	103.22	190.00	242.47	242.47
146	109.34	100.47	190.10	241.22	241.22
147	108.97	101.00	190.19	241.35	241.35
148	108.61	104.75	190.29	242.86	242.86
149	108.25	107.22	190.38	243.84	243.84
150	107.90	108.82	190.46	244.46	244.46
151	107.54	102.48	190.55	241.61	241.61
152	107.19	101.02	190.63	240.91	240.91
153	106.85	101.56	190.71	241.05	241.05
154	106.51	95.57	190.79	238.50	238.50
155	106.17	97.54	190.87	239.20	239.20
156	105.83	103.54	190.95	241.62	241.62
157	105.50	104.61	191.02	242.00	242.00
158	105.17	96.30	191.09	238.44	238.44
159	104.84	100.98	191.16	240.28	240.28
160	104.52	108.19	191.23	243.31	243.31
161	104.20	98.43	191.30	239.04	239.04
162	103.88	90.94	191.36	235.97	235.97
163	103.57	96.98	191.42	238.28	238.28
164	103.26	101.39	191.49	240.02	240.02
165	102.95	101.04	191.54	239.79	239.79
166	102.64	100.71	191.60	239.56	239.56
167	102.34	102.08	191.66	240.05	240.05
168	102.04	102.71	191.71	240.24	240.24
169	101.74	104.13	191.77	240.76	240.76
170	101.44	102.81	191.82	240.11	240.11
171	101.15	103.63	191.87	240.38	240.38
172	100.86	104.93	191.92	240.86	240.86
173	100.57	104.64	191.96	240.65	240.65
174	100.29	104.78	192.01	240.63	240.63

Ring index	V_{bulge}	V_{disk}	$V_{NFWhalo}$	V_{total} bulge not rot. + NFW	V_{total} bulge rot. like disk + NFW
175	100.00	105.61	192.05	240.91	240.91
176	99.72	107.23	192.10	241.55	241.55
177	99.44	105.36	192.14	240.64	240.64
178	99.17	110.01	192.18	242.63	242.63
179	98.89	109.90	192.22	242.50	242.50
180	98.62	105.34	192.25	240.38	240.38
181	98.35	105.89	192.29	240.54	240.54
182	98.09	112.53	192.33	243.46	243.46
183	97.82	107.99	192.36	241.31	241.31
184	97.56	105.44	192.39	240.10	240.10
185	97.30	108.92	192.42	241.57	241.57
186	97.04	105.10	192.45	239.79	239.79
187	96.78	104.22	192.48	239.33	239.33
188	96.53	109.94	192.51	241.79	241.79
189	96.28	114.04	192.54	243.61	243.61
190	96.02	110.80	192.56	242.03	242.03
191	95.78	115.82	192.59	244.29	244.29
192	95.53	116.70	192.61	244.63	244.63
193	95.28	116.12	192.63	244.27	244.27
194	95.04	118.67	192.65	245.42	245.42
195	94.80	123.16	192.67	247.54	247.54
196	94.56	126.50	192.69	249.15	249.15
197	94.32	124.27	192.71	247.94	247.94

Table C.2: Result of the rotation velocities in the galaxy NGC 7331 with a NFW halo

Bibliography

[1] Sloan Digital Sky Survey / SkyServer. Characteristics of galaxies, 2018 (accessed December 22, 2018). Available at: `http://skyserver.sdss.org/dr1/en/proj/advanced/galaxies/characteristics.asp`. 1

[2] J. Binney and M. Merrifield. *Galactic Astronomy*. Princeton University Press, Princeton, New Jersey, 1998. 3, 4

[3] F. Combes. *Mysteries of Galaxy Formation*. Springer Praxis Books / Popular Astronomy. Springer-Verlag New York Inc, 2010. 3, 61

[4] M. Longair. *The Cosmic Century: A History of Astrophysics and Cosmology*. Cambridge University Press, 2006. 3, 4

[5] H. Pointcaré. The Milky Way and the theory of gases. *Popular Astronomy, vol. 14, pp.475-488*, 1906. Available at: `http://adsabs.harvard.edu/abs/1906PA.....14..475P`. 3, 57

[6] F. Zwicky. On the masses of nebulae and of clusters of nebulae. *Astrophysical Journal, vol. 86, p.217*, 1937. Available at: `http://adsabs.harvard.edu/abs/1937ApJ....86..217Z`. 3, 57

[7] E. Battaner and E. Florido. The rotation curve of spiral galaxies and its cosmological implications. *arXiv:astro-ph/0010475*, 2000, reviewed October 2018. Available at: `https://arxiv.org/pdf/astro-ph/0010475v1.pdf`. 3, 57, 58, 60, 61

[8] R. Bottema and J.G. Pestaña. The distribution of dark and luminous matter inferred from extended rotation curves. *arXiv:1501.06424*, 2015. Available at: `https://arxiv.org/pdf/1501.06424.pdf`. 3, 58

[9] M. Milgrom. A modification of the Newtonian dynamics as a possible alternative to the hidden mass hypothesis. *Astrophysical Journal, Part 1, vol. 270*, 1983. Available at: `http://adsabs.harvard.edu/abs/1983ApJ...270..365M`. 3, 60

[10] J. Binney. Dark matter versus magnetism. *Nature 360 (6405)*, 1992. Available at: `https://ora.ox.ac.uk/objects/pubs:211584`. 4, 61

[11] D. Pfenniger and F. Combes. Is dark matter in spiral galaxies cold gas? II. fractal models and star non-formation. *arXiv:astro-ph/9311044*, 1993. Available at: `https://arxiv.org/pdf/astro-ph/9311044.pdf`. 4, 61

[12] J. Binney and S. Tremaine. *Galactic Dynamics*. Princeton University Press, Princeton, New Jersey, 2011. 4, 51

[13] NASA/IPAC Extragalactic Database, 2018 (accessed July 20, 2018). Available at: `https://ned.ipac.caltech.edu/`. 5, 9, 10

[14] Bob Erdmann. The NGC/IC project: NGC/IC database files, 2006 (accessed December 26, 2018). Available at: `http://ngcicproject.org/erdmann/`. 5

[15] News Staff / Source. Hubble observes unbarred spiral galaxy NGC 7331, Jan. 5

[16] H0 Key Project: S.M.G. Hughes, M. Han, J. Hoessel, W.L. Freedman, R.C. Kennicutt, J.R. Mould, A. Saha, P.B. Stetson, B.F. Madore, N.A. Silbermann, P. Harding, L.Ferrarese, H. Ford, B.K. Gibson, J.A. Graham, R. Hill, J. Huchra, G.D. Illingworth, R. Phelps, and S. Sakai. The Hubble space telescope extragalactic distance scale key project. X. the cepheid distance to NGC 7331.

arXiv:astro-ph/9802184, 1998. Available at: https://arxiv.org/pdf/1408.6953.pdf. 5, 6, 35, 56

[17] European Space Agency. Hubble space telescope: Twins with differences, 2018 (accessed December 26, 2018). Available at: https://www.spacetelescope.org/images/potw1805a/. 5

[18] F. Prada, C. Gutierrez, R.F. Peletier, and C.D. McKeith. A counter-rotating bulge in the sb galaxy ngc 7331. *arXiv:astro-ph/9602142*, 1996. Available at: https://arxiv.org/abs/astro-ph/9602142. 5, 54

[19] L. Van de Vyvere. Distribution de vitesse, de masse et de luminosité dans la galaxie spirale NGC3198. 2018. Available at: http://hdl.handle.net/2268.2/5031. 9, 27, 34, 36, 51, 53, 62

[20] European Southern Observatory - MIDAS, 2018 (accessed July 20, 2018). Available at: https://www.eso.org/sci/software/esomidas/. 12, 16

[21] J. Biernaux, P. Magain, D. Sluse, and V. Chantry. Analysis of luminosity distributions and shape parameters of strong gravitational lensing elliptical galaxies. *arXiv:1510.09118*, 2015. Available at: https://arxiv.org/pdf/1510.09118.pdf. 17, 19, 62

[22] P. Morrissey, T. Conrow, T.A. Barlow, T. Small, M. Seibert, T.K. Wyder, T. Budavari, S. Arnouts, P.G. Friedman, K. Forster, D.C. Martin, S.G. Neff, D. Schiminovich, L. Bianchi, J. Donas, T.M. Heckman, Y.-W. Lee, B.F. Madore, B. Milliard, R.M. Rich, A.S. Szalay, B.Y. Welsh, and S.K. Yi. The calibration and data products of the Galaxy Evolution Explorer. *arXiv:0706.0755*, 2007. Available at: https://arxiv.org/pdf/0706.0755.pdf. 22

[23] N. Padmanabhan, D.J. Schlegel, D.P. Finkbeiner, J.C. Barentine, M.R. Blanton, H.J. Brewington, J.E. Gunn, M. Harvanek, D.W. Hogg, Z. Ivezic, D. Johnston, S.M. Kent, S.J. Kleinman, G.R. Knapp, J. Krzesinski, D. Long, E.H.

Neilsen, A. Nitta, C. Loomis, R.H. Lupton, S. Roweis, S.A. Snedden, M.A. Strauss, and D.L. Tucker. An improved photometric calibration of the Sloan Digital Sky Survey imaging data. *arXiv:astro-ph/0703454*, 2007. Available at: https://arxiv.org/pdf/astro-ph/0703454.pdf. 23

[24] R. C. Bohlin, M. E. Dickinson, and D. Calzetti. Spectrophotometric standards from the far-ultraviolet to the near-infrared: STIS and NICMOS fluxes. *The Astronomical Journal*, 2001. Available at: http://adsabs.harvard.edu/abs/2001AJ....122.2118B. 23

[25] W.T. Reach, S.T. Megeath, M. Cohen, J. Hora, S. Carey, J. Surace, S.P. Willner, P. Barmby, G. Wilson, W. Glaccum, P. Lowrance, M. Marengo, and G.G. Fazio. Absolute calibration of the infrared array camera on the Spitzer space telescope. *arXiv:astro-ph/0507139*, 2005. Available at: https://arxiv.org/pdf/astro-ph/0507139.pdf. 23

[26] Z. Balog, T. Müller, M. Nielbock, B. Altieri, U. Klaas, J. Blommaert, H. Linz, D. Lutz, A. Moór, N. Billot, M. Sauvage, and K. Okumura. The Herschel-PACS photometer calibration: Point-source flux calibration for scan maps. *arXiv:1309.6099*, 2013. Available at: https://arxiv.org/pdf/1309.6099.pdf. 23

[27] B.T. Draine. Interstellar dust grains. *arXiv:astro-ph/0304489*, 2003. Available at: https://arxiv.org/pdf/astro-ph/0304489.pdf. 27, 30, 56, 62

[28] B.T. Draine and J.C. Weingartner. Dust grain size distributions and extinction in the Milky Way, LMC, and SMC. *arXiv:astro-ph/0008146*, 2001. Available at: https://arxiv.org/pdf/astro-ph/0008146.pdf. 27

[29] C. Maraston. Stellar population models. *arXiv:astro-ph/0301419*, 2003. Available at: https://lanl.arxiv.org/pdf/astro-ph/0301419v1. 27, 34, 43, 62

[30] Galactic dust reddening and extinction - NASA/IPAC Infrared Science Archive, 2011 (accessed October 14, 2018). Available at: `https://irsa.ipac.caltech.edu/applications/DUST`. 28

[31] B.T. Draine and A. Li. Infrared emission from interstellar dust. II. the diffuse interstellar medium. *arXiv:astro-ph/0011319*, 2001. Available at: `https://arxiv.org/pdf/astro-ph/0011319.pdf`. 30, 56, 62

[32] C. Maraston. Evolutionary population synthesis: models, analysis of the ingredients and application to high-z galaxies. *aarXiv:astro-ph/0410207*, 2005. Available at: `https://arxiv.org/pdf/astro-ph/0410207.pdf`. 34, 43

[33] T. Maschberger. On the function describing the stellar initial mass function. *arXiv:1212.0939*, 2012. Available at: `https://arxiv.org/pdf/1212.0939.pdf`. 35

[34] E.E. Salpeter. The luminosity function and stellar evolution. *1955ApJ...121..161S*, 1955. Available at: `http://adsabs.harvard.edu/abs/1955ApJ...121..161S`. 35, 57

[35] P. Kroupa. The initial mass function of stars: Evidence for uniformity in variable systems. *arXiv:astro-ph/0201098*, 2002. Available at: `https://arxiv.org/pdf/astro-ph/0201098.pdf`. 35, 57

[36] Filter Profile Service - Spanish Virtual Observatory, 2018 (accessed November 12, 2018). Available at: `http://svo2.cab.inta-csic.es/svo/theory/fps/`. 35

[37] C. Rodrigo, E. Solano, and A. Bayo. SVO Filter Profile Service. *IVOA*, 2012. Available at: `http://ivoa.net/documents/Notes/SVOFPS/NOTE-SVOFPS-1.0.20121015.pdf`. 35

[38] C. Rodrigo and E. Solano. Filter Profile Service access protocol. *IVOA*, 2013. Available at: `http://ivoa.net/documents/Notes/SVOFPSDAL/20130510/NOTE-SVOFPSDAL-v2-1.0-20130510.pdf`. 35

[39] Laidler et al. Synphot user's guide, v5.0. *Space Telescope Science Institute (STScI)*, 2005. Available at: `http://www.stsci.edu/institute/software_hardware/stsdas/synphot/SynphotManual.pdf`. 35

[40] G.K. Palshikar. Simulated annealing: A heuristic optimization algorithm, 2011 (accessed December 02, 2018). Available at: `http://www.drdobbs.com/architecture-and-design/simulated-annealing-a-heuristic-optimiza/184404780`. 42

[41] Mathworks. Simulated annealing solver for derivative-free unconstrained optimization or optimization with bounds, 2018 (accessed December 02, 2018). Available at: `https://nl.mathworks.com/help/gads/simulated-annealing.html`. 42

[42] A. Bosma. 21-cm line studies of spiral galaxies. I - Observations of the galaxies NGC 5033, 3198, 5055, 2841, and 7331. *Astronomical Journal, vol. 86, 1981AJ.....86.1791B*, 1981. Available at: `http://adsabs.harvard.edu/abs/1981AJ.....86.1791B`. 46, 61, 63

[43] A.K. Leroy, F. Walter, E. Brinks, F. Bigiel, W.J.G. de Blok, B. Madore, and M.D. Thornley. The star formation efficiency in nearby galaxies: Measuring where gas forms stars effectively. *Astronomical Journal, 36:2782–2845*, 2008. Available at: `http://iopscience.iop.org/article/10.1088/0004-6256/136/6/2782/pdf`. 47, 63

[44] Y.I. Izotov, T.X. Thua, and N.G. Guseva. A new determination of the primordial He abundance using the HeI 10830a emission line: cosmological implica-

tions. *arXiv:1408.6953*, 2014. Available at: https://arxiv.org/pdf/1408.6953.pdf. 47, 63

[45] F. Lelli, S.S. McGaugh, and J.M. Schombert. SPARC: Mass models for 175 disk galaxies with Spitzer photometry and accurate rotation curves. *arXiv:1606.09251*, 2016. Available at: https://arxiv.org/pdf/1606.09251.pdf. 48, 51, 53, 64

[46] N.A. Devereux and J.S. Young. The gas/dust ratio in spiral galaxies. *The Astrophysical Journal, Part 1, vol. 359,*, 1990. Available at: http://adsabs.harvard.edu/abs/1990ApJ...359...42D. 56, 63

[47] M. Mollá, F. Ferrini, and A.I. Díaz. Evolution of spiral galaxies. VII. time evolution of the radial distributions of abundances. *The Astrophysical Journal, Volume 475, Number 2*, 1997. Available at: http://iopscience.iop.org/article/10.1086/303550/pdf. 57

[48] J.F. Navarro. The cosmological significance of disk galaxy rotation curves. *arXiv:astro-ph/9807084*, 1998. Available at: https://arxiv.org/pdf/astro-ph/9807084.pdf. 57

[49] J.F. Navarro, C.S. Frenk, and S. White. A universal density profile from hierarchical clustering. *arXiv:astro-ph/9611107*, 1996, reviewed October 1997. Available at: https://arxiv.org/pdf/astro-ph/9611107.pdf. 58

[50] J.F. Navarro and M. Steinmetz. The core density of dark matter halos: a critical challenge to the Lambda-CDM paradigm? *arXiv:astro-ph/9908114*, 1999. Available at: https://arxiv.org/pdf/astro-ph/9908114.pdf. 58

[51] M. Milgrom. MOND theory. *arXiv:1404.7661*, 2014. Available at: https://arxiv.org/pdf/1404.7661.pdf. 60

[52] R.H. Sanders and S.S. McGaugh. Modified Newtonian Dynamics as an alternative to dark matter. *arXiv:astro-ph/0204521*, 2002. Available at: https://arxiv.org/pdf/astro-ph/0204521.pdf. 61

[53] C. Carignan, P. Charbonneau, F. Boulanger, and F. Viallefond. Observational study of the spiral galaxy NGC 6946. II - HI kinematics and mass distribution. *Astronomy and Astrophysics, vol. 234, no. 1-2*, 1990. Available at: http://adsabs.harvard.edu/abs/1990A%26A...234...43C. 61

[54] E. Battaner, E. Florido, and A. Guijarro. Magnetic fields are not ignorable in the dynamics of disks. *Galaxy Disks and Disk Galaxies. ASP Conference Series, Vol. 230.*, 2000. Available at: http://cds.cern.ch/record/466030/files/0009391.pdf. 61

[55] E. Battaner, H. Lesch, and E. Florido. Magnetic fields and rotation of spiral galaxies. *arXiv:astro-ph/9802010*, 1998. Available at: https://arxiv.org/pdf/astro-ph/9802010.pdf. 61